HEAT TRANSFER DUE TO SHOCK WAVE TURBULENT BOUNDARY LAYER INTERACTIONS ON HIGH SPEED WEAPON SYSTEMS

K. H. Token

McDonnell Aircraft Company

Prepared for:

Air Force Flight Dynamics Laboratory

April 1974

NOTICE

When Government drawings, specifications, or other data are used for any purpose other than in connection with a definitely related Government procurement operation, the United States Government thereby incurs no responsibility nor any obligation whatsoever; and the fact that the government may have forumulated, furnished, or in any way supplied the said drawings, specifications, or other data, is not to be regarded by implication or otherwise as in any manner licensing the holder or any other person or corporation, or conveying any rights or permission to manufacture, use, or sell any patented invention that may in any way be related thereto.

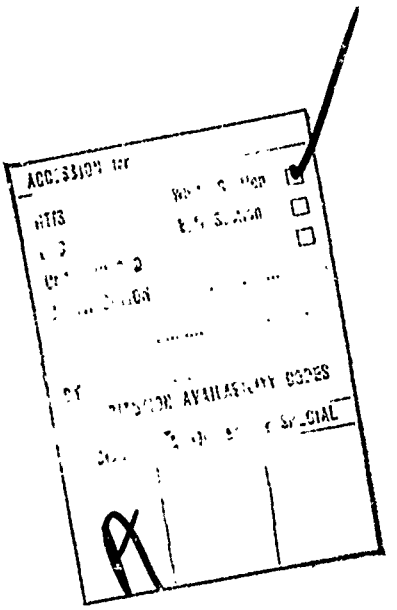

Copies of this report should not be returned unless return is required by security considerations, contractual obligations, or notice on a specific document.

Unclassified

SECURITY CLASSIFICATION OF THIS PAGE (When Data Entered)

AD/A002685

REPORT DOCUMENTATION PAGE

READ INSTRUCTIONS BEFORE COMPLETING FORM

1. REPORT NUMBER: AFFDL-TR-74-77	2. GOVT ACCESSION NO.
3. RECIPIENT'S CATALOG NUMBER	
4. TITLE (and Subtitle): Heat Transfer Due to Shock Wave Turbulent Boundary Layer Interactions on High Speed Weapon Systems	5. TYPE OF REPORT & PERIOD COVERED: Final Report January 73 thru April 74
	6. PERFORMING ORG. REPORT NUMBER
7. AUTHOR(s): K. H. Token	8. CONTRACT OR GRANT NUMBER(s): F33615-73-C-3046
9. PERFORMING ORGANIZATION NAME AND ADDRESS: McDonnell Aircraft Company, Post Office Box 516, St. Louis, Missouri 63166	10. PROGRAM ELEMENT, PROJECT, TASK AREA & WORK UNIT NUMBERS: 1366/03/20
11. CONTROLLING OFFICE NAME AND ADDRESS: United States Air Force, Air Force Systems Command, Wright-Patterson AFB, Ohio 45433	12. REPORT DATE: April 1974
	13. NUMBER OF PAGES: ~~114~~ 117
14. MONITORING AGENCY NAME & ADDRESS(if different from Controlling Office)	15. SECURITY CLASS. (of this report): Unclassified
	15a. DECLASSIFICATION/DOWNGRADING SCHEDULE

16. DISTRIBUTION STATEMENT (of this Report)

Approved for public release, distribution unlimited.

17. DISTRIBUTION STATEMENT (of the abstract entered in Block 20, if different from Report)

18. SUPPLEMENTARY NOTES

19. KEY WORDS (Continue on reverse side if necessary and identify by block number)

Three-dimensional Interaction
Turbulent Boundary Layer
Heat Transfer
Flow Field

20. ABSTRACT (Continue on reverse side if necessary and identify by block number)

Three-dimensional shock wave turbulent boundary layer interactions caused by a fin-plate configuration (glancing shock problem) were investigated experimentally and analytically.

Wind tunnel tests were conducted at a Mach number of 3.71 and at Reynolds numbers of 1.5×10^6 and 3.5×10^6 per foot. The interactions were studied at near full scale conditions by mounting one of several fins normal to the tunnel sidewall in the naturally turbulent, 6 inches thick sidewall boundary

DD FORM 1 JAN 73 1473 EDITION OF 1 NOV 65 IS OBSOLETE

Unclassified

SECURITY CLASSIFICATION OF THIS PAGE (When Data Entered)

layer. Tests were conducted primarily with a sharp leading edge planar fin, although blunt and blunt swept planar fins were also used. The fins were deflected to angles from -4 to +20 degrees, in 2 degree increments, relative to the free stream flow. Surface pressures, surface heating, pitot pressure profiles, and oil flow patterns were measured. All measurements were made with excellent spatial resolution due to the thickness of the sidewall boundary layer.

The experimental flow field and heating data indicate that the interaction region is a very complex three dimensional flow field. The data agree favorably with McCabe's criterion for three-dimensional incipient boundary layer separation. The flow field disturbance caused by the interaction was observed to propagate relatively large distances upstream of the fin generated shock wave for both separated and unseparated flow. Local peak heating rates were measured close to the fin surface and observed to increase with distance downstream. Maximum heating rates were not measured, they occur further aft than the most downstream measurements.

The experimental data were used to develop new analytical and correlation procedures. The test results indicate that the interaction flow field may be dominated by a vortex. This hypothesis is used to develop a new analytical technique for calculating heating distributions between the impinging fin shock wave and the peak heating locus. To complement this analysis, new correlations are obtained for the location and magnitude of peak heating and the magnitude of the heating at the impinging shock wave location.

PREFACE

This document presents surface heating and flow field data, correlations, and an analysis of three-dimensional shock wave boundary layer interaction heating. The study was conducted by McDonnell Aircraft Company under Contract F33615-73-C-3046, Project Number 1366, issued by the Air Force Flight Dynamics Laboratory, Wright-Patterson Air Force Base. This final report, submitted in April 1974, describes all of the work accomplished for the duration of the contract beginning in January 1973 and ending in April 1974. The experimental program was conducted in the NASA Langley Unitary Plan Tunnel during a two week test period beginning in June 1973.

The contract effort was directed by Mr. Richard D. Neumann (AFFDL/FXG) of the Flight Dynamics Laboratory. The NASA test project engineer was Mr. Robert L. Stallings, Jr. Key McDonnell Aircraft personnel were Dr. Kenneth H. Token, who as Principal Investigator, was responsible for planning of the test program, interpretation of the results, and development of the analytical techniques; Richard R. Dieckmann, who served as Program Manager; Richard D. Hardin, who served as test engineer; Kenneth Borgmeyer, who provided the model design; and John E. Harder, who developed the technique for machine plotting of test results.

This technical report has been reviewed and is approved.

PHILIP P. ANTONATOS
Chief, Flight Mechanics Division
AF Flight Dynamics Laboratory

SUMMARY

Three-dimensional shock wave turbulent boundary layer interactions caused by a fin-plate configuration (glancing shock problem) were investigated experimentally and analytically.

Wind tunnel tests were conducted at a Mach number of 3.71 and at Reynolds numbers of 1.5×10^6 and 3.5×10^6 per foot. The interactions were studied at near full scale conditions by mounting one of several fins normal to the tunnel sidewall in the naturally turbulent, 6 inches thick sidewall boundary layer. Tests were primarily conducted with a sharp leading edge planar fin, although blunt and blunt swept planar fins were also used. The fins were deflected to angles from -4 to +20 degrees, in 2 degree increments, relative to the free stream flow. Surface pressures, surface heating, pitot pressure profiles, and oil flow patterns were measured. All measurements were made with excellent spatial resolution due to the thickness of the sidewall boundary layer.

The experimental flow field and heating data indicate that the interaction region is a very complex three dimensional flow field. The data agree favorably with McCabe's criterion for three-dimensional incipient boundary layer separation. The flow field disturbance caused by the interaction was observed to propagate relatively large distances upstream of the fin generated shock wave for both separated and unseparated flow. Local peak heating rates were measured close to the fin surface and observed to increase with distance downstream. Maximum heating rates were not measured, they occur further aft than the most downstream measurements.

The experimental data were used to develop new analytical and correlation procedures. The test results indicate that the interaction flow field may be dominated by a vortex. This hypothesis is used to develop a new analytical technique for calculating heating distributions between the impinging fin shock wave and the peak heating locus. To compliment this analysis, new correlations are obtained for the location and magnitude of peak heating and the magnitude of the heating at the impinging shock wave location.

TABLE OF CONTENTS

TABLE OF CONTENTS (CONT.)

LIST OF ILLUSTRATIONS

LIST OF ILLUSTRATIONS (CONT.)

LIST OF ILLUSTRATIONS (CONT.)

LIST OF TABLES

1. INTRODUCTION

Aerodynamic heating rates on aircraft and missiles increase with vehicle speed. In many regions on the surface, vehicle geometry causes shock waves to interact with the surface boundary layers. These shock wave boundary layer interactions cause local heating rates which are considerably higher than undisturbed heating values. Recent investigations of shock wave boundary layer interactions are summarized by Korkegi in Reference 1. High localized heating rates can be major design problems on high speed weapon systems.

Three-dimensional shock wave boundary layer interactions have not been considered extensively in the past. However, three-dimensional interactions can produce local heating rates which are higher than those produced by two-dimensional interactions. Test data obtained on small scale models indicated that the three-dimensional interactions will occur in many areas on the surface of high speed aircraft. Neumann and Burke in Reference 3 developed a technique for predicting three-dimensional interaction peak heating magnitudes and locations. Their approach is based on the hypothesis that the impinging shock wave effectively destroys the existing boundary layer and that an effective new boundary layer is formed in the interaction region. This proposed correlation, however, does not compare well with turbulent data.

This report presents the results of an experimental and analytical program to study three-dimensional shock wave turbulent boundary layer interactions.

The experimental program was conducted by investigating interactions in the thick, naturally turbulent boundary layer on a wind tunnel sidewall. The goal was to make measurements with sufficient spatial resolution to accurately identify heating and surface flow distributions, and to obtain data at near flight scale conditions. Wind tunnel tests were conducted at a free stream Mach number of 3.71 and at two Reynolds numbers: 1.5 and 3.5×10^6 per foot. The experimental configuration is shown in Figure 1. Planar fins with sharp, blunt, and blunt swept leading edges were mounted normal to the tunnel sidewall. Primary emphasis was placed on data with the sharp leading edge fin since the more simple fin geometry produces an

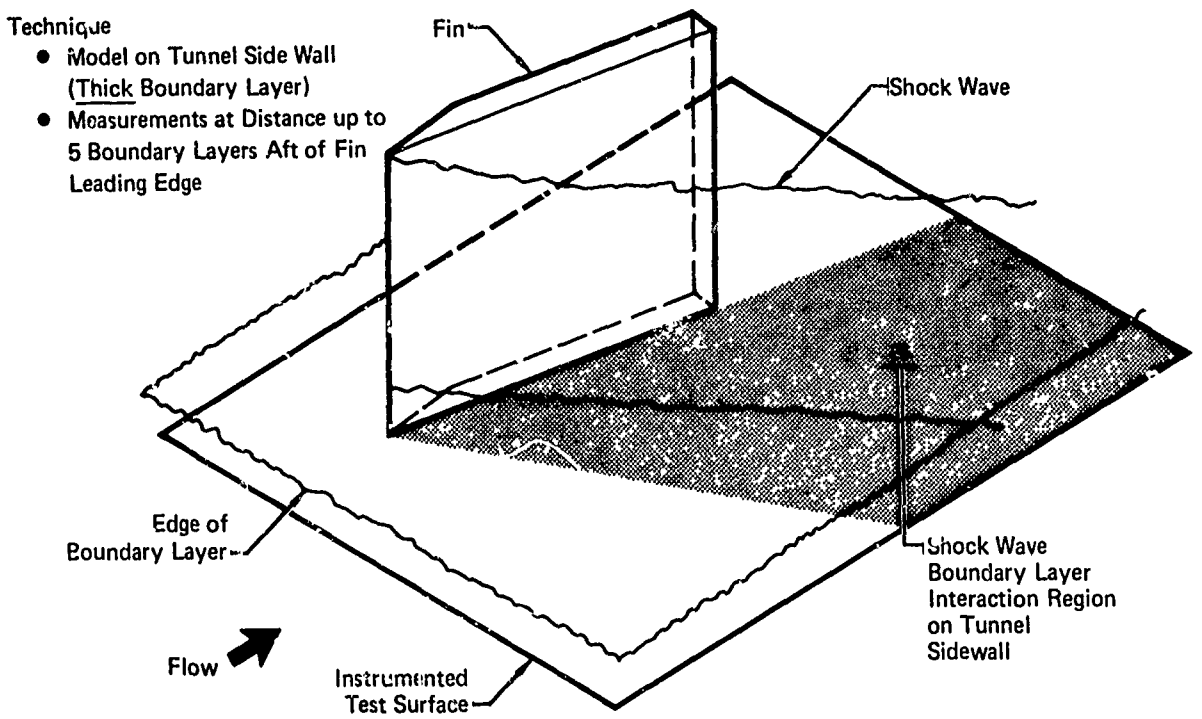

FIGURE 1 THREE-DIMENSIONAL SHOCK WAVE TURBULENT BOUNDARY LAYER INTERACTION CONFIGURATION

interaction which can be more easily handled analytically. Tests were conducted with the fins remotely selected to angles from -4 to +20 degrees relative to the free stream flow, in 2 degree increments. An instrumented plate, mounted flush with the tunnel sidewall, was positioned relative to the fin in order to measure surface pressures and surface heating in the interaction region. In addition, pitot pressure profiles and surface oil streak patterns in the interaction region were measured and recorded.

The sharp fin test results indicate that the three-dimensional shock wave boundary layer interaction region is a complex flow region which causes a highly nonuniform heating distribution. The test data agree favorably with McCabe's three-dimensional incipient boundary layer separation criterion. The data also indicate that the interaction disturbance propagates a relatively large distance upstream of the fin shock wave for separated and unseparated flow interactions. The observed local peak heating data shows that peak heating lies close to the fin-plate interface and that the peak heating increases with distance downstream of the leading edge. Based on the rate of increase in the local peak heating magnitude with distance aft, it is

apparent that the maximum heating is downstream of the most aft instrumentation. The magnitude of the heating at the impinging shock wave location was found to be constant along the shock and to only depend on fin deflection angle. Measured surface pressures in t' e interaction region never reached values calculated by oblique shock theory. The wind tunnel test program and results from the tests are discussed in Section 2.

The analytical program was conducted by correlating the measured heating data, and by developing a new analysis technique for heating distributions. Favorable correlations and comparisons were obtained between the analysis technique and test data. Data correlations and the analysis technique are presented in Section 3.

A new correlation for the peak heating location and magnitude in the interaction region caused by a sharp leading edge fin was developed. The correlation for peak heating location compares favorably with Reference 3 test data obtained at Mach numbers of 6 and 8. The variation of peak heating magnitude as a function of distance from the fin leading edge is shown to be independent of fin deflection angle when it is normalized by the oblique shock pressure ratio raised to the 0.9 power. The peak heating magnitude was correlated for the range of parameters available in the experimental phase of the study. Based on the measured data, it is hypothesized that the interaction flow field is dominated by a spiral vortex formed by the rollup of the separated boundary layer. This hypothesis suggests that the downstream distance to the point of maximum heating will scale with boundary layer thickness

Heating at the impinging shock location was correlated for sharp fin data. This new correlation shows that the shock impingement heating is constant for fin deflection angles which are less than McCabe's incipient separation angle. The heating at the shock impingement location is shown to increase monotonically with fin deflection angle for fin deflection angles greater than McCabe's incipient separation angle. The heating at the shock impingement location was observed to be independent of distance downstream of the fin leading edge. The constant heating along the shock impingement line suggests that it is characteristic of turbulent heating in a separated region.

The vortex flow hypothesis was used to develop a new analytical technique for defining heating distributions between the impinging shock wave

and the peak heating locus. The analytical heating distribution technique favorably correlates the sharp fin test data. The heating distributions, in nondimensional form, are shown to be independent of the fin angle and downstream location, except in the region very close to the fin leading edge.

The correlations and analysis technique developed from the sharp leading edge fin data are compared with blunt, and blunt swept fin test data. Considering the flow field complexity introduced by fin blunting and sweep, the correlations compare favorably, or they deviate in an explainable manner.

2. EXPERIMENTAL PROGRAM

The experimental program consisted of model design and fabrication, wind tunnel testing, and subsequent data reduction. The model, which contains a high surface instrumentation density, was installed as part of the sidewall of the NASA Langley Unitary Plan Wind Tunnel. Wind tunnel tests were conducted at a Mach number of 3.71 and Reynolds numbers of 3.5 and 1.5 x 10^6 per foot. A remotely positionable fin, mounted normal to the sidewall, produced an oblique shock which interacted with the naturally turbulent sidewall boundary layer. Testing was conducted with five fin configurations oriented at selected fin deflection angles between -4 and +20 degrees relative to the free-stream flow. Measurements of surface pressure, heat transfer, oil flow patterns and pitot pressure profiles were recorded. Data measured in the interaction region were reduced to engineering units and presented on machine generated plots. The plotted results and the oil flow patterns indicate certain qualitative characteristics of the interaction region. All pertinent aspects of the wind tunnel, the model, the testing, and the data reduction and data accuracy are discussed in Section 2.1. A discussion of the test results is presented in Section 2.2.

2.1 Wind Tunnel, Model, and Testing

Wind tunnel tests were conducted in the NASA Langley Unitary Plan Wind Tunnel. The turbulent boundary layer which flows along the test section sidewall was used as part of the test flow field. Surface and flow field measurements were made in the interaction region formed by this boundary layer and the shock wave emanating from fins mounted perpendicular to the sidewall. The test facility, model, instrumentation, test conditions, and data reduction are discussed in this section.

2.1.1 Wind Tunnel - The NASA Langley Unitary Plan Wind Tunnel is a continuous flow, variable pressure tunnel with a two-dimensional nozzle. The asymmetric sliding block nozzle provides Mach number variations. Heat transfer measurements are made using the thin skin technique which requires a rapid rise in the tunnel total temperature. The tunnel compressor aftercoolers are bypassed to provide a rapid rise to an increased total temperature for such tests. In the facility, the temperature increases 150°R in 4 seconds when the aftercoolers are bypassed. The period when the total temperature is high is termed the heat pulse. The steady state total temperature during periods

of compressor aftercooling is nominally 610°R. During the heat pulse a total temperature of nominally 760°R is attained. A more thorough description of the facility is provided in Reference 4.

2.1.2 Model - The wind tunnel model consists of a flat plate assembly and several assemblies which support and position one of five interchangeable shock generating fins. Figure 2 is an oblique frontal installation photograph of the model with a fin attached. A sketch of the wind tunnel model assembly presented in Figure 3 identifies all components. A highly instrumented test plate assembly is mounted in an adapter plate assembly. The adapter plate assembly is attached to the test section door which is recessed from the tunnel sidewall. Windward surfaces of both plate assemblies are flush with the tunnel sidewall. One of five interchangeable fin assemblies is held in a position normal to the test plate assembly. Each fin assembly rotates about a fixed pivot pin by an electro-hydraulic fin deflection system.

The boundary flow region in the vicinity of the corners of the test section, where the boundary layers from the walls and the floor or ceiling merge, was anticipated to be highly non-uniform. To avoid these non-uniformities,

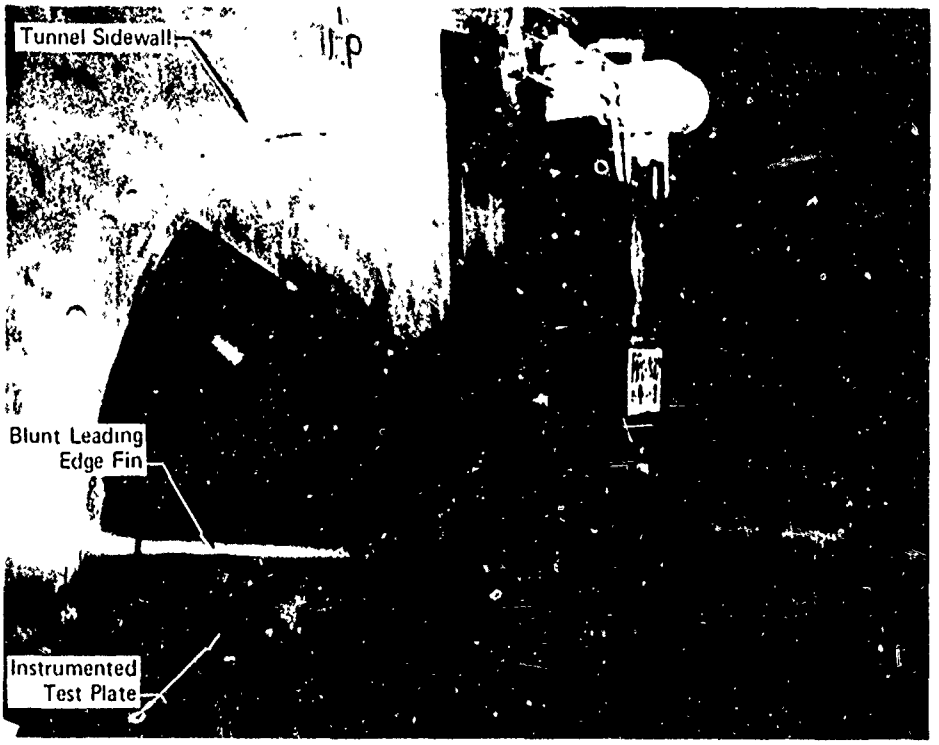

FIGURE 2 PHOTO OF MODEL INSTALLATION

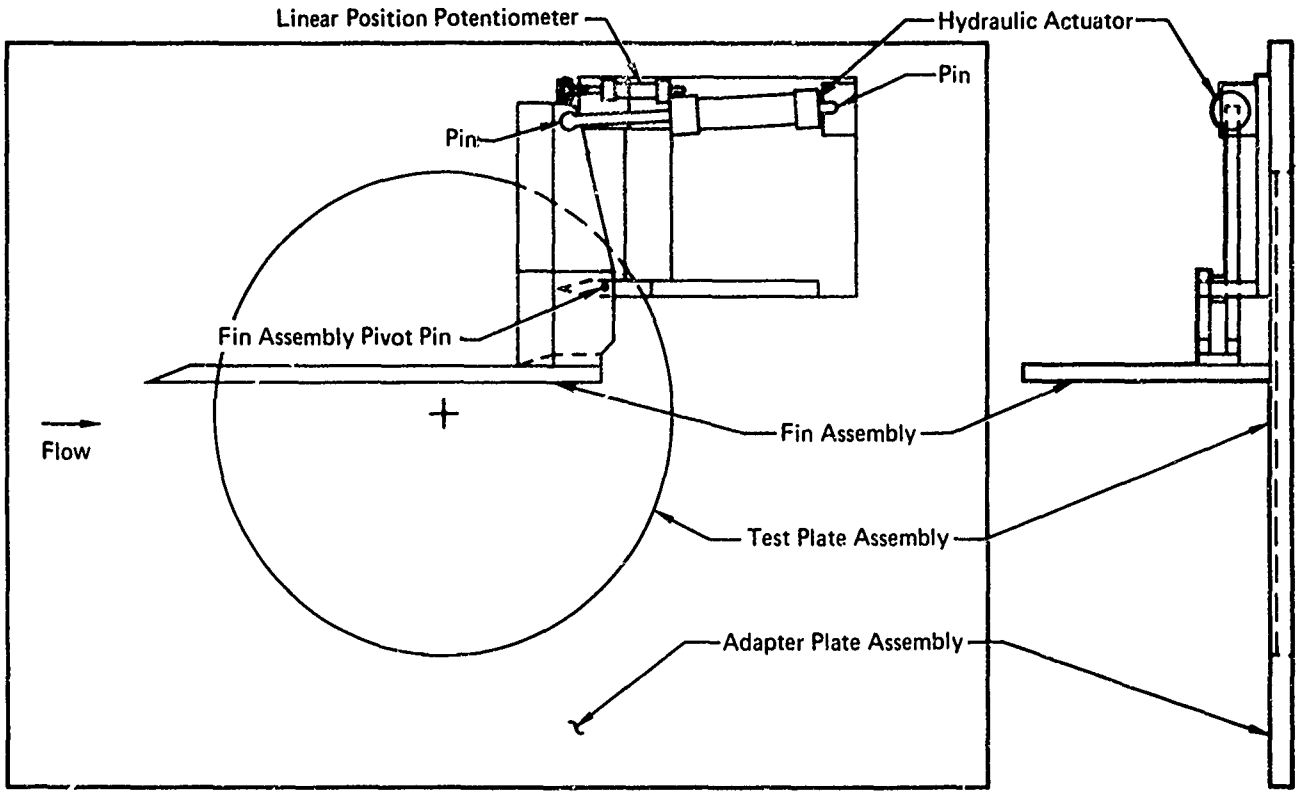

FIGURE 3 WIND TUNNEL MODEL ASSEMBLY

all instrumentation and the shock generating fins were located in a region within 13 inches on each side of the test section midline. This test region is approximately two boundary layer thicknesses from the corners of the test section.

2.1.2.1 Test Plate Assembly - The test plate assembly is illustrated in Figure 4. It consists of a 32-inch diameter aluminum base plate, a phenolic fiberglass honeycomb core, and a 0.032-inch thick stainless steel test plate insert. The test plate insert was sized to measure heat transfer distributions by the thin skin technique. The test plate insert, the honeycomb core, and the base plate are bonded together to form a sandwich construction.

Elongated slots 1-1/2 inches wide are provided in the base plate and in the honeycomb core. This is where 184 surface pressure taps and 240 thermocouples are located and routed.

2.1.2.2 Fin Assemblies - There are five shock generating fin assemblies, as illustrated in Figure 5. The short sharp leading edge fin, the extended sharp leading edge fin, and the blunt leading edge fin use the same fin base plate and three different leading edge sections. The swept leading edge fins, with sweep angles of 45° and 60°, are blunt. The sharp leading edge fins

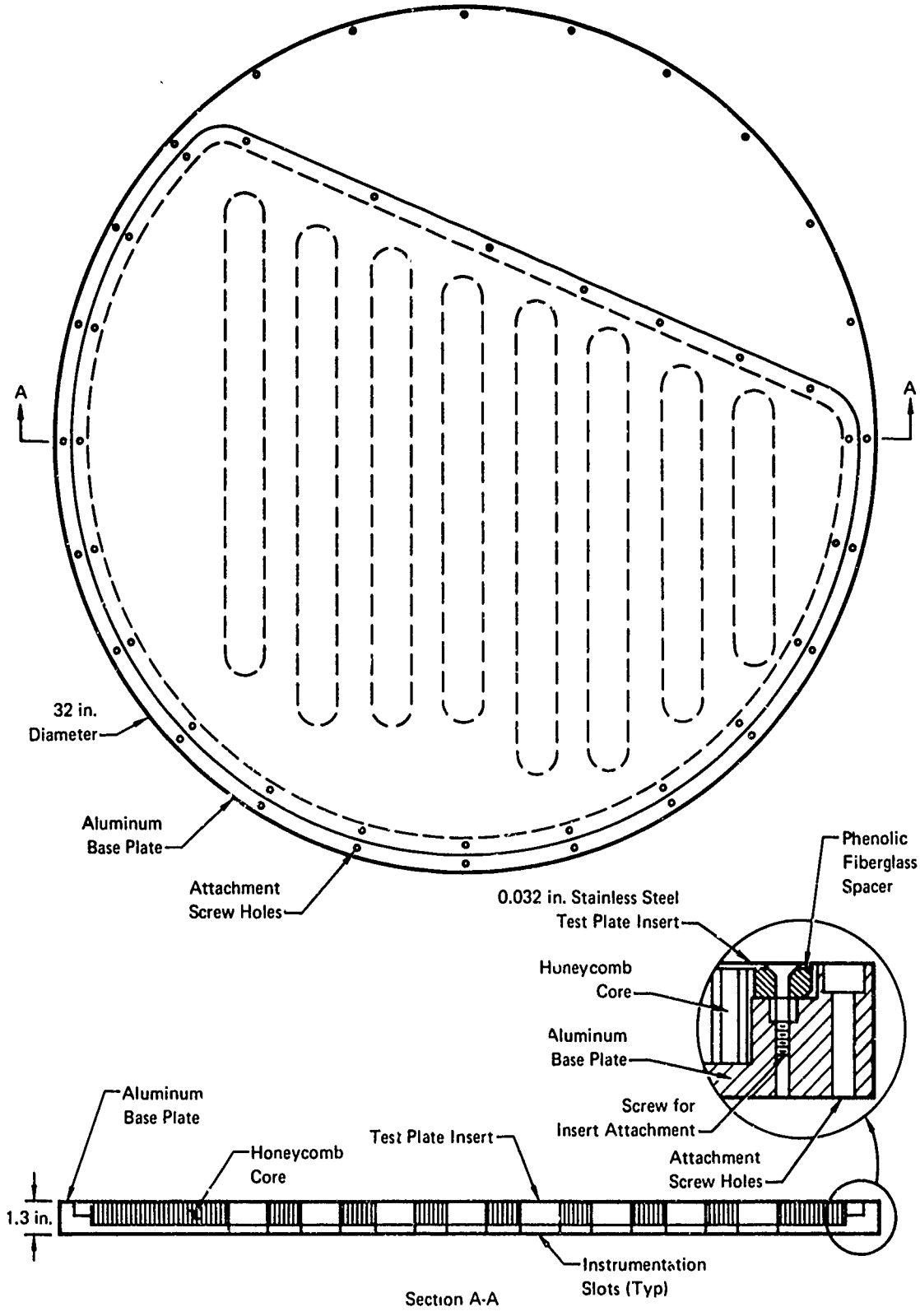

FIGURE 4 TEST PLATE ASSEMBLY

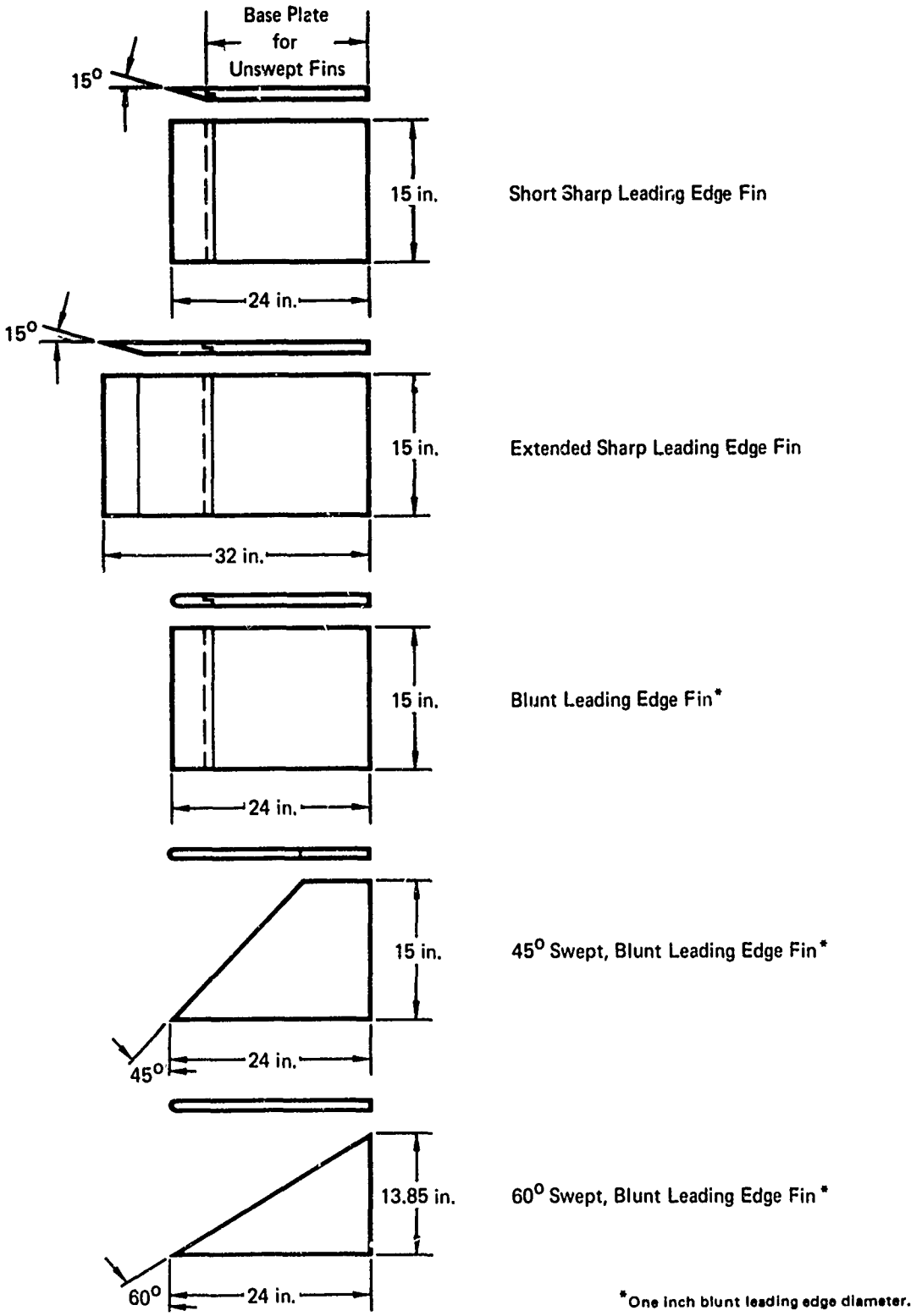

FIGURE 5 SHOCK GENERATING FIN ASSEMBLIES

have scarf angles of 15° and a leading edge bluntness of less than 0.020 inches radius. The blunt leading edge fins have a 1.00-inch circular leading edge diameter in the plane normal to the sweep angle. All fins have a Teflon seal to prevent air flow at the fin-test plate assembly interface.

2.1.2.3 Electro-Hydraulic Fin Deflection Assembly - The deflection angle of the shock generating fins is controlled by an electro-hydraulic fin deflection assembly. The fin deflection assembly, which contains a feed-back control, is used to remotely position the fin assembly to deflection angles between -4 and +20 degrees. The fin position signal, which is input to the feedback control circuit, is provided by a linear potentiometer. A digital voltmeter provides a visual fin position read-out. The signal is also supplied to the data acquisition system.

2.1.3 Instrumentation - Thin skin temperatures and surface pressures were measured on a portion of the test plate assembly surface. Surface pressures were also measured at selected locations on the fin surface and on the adapter plate assembly. The general location of the pressure and thermocouple instrumentation on the tunnel sidewall is illustrated in Figure 6. Pitot pressure profiles were obtained in the interaction region at a fixed axial station and at five transverse locations with a NASA Langley five-probe rake. Surface oil flow patterns for selected configurations were photographed using an AFFDL oil technique. Details of the instrumentation, including calibration techniques for each type of measurement, are discussed in following sections.

2.1.3.1 Thermocouple Measurements - The transient response of thermocouples was used to determine heat transfer coefficients by the thin skin technique. The thermocouples were located on the back (non-flow) side of the test plate insert. The mathematical formulation for determining the heat transfer coefficient is presented in Section 2.1.5.1.

The model is designed to determine surface heat transfer from the response of 240 thermocouples on the test plate insert. The thermocouple junctions were formed by spot welding iron-constantan wires (30 gage) to the back side of the test plate insert. The 240 thermocouples are distributed along four instrumentation columns on the test plate insert. During the model installation, only 198 thermocouples were connected due to facility data recording limitations. Also, four thermocouples became inoperative. Testing was, therefore, conducted with 194 operational thermocouples which were located as indicated in Figure 7.

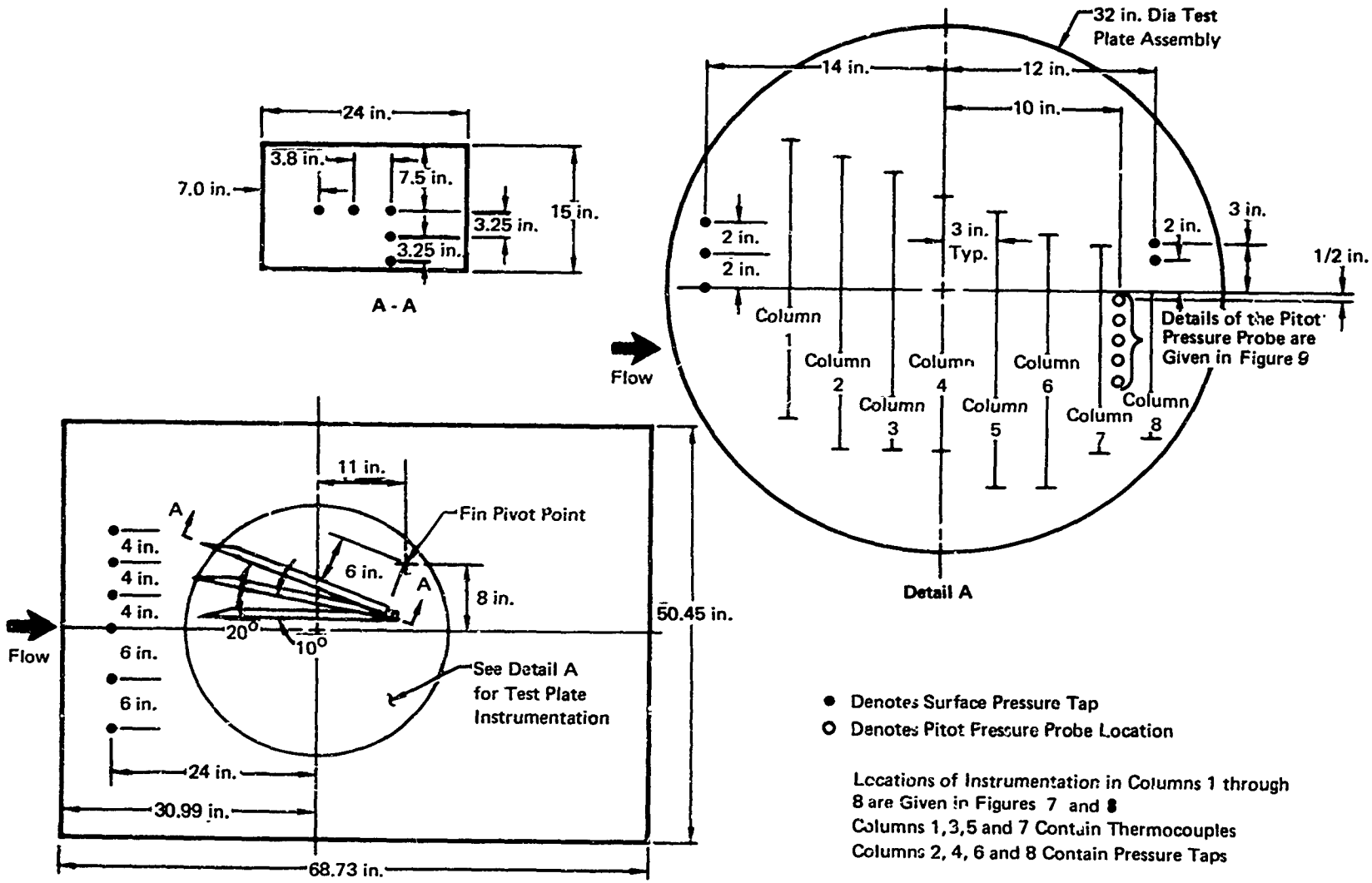

FIGURE 6 LOCATION OF INSTRUMENTATION

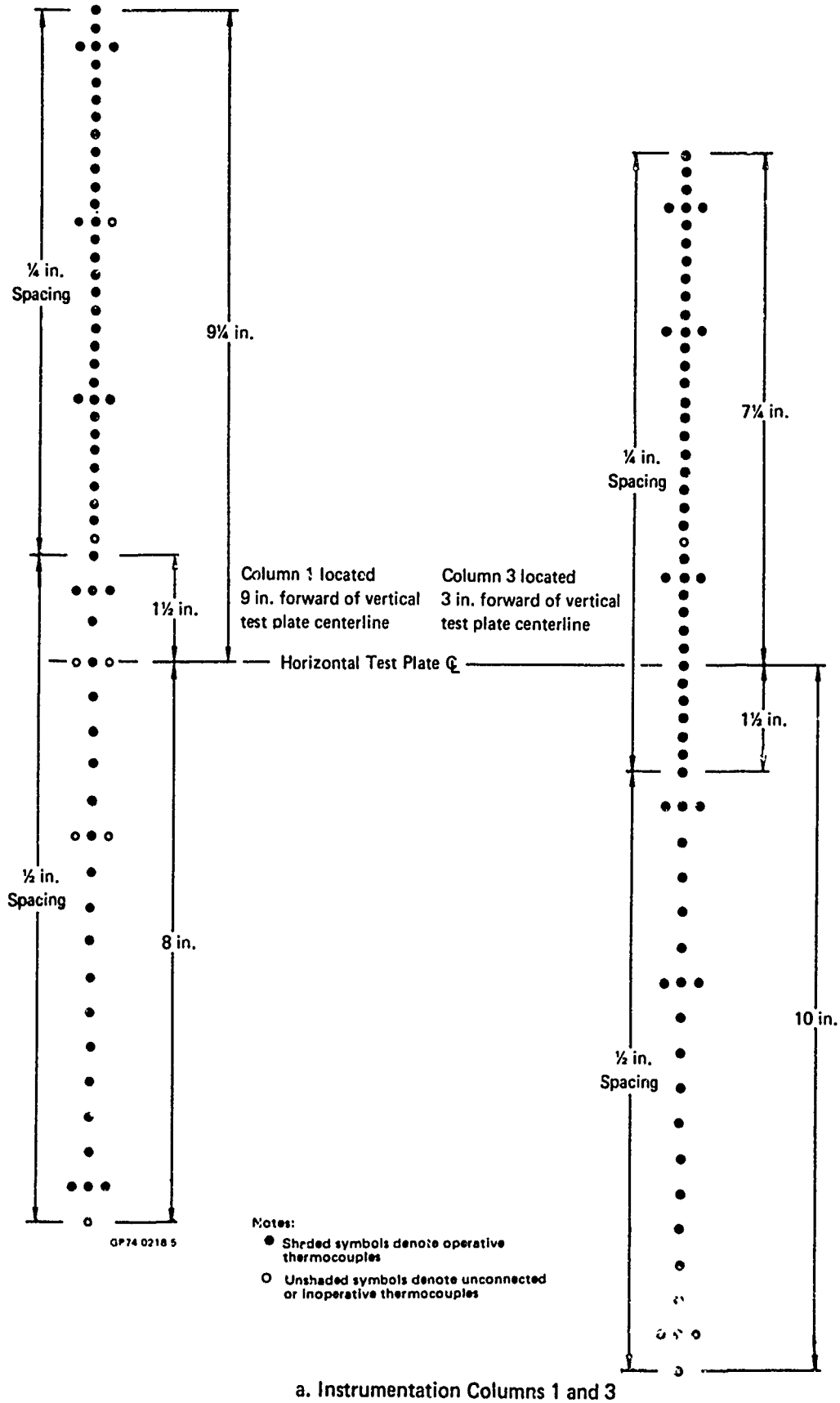

a. Instrumentation Columns 1 and 3

FIGURE 7 THERMOCOUPLE LOCATIONS

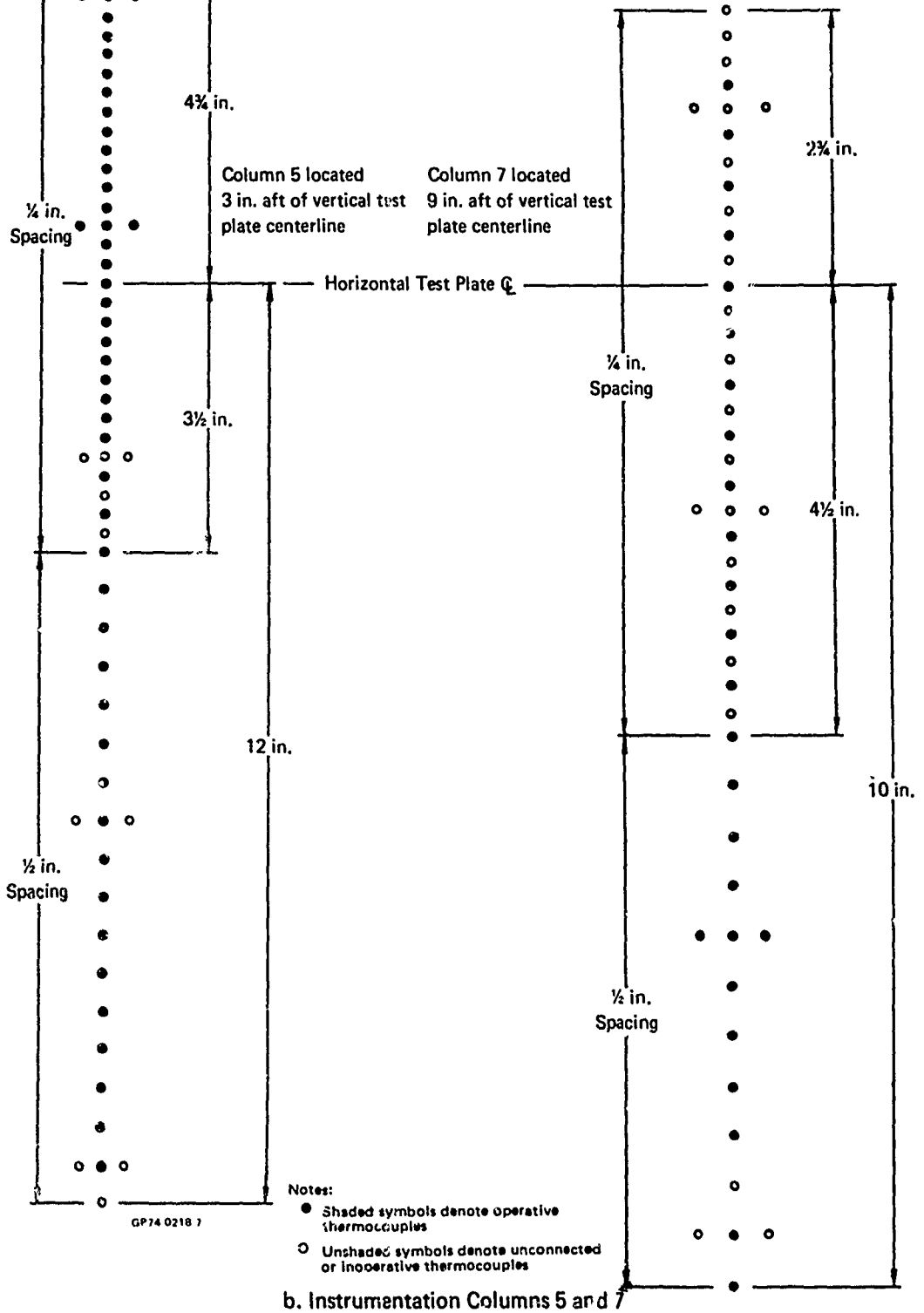

b. Instrumentation Columns 5 and 7

FIGURE 7 THERMOCOUPLE LOCATIONS (Concluded)

2.1.3.2 Surface Pressure Measurements - A total of 200 0.05-inches diameter surface pressure taps are deployed on the test plate insert, on the unswept fin base plate, and on the adapter plate assembly. The locations of the pressure taps are illustrated in Figure 6.

There are 189 surface pressure taps on the test plate insert. A total of 184 of these pressure taps are arranged in four columns on the test plate. Each column was approximately normal to the test section flow. Three of these 184 pressure taps were not operational during testing. The location of pressure taps on these four instrumentation columns is indicated in Figure 8. The five remaining pressure taps on the test plate insert are located as indicated in Figure 6. These five pressure taps served as a further aid in defining the flow field.

Five pressure taps are distributed on the surface of the fin base plate. Pressures measured by these pressure taps served as a check on the fin deflection angle. Some flow field information was also obtained since these taps provide a small amount of fin surface pressure information.

There are six pressure taps on the adapter plate assembly. These pressure taps measured static pressures upstream of the test region. They also served as a check on the calculated static pressure which was used in the data reduction, as explained in Section 2.1.5.2.

2.1.3.3 Pitot Pressure Profile Measurements - Pitot pressure measurements were made with a NASA Langley five-probe pitot pressure rake at the axial location defined in Figure 6. Figure 9 is a schematic illustration providing the dimensions of the rake and the pitot pressure profile measurement stations. The rake was traversed in a direction normal to the sidewall and measurements were made at the 18 rake stations tabulated on Figure 9. During each traverse of the rake, five pitot profiles were obtained. The pitot pressures were measured with the probes at an effective angle of attack, dependent on fin deflection angle, since the rake was maintained at constant attitude while the fins were deflected between 0 and +20 degrees. Measurements made with similar probes by Stallings, Reference 5, at Mach number 3.71 indicate a maximum error of 10% when the probes were placed at a 20 degree yaw angle.

2.1.3.4 Oil Flow Technique - Surface streamline patterns were photographed for selected fin configurations via the oil flow technique. An AFFDL

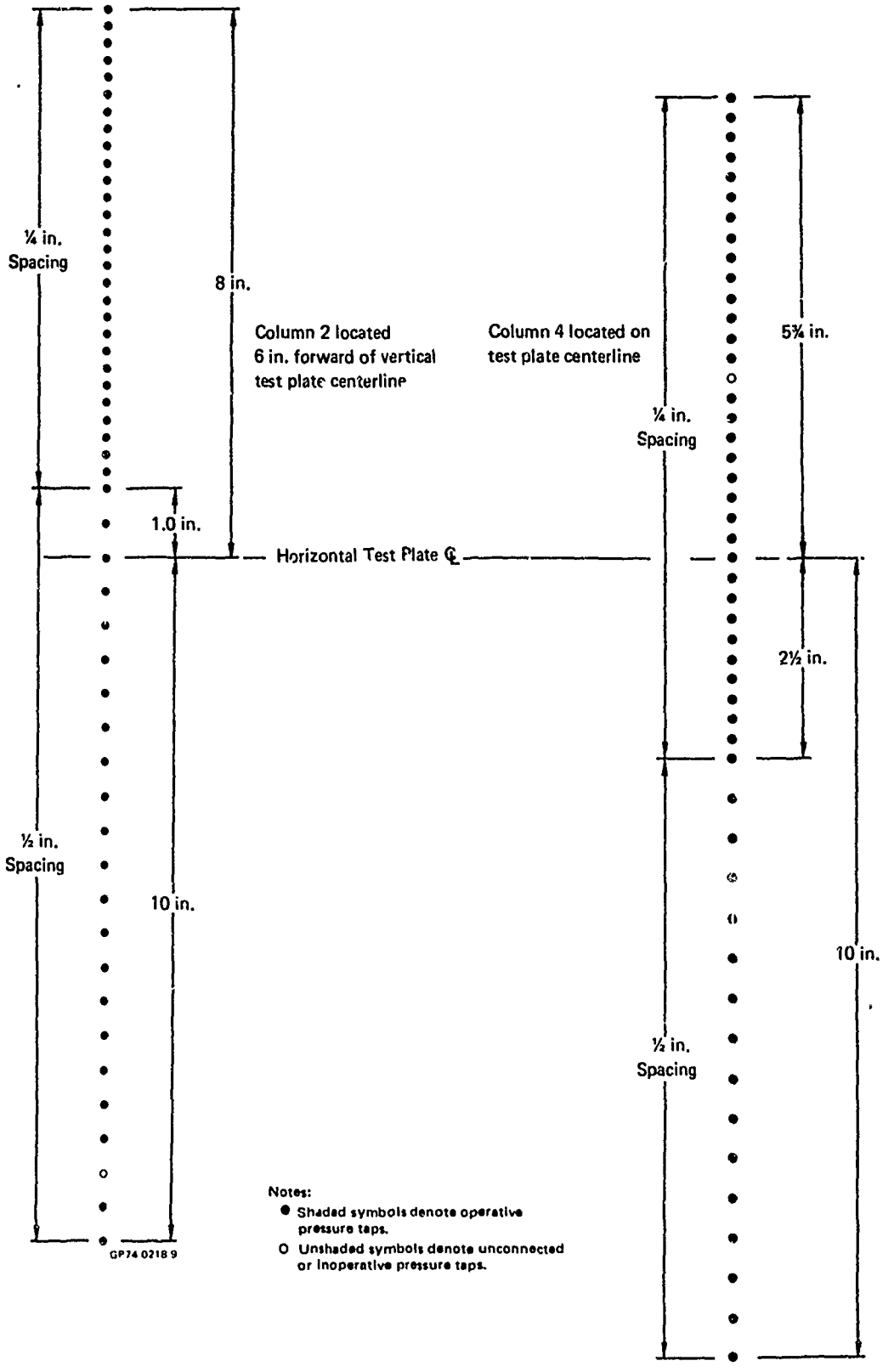

a. Instrumentation Columns 2 and 4

FIGURE 8 PRESSURE TAP LOCATIONS

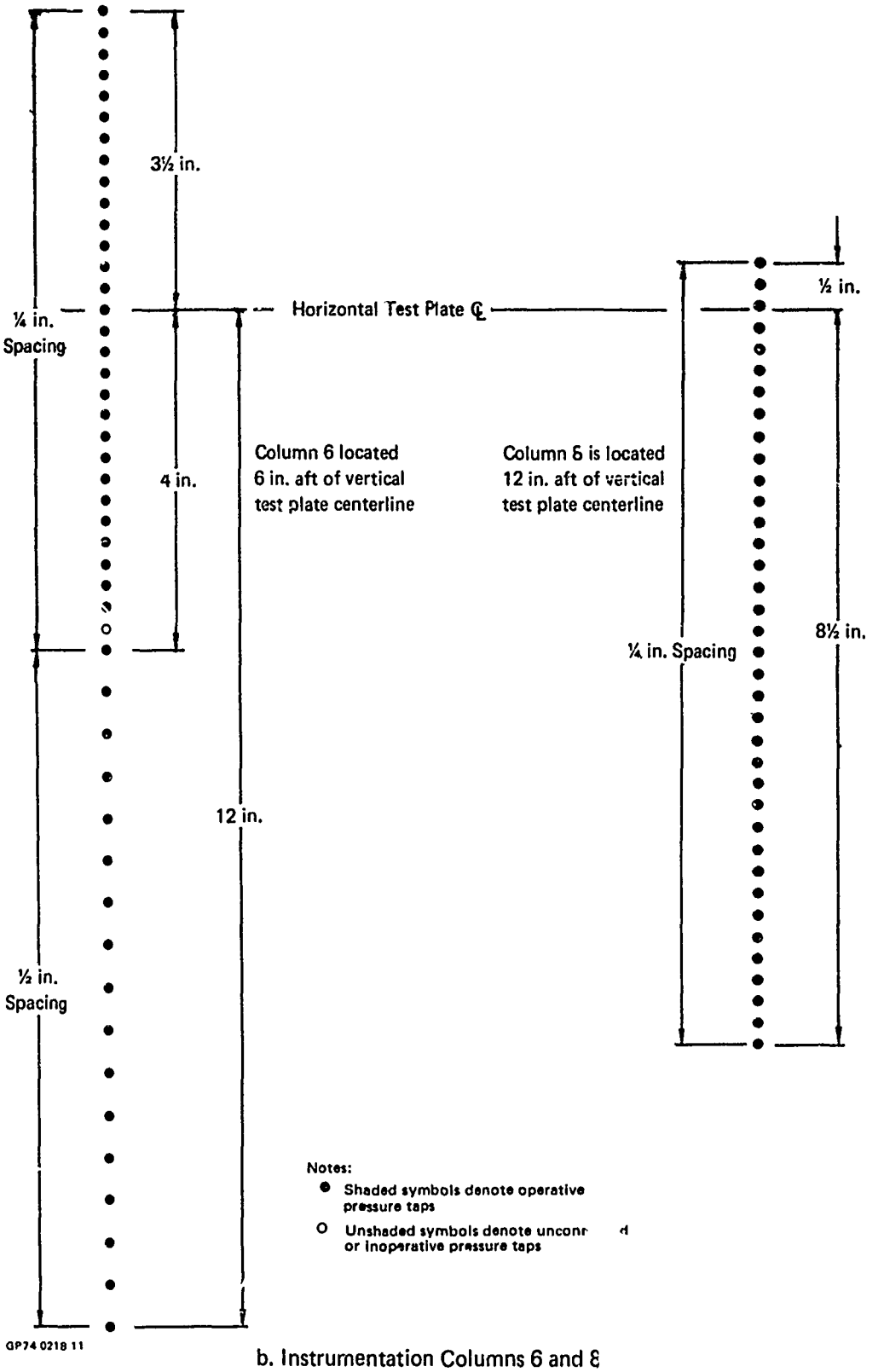

b. Instrumentation Columns 6 and 8

FIGURE 8 PRESSURE TAP LOCATIONS (Concluded)

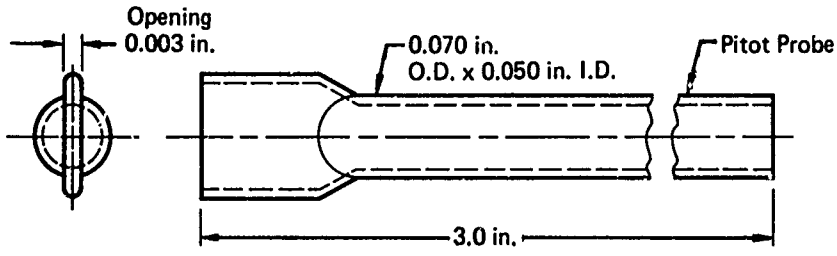

a. Probe Detail

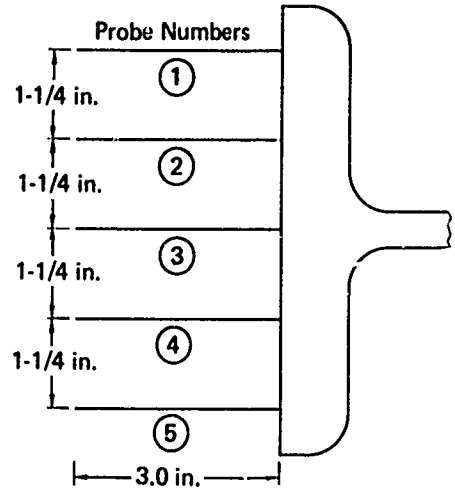

b. Rake Dimensions

Rake Station Identification	z (in.)
1*	0.035
2	0.125
3	0.250
4	0.375
5	0.625
6	0.875
7	1.125
8	1.375
9	1.625
10	2.000
11	2.375
12	2.750
13	3.250
14	3.750
15	4.250
16	4.750
17	5.500
18	6.250

*Probes touching sidewall.

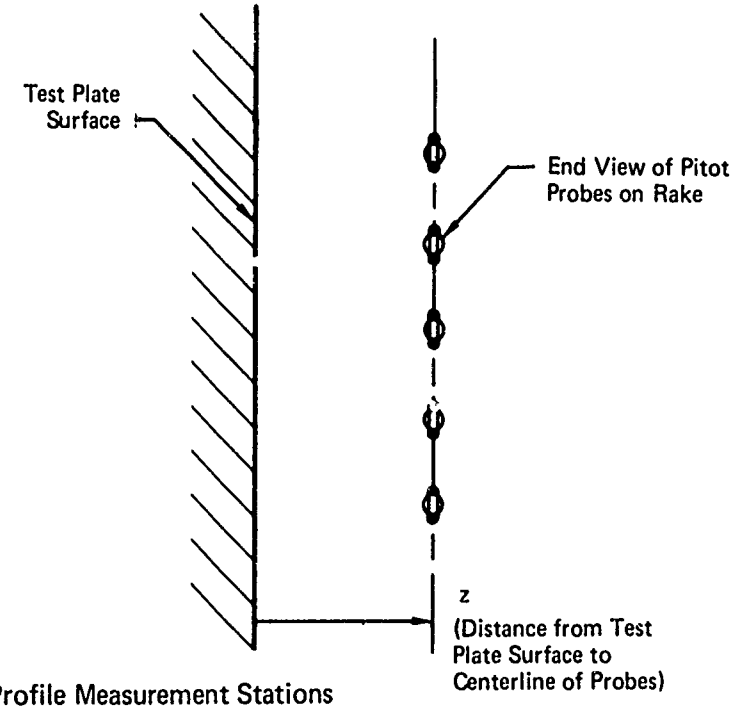

c. Profile Measurement Stations

FIGURE 9 PITOT PRESSURE RAKE DETAIL AND PROFILE MEASUREMENT STATIONS

oil mixture was evaluated on a portion of the sidewall during initial testing and was subsequently used during oil flow tests. This oil is very viscous, having a high percentage of STP brand automotive oil treatment and trace amounts of oleic acid and titanium dioxide. In all cases the oil was applied to the sidewall in vertical strips, approximately an inch wide, with a nominal 6 inch spacing in the test region. During interaction region oil flow tests a strip of oil was also applied on the sidewall near the fin base to accommodate high shearing rates in that region.

2.1.3.5 Calibration Criteria - The instrumentation calibration techniques are described in this section for each of the types of measurements made.

All pressure measurements were made in a segmented sequential manner using scanivalves. A pressure transducer measured the pressure imposed by each port as the scanivalve sampled them sequentially. NASA equipment and NASA calibration techniques were used. The scanivalve also sampled the pressure from two known pressure sources. These known pressure levels were recorded and provided a calibration for the transducer.

The standard iron-constantan thermocouple calibration curve was used to reduce all thermocouple data. The thermocouples were not calibrated. The actual calibration curve consists of thermoelectric effects from the thermocouple junctions, Cannon plug solder connections and pinsocket interfaces, solder connections at the reference junction, and the reference junction itself. It is desirable that the slopes of the two calibration curves (actual and assumed standard) be the same so that the measured transient wall temperature differences are correct. The absolute value of the calibration is less important.

The potentiometer that measured fin deflection angle was calibrated relative to an inclinometer after the model was installed in the wind tunnel and prior to wind tunnel tests each day. The resulting relationship between deflection angle and differential voltage was used to determine fin positions during tests and for the data printout.

The pitot probe rake position potentiometer was calibrated prior to the test program. The calibration was obtained relative to rake position changes as indicated by a precision length measuring device. Zero distance was defined during the test by electrical contact between the pitot rake and the sidewall. The resulting calibration curve was used during tests to adjust

probe positions and to supply correct rake locations.

2.1.4 Test Conditions - Wind tunnel test conditions and testing methods, which were used to monitor and insure the flow field integrity, are described in the following section for each type of measurement made. A summary test matrix is presented in Section 2.2.

2.1.4.1 Wind Tunnel Test Conditions - All wind tunnel tests were conducted at a Mach number of 3.71. The nominal total temperature was 610°R for normal operation and 760°R during the heat pulse mode of operation. The two Reynolds numbers selected for the tests were 1.5×10^6 and 3.5×10^6 per foot.

The standard operating procedure in the NASA Langley Unitary Plan Wind Tunnel is to measure stagnation pressure in the settling chamber upstream of the nozzle. This pressure level is used to establish the desired Reynolds numbers in the wind tunnel. The stagnation pressure reading is also required for data reduction.

The total temperature level was measured during all heat transfer tests with probes mounted on the sidewall opposite from the model installation. Data from Reference 5 indicates that the total temperature profiles at both sidewalls are identical to within probe accuracy.

2.1.4.2 Testing Methods - Testing methods used during the test program can be delineated according to the type of measurement made. Four types of primary measurements were obtained; thin skin temperature, surface pressure, pitot pressure, and surface oil flow photographs.

During the test program heat transfer data were obtained using the thin skin technique. This technique requires the recording of thin skin temperatures during a heat pulse mode of operation. The heat pulse was not initiated or terminated until the thermocouple readings become constant implying that the test plate had reached local thermal equilibrium. The heat transfer testing progressed by measuring the "cold" equilibrium temperatures, the heat pulse was applied, transient temperature data were obtained, and the heat pulse was maintained until the "hot" equilibrium temperatures and the hot pressures were measured. Thus, surface pressure data were measured each time heat transfer data were measured. In addition, heat transfer runs were duplicated with the short sharp fin as time and schedule permitted. Duplicate heating data were obtained at the low Reynolds number condition and at

12 degree and 18 degree fin deflection angles. During the heating and pressure testing tufts were deployed at strategic locations in the test region to assure that the interaction region was not influenced by other disturbances.

The pitot rake was positioned by electrical contact with the sidewall and the pitot pressure was sensed. Thereafter, using the probe position calibration the pitot rake was positioned at selected distances from the sidewall. The probe pressure was allowed to come to equilibrium and the pressures were recorded. This was continued for all pitot rake stations. Subsequently, the surface pressure levels were measured before fin angle or other variables were changed.

Oil flow studies were conducted after all other testing was completed so that the surface heating and pressure results would not be compromised by the presence of the oil.

Two methods of oil flow measurements were attempted. One mode of surface oil flow testing was to start the tunnel with the fin at a small angle of attack. Subsequently, the oil pattern was photographed, the fin was advanced to a larger deflection angle, and the oil flow pattern was again photographed. Testing was continued in this manner for three to four fin deflections. This manner of testing is similar to that suggested by Stanbrook, Reference 6. During the second oil flow test mode the tunnel was started with the fin at the desired deflection angle, the oil pattern for that deflection angle setting was photographed, the tunnel was shut down, oil was reapplied, and the process was repeated for other desired fin deflection angles. A comparison of the results during the testing revealed that the outer oil accumulation line could be determined as accurately by the first method as with the second. However, surface flow directions in the interaction region became confused using the first method. The oil streaks tended to flow along the wetted surface. Therefore, all observed surface flow directions for the second and subsequent fin deflection settings were confusing. Thus the second oil flow technique which requires tunnel shut down between fin deflection settings was used for the remaining oil flow tests.

2.1.5 Data Reduction - The basic data recording and reduction process is schematically illustrated in Figure 10. Signals from all sensors were conditioned and subsequently provided to the NASA Langley Computer System where they were stored on magnetic tape and to the on-site visual display

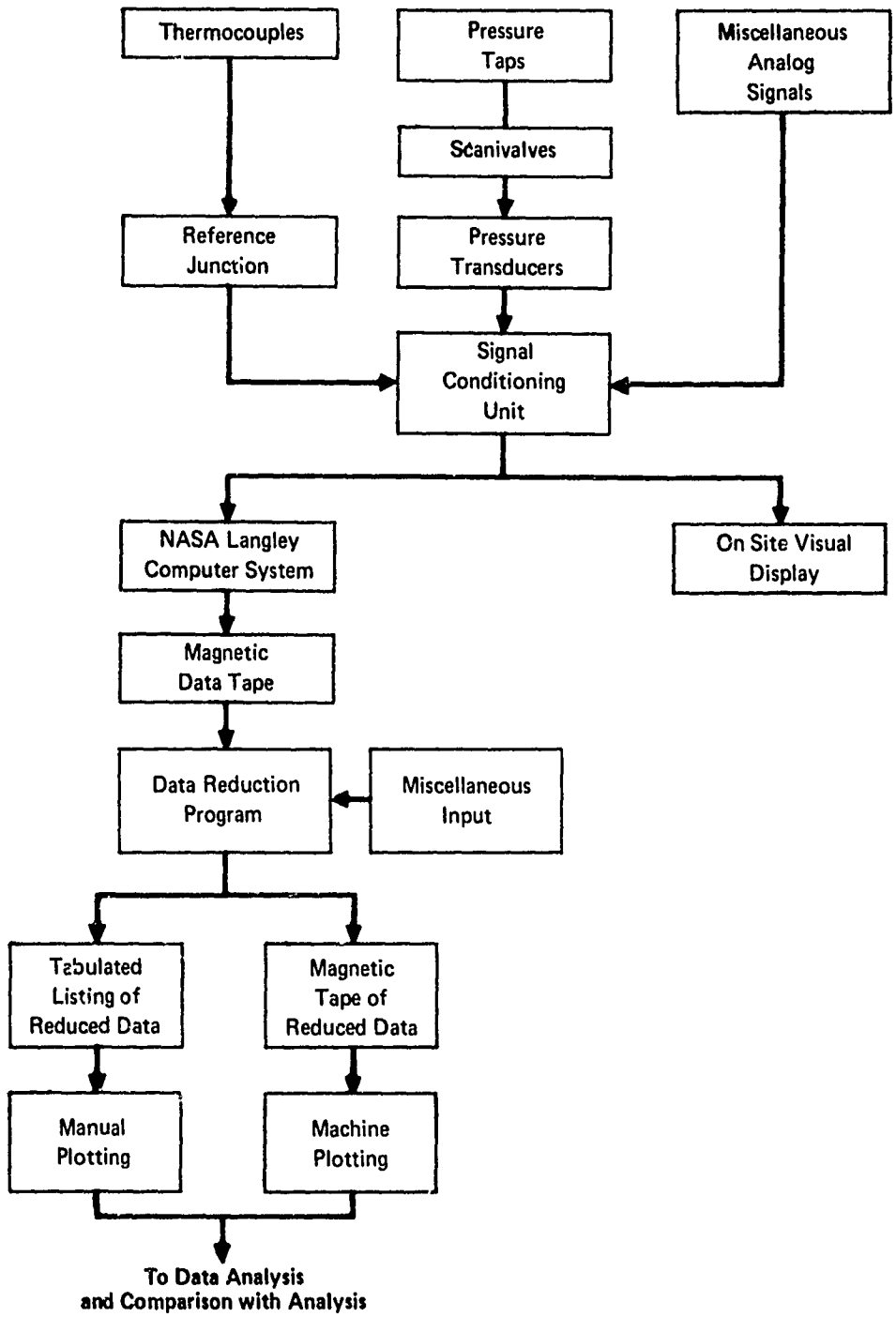

FIGURE 10 SCHEMATIC DIAGRAM OF DATA REDUCTION

(millivolt units). In the computer system the millivolt signals were subsequently read from the magnetic tape, calibration factors were applied, and calculations were made to provide required data formats. The data was then written on magnetic tape and tabulated on paper. The data on magnetic tape was subsequently used to generate machine plots after data from unconnected or malfunctioning sensors, or sensors located under or behind the fin had been deleted. Machine plots eased the task of scrutinizing the data for consistency and validity. The paper tabulated data was used to check the machine plots and for manual data plotting.

Oil flow data which was photographically recorded was viewed qualitatively although some selected quantitative measurements were made on the photographs. Within the framework of basic data reduction, data for each type of instrumentation required special treatment as discussed in this section.

2.1.5.1 Heat Transfer Data Reduction - Heat transfer coefficients were calculated by using the standard thin skin heat transfer data reduction equation of Reference 4, which is reproduced below:

$$h = \frac{W\, C_p\, (d\, T_w/dt)}{T_{eq} - T_w} \cdot \frac{}{} \quad . \tag{1}$$

Calculation of the heating is based on the assumptions that no temperature gradients occur through the skin, that a step function in total temperature is applied, and that radiative and conductive heat transfer from the skin can be neglected. The parameters W and C_p were based on measurements made on the thin skin material, and T_{eq} was measured during the testing for both "hot" and "cold" flow. T_w variations ($T_w(t)$) were measured at each thermocouple location for a period of 10 seconds. The appropriate $T_w(t)$ was selected by the NASA test engineer based on the shape of the total temperature transient.

The heat transfer coefficients obtained by this technique for all tests with fins were normalized with respect to values obtained with no fin (bare sidewall). This technique eliminates, in an approximate manner, effects on the measured heating due to heat transfer through the back side of the test plate and other biased errors since these effects tend to cancel. Lateral conduction corrections were calculated for all heat transfer data in an

approximate manner. The lateral conduction errors are negligible within the accuracy of the approximation, Reference 5. The heat transfer data were reduced to heat transfer coefficient, normalized heat transfer coefficient, and Stanton number data.

2.1.5.2 Surface Pressure Data Reduction - All surface pressure data were reduced to three formats: measured surface pressure, pressure coefficient, and pressure normalized with respect to the freestream static pressure.

2.1.5.3 Pitot Pressure Data Reduction - Pitot pressure data were reduced and normalized with respect to freestream total pressure. Thus both absolute and normalized pitot pressure data were obtained.

2.1.5.4 Oil Flow Data Reduction - Oil flow photographs were reduced to quantitative data by measuring selected angles of characteristic oil flow patterns. Measurements were made of the inclination of oil streak lines in separated flow regions and maximum deflection angles in the interaction region.

2.1.6 Data Accuracy - The accuracy of the measured data is comprised of the instrumentation accuracy, the accuracy of the signal conditioning equipment, the repeatability of the facility run conditions, and the accuracy of calibration constants and physical parameters used in converting data to physical units. All transducers except for the fin deflection angle sensors and the thermocouple junctions were supplied by NASA at the facility. All signal conditioning and recording used standard facility equipment. The facility repeatability was checked by repeating measurements at two of the lower Reynolds number test conditions. The results of this check are discussed in Section 2.2. Calibration factors and physical parameters were determined using techniques consistent with accepted wind tunnel practice. Table 1 presents a summary of the transducer and measurement accuracies.

The heat transfer coefficients were determined using the thin skin technique. The thin skin temperature was measured using thermocouple junctions spot welded on the back side of the test plate. Standard thermocouple wire was used and the inherent uncertainty in temperature measurement is indicated on Table 1 where the possible error is tabulated. Care was taken in the design of the thin skin test plate to reduce thermal inertia and heat leaks. The thin skin thermophysical properties for use during data reduction were accurately measured and the thin skin thickness was measured at each thermocouple location. The accuracy of the resultant heat transfer coefficient

TABLE 1 MEASUREMENT ACCURACY

Data Type	Quantity Measured	Transducer Accuracy	Measurement Accuracy
Heat Transfer	Thermocouple Junction Temperature (^{o}F)	± 1.5^{o}F (1σ)	2.23% of Full Scale
	Heat Transfer Coefficient h Btu/ft^2 sec^{o}F		
	$0.015 \leq h$		± 10%
	$0.001 \leq h \leq 0.015$		± 15%
	$0.0003 \leq h \leq 0.001$		± 20%
	$h \leq 0.0003$		No Significance to Measurement
Surface Pressure	Surface Pressure (5 psia Transducer)	± 0.0125 psia (1σ)	0.5% of Full Scale
Pitot Pressure and Stagnation Pressure	Pitot Pressure and Stagnation Pressure (15 psia Transducer)	± 0.0375 psia (1σ)	0.5% of Full Scale
Pitot Probe Location	Pitot Probe Location (NASA Mechanism and Potentiometer)		± 0.005 in.
Fin Position	Fin Position (Linear Potentiometer)	± 0.092^{o} Deflection	± 0.097^{o} Deflection

is indicated on Table 1 based on NASA experience during a large number of heat transfer tests, Reference 4. It represents the total error observed for data taken during numerous repeat runs. Thus, the cited values contain random as well as biased errors and hence are dependent on model design.

All pressure measurements were made using transducers with 0.25 percent accuracy based on a one sigma (1σ) standard deviation. The scanivalves and signal conditioning equipment increase the measurement error to 0.5 percent of the full scale measurement.

The fin deflection angle and pitot rake positions were sensed with calibrated, temperature compensated, potentiometers. The accuracy shown on Table 1 for the pitot probe location is based on NASA observation. The fin position accuracy is based on MCAIR observation prior to and during the wind tunnel testing.

2.2 Test Results

Wind tunnel tests were conducted for a range of test conditions, fin configurations, and types of measurement. Table 2 is a test matrix which summarizes the data obtained. All tests were conducted at a Mach number of 3.71, and at a Reynolds number of 1.5 or 3.5 x 10^6 per foot. Table 2 illustrates that primary emphasis was placed on the sharp leading edge fin configuration and on the higher Reynolds number data. Prior to deploying the fins, for interaction measurements, the surface heating, surface pressure, and bare sidewall

TABLE 2 DATA SUMMARY

Reynolds Number Per Foot x 10^{-6}	Model Geometry	Fin Angles (degrees)			
		Surface Heat Transfer	Surface Pressure	Pitot Pressure	Surface Oil Flow
3.5	Bare Sidewall	No Fin	No Fin	No Fin	
	Sharp Short Fin	–4,0,2,4,6,8,10, 12,14,16,18,20	–4,0,2,4,6,8,10, 12,14,16,18,20	0,4,8,12, 16,20	4,8,12,16,20
	Sharp Extended Fin	–4,0,2,4,6,8, 10,12,14	–4,0,2,4,6,8,10, 12,14		
	Blunt Fin	2,6,10,14	2,6,10,14		4,12,16
	Blunt 45° Sweep Fin	2,6,10,14	2,6,10,14		
	Blunt 60° Sweep Fin	2,6,10,14	2,6,10,14		
1.5	Bare Sidewall	No Fin	No Fin	No Fin	
	Sharp Short Fin	2,4,6,8,10,12, 14,16,18,20	2,4,6,8,10,12, 14,16,18,20		
	Sharp Extended Fin	2,4,6,8,10,12,14	2,4,6,8,10,12,14		

pitot pressure data were measured. Combining all test points, a total of 54 heat transfer measurements at each of the 194 active thermocouple locations; 62 surface pressure measurements at each of the 197 active surface pressure taps; and 8 pitot rake traverses each containing 18 pitot measurements for each of the 5 pitot probes were obtained. In addition, 8 valid surface oil flow patterns were photographed with each of two cameras. A discussion of the test validity and qualitative results is presented in this section.

2.2.1 Heat Transfer Results - Heat transfer measurements were made on the bare sidewall and with the fins deployed. The accuracy of the measurements and ramifications of the bare plate measurements which are discussed in this section determine the validity of the heat transfer data. Sample machine plots and variations of locally high heating rates are presented to summarize the heat transfer test results.

The accuracy of heat transfer measurements is a function of heating level

as indicated on Table 1. Based on the ranges of heat transfer coefficient magnitude given in Table 1, the accuracy of the data will vary in the interaction region according to the level of local heating rates. Thus, the higher Reynolds number data are consistently more accurate since heat transfer coefficients increase with increased Reynolds number. Similarly, the data accuracy improves with increased fin deflection angle.

Two lower Reynolds number heat transfer data runs were repeated at fin deflection angles of 12 and 18 degrees. Good repeatability was observed in the duplicate heating data. Measured heating rates were within $\pm$ 6% of their average value for the 12 degree fin deflection angle data and within $\pm$ 2.5% for the 18 degree fin deflection angle data. Both sets of data were thus well within the $\pm$ 15% to $\pm$ 20% error band provided by previous NASA experience as listed on Table 1. The error bounds discussed above consist primarily of random error. Wherever possible in this report, heat transfer data are treated in normalized form. The heat transfer coefficient obtained at each thermocouple location is divided by the heat transfer coefficient measured at the same thermocouple location on the bare sidewall. This technique reduces the influence of biased errors on the data.

A sample high Reynolds number bare plate heat transfer coefficient variation is plotted on Figure 11. There is a distinct gradient. However, the data are within $\pm$ 7.94% of their mean value. Thus, the apparent gradient magnitude is comparable to the data accuracy and can be disregarded. This same conclusion was reached for all observed bare plate heating gradients. This is indicated on Table 3 which tabulates characteristic measured transfer coefficient magnitudes and deviations observed.

A sample run to run variation of normalized heat transfer coefficient for a thermocouple which was always outside of the interaction region is illustrated in Figure 12. The maximum deviation from the mean value is $\pm$ 3.4% for the high Reynolds number data. The corresponding low Reynolds number data deviation is within $\pm$ 9.4% of the mean value.

From considerations of the data accuracy and consistency it is concluded that, to within error bounds somewhat less than those indicated by previous NASA experience, the normalized heat transfer coefficient data is sufficiently accurate for detailed correlation and comparison with analysis. Furthermore, to within data accuracy the bare plate data are considered uniform.

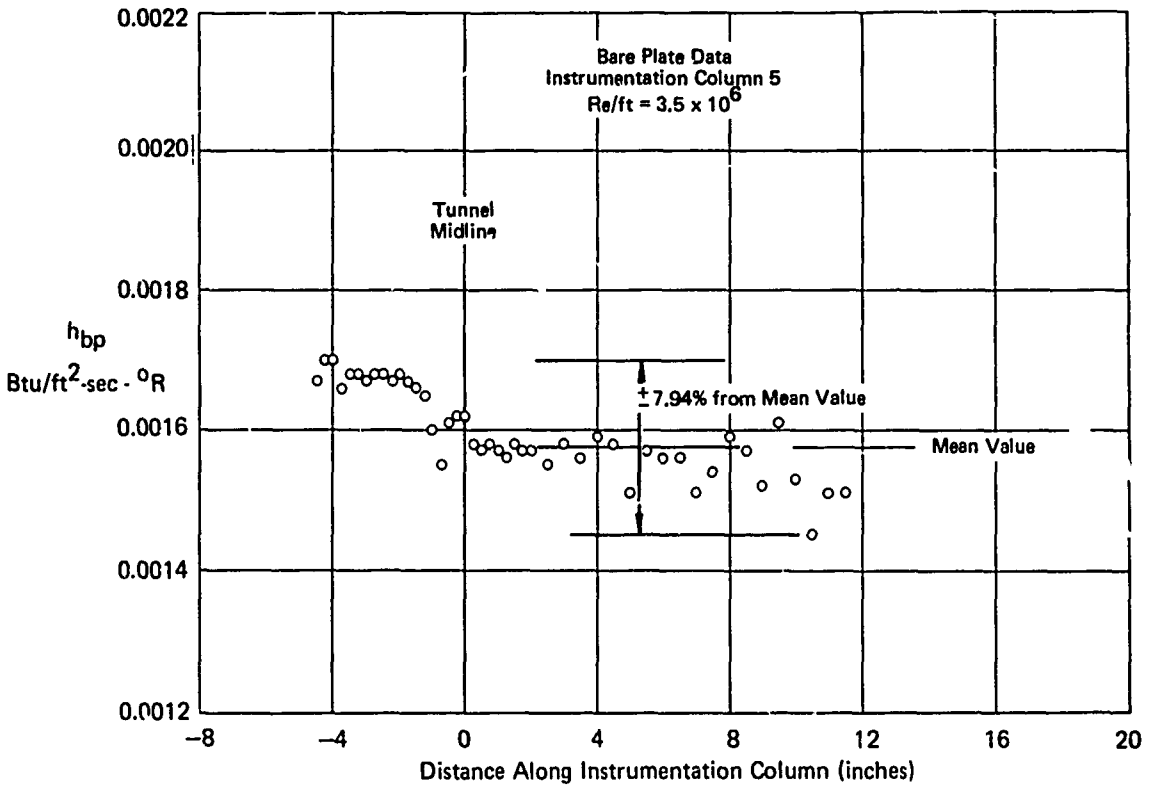

FIGURE 11 SAMPLE BARE PLATE HEATING VARIATION

TABLE 3
BARE PLATE HEATING

	Re = 1.5 x 10^6/ft		Re = 3.5 x 10^6/ft	
Column	Mean Value of h_{bp} (Btu/ft^2-sec-°R)	Maximum Deviation from Mean Value of h_{bp} (%)	Mean Value of h_{bp} (Btu/ft^2-sec-°R)	Maximum Deviation from Mean Value of h_{bp} (%)
1	0.00080	13.75	0.00163	8.59
3	0.00080	16.25	0.00163	7.36
5	0.00082	14.63	0.00158	7.94
7	0.00078	5.81	0.00152	5.57
Average	0.00080	12.61	0.00159	7.36

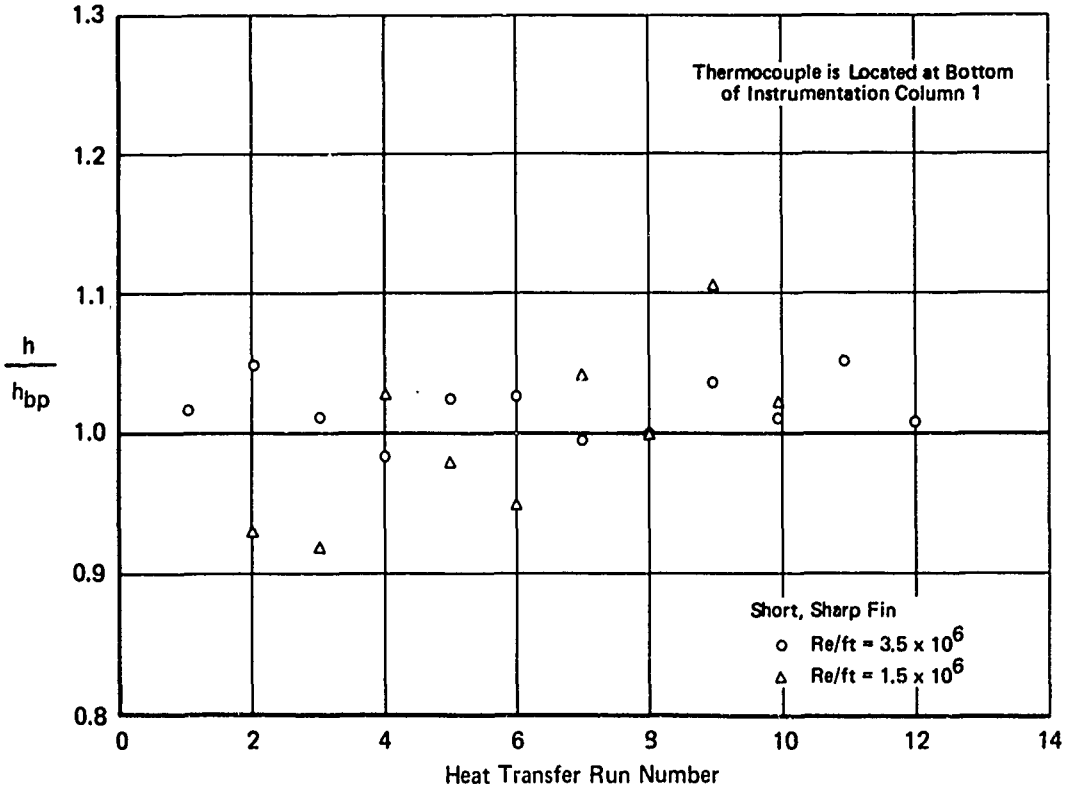

FIGURE 12 RUN TO RUN HEATING VARIATION

Selected machine plots of normalized heat transfer coefficient variation across the interaction region along instrumentation columns from the fin surface outboard are illustrated in Figure 13. The location and orientation of the instrumentation columns are illustrated in Figure 6. The data presented were obtained at both high and low Reynolds number, for all fin configurations and at selected fin deflection angles.

The sample machine plots of heating data were selected to illustrate the influence of fin deflection angle on sharp fin heating data, the influence of distance downstream from the sharp fin leading edge, the influence of Reynolds number, and the influence of fin geometry. It is apparent from this sample data that the highest heating along an instrumentation column occurs very close to the fin surface, and that this local peak heating magnitude for sharp leading edge fins increases with distance aft. The calculated impinging shock wave locations are shown for reference on the sharp fin data. It is evident that the interaction region influences the surface heating for a large distance upstream and outboard of the shock waves

Local peak heating variations downstream of the fin leading edge for both the 3.5 and 1.5 x 10^6 Reynolds number per foot cases are illustrated in Figure 14. All fin deflection angle data are shown and the data from both short and extended sharp leading edge fins are plotted. Both plots indicate that the maximum value of local peak heating lies a considerable distance downstream of the instrumented region since the peak heating gradient in the freestream direction is large and appears to be decreasing at a slow rate.

2.2.2 Surface Pressure Results - Surface pressure measurements were made on the bare sidewall and with fins deployed. The accuracy of the measurements, ramifications of the bare plate measurements, sample machine plots and peak pressure variations are discussed in this section.

The absolute surface pressure measurement accuracy indicated in Table 1 is $\pm$ 0.025 psia. Figure 15 is a plot of a sample bare plate surface pressure variation at high Reynolds number. It indicates that a surface pressure gradient exists on the tunnel sidewall. The pressure variation is $\pm$ 5.91% of the mean value which in terms of absolute error is essentially equal to the measurement accuracy. A similar result was obtained for low Reynolds number data. All bare plate pressure levels and deviations are tabulated in Table 4. Thus, to within measurement accuracy, the bare sidewall surface pressure is constant in the instrumented region. Figure 16 presents a run to run

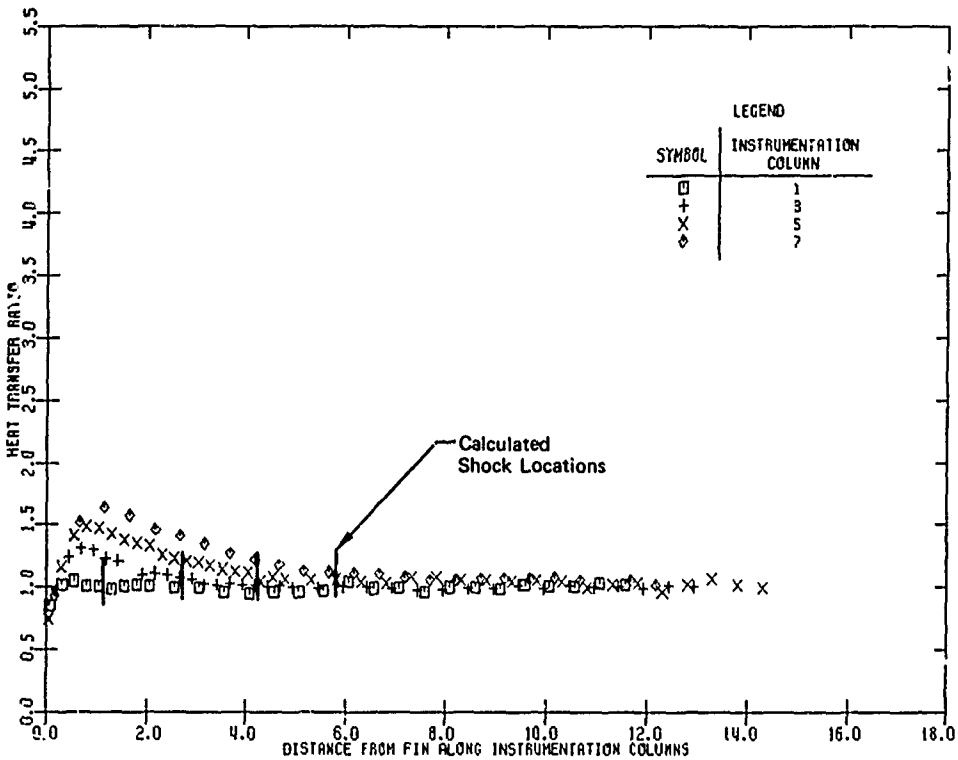

a. Short, Sharp Fin, $\alpha = 6^{o}$, Re/Ft = 3.5×10^{6}

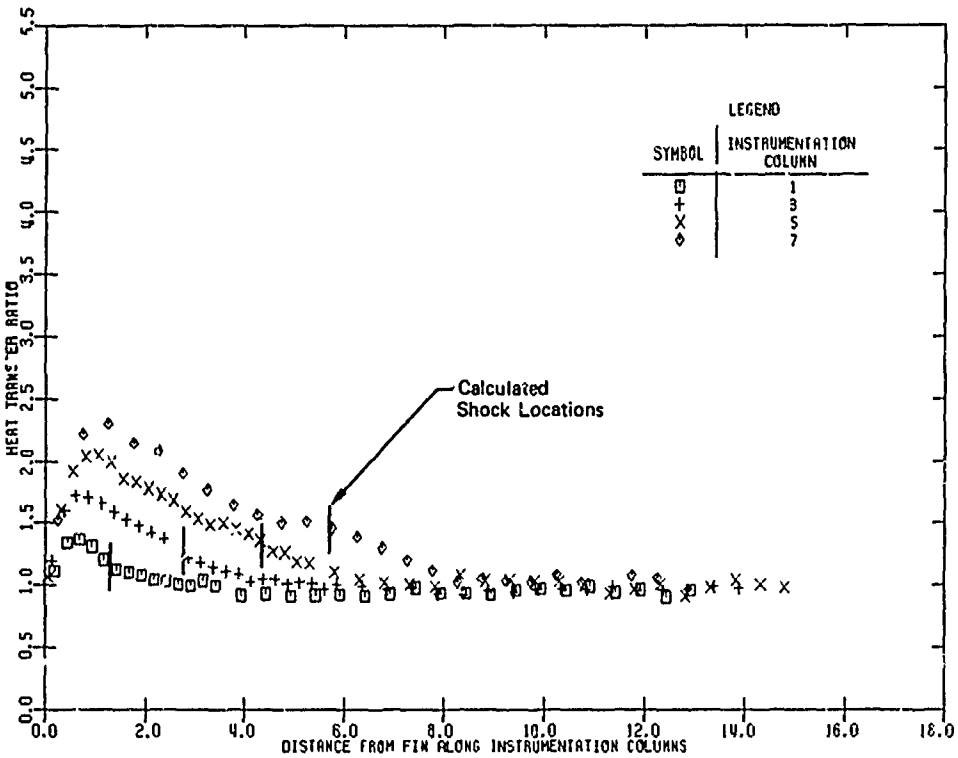

b. Short, Sharp Fin, $\alpha = 10^{o}$, Re/Ft = 3.5×10^{6}

FIGURE 13 SAMPLE SURFACE HEAT TRANSFER COEFFICIENT MACHINE PLOTS

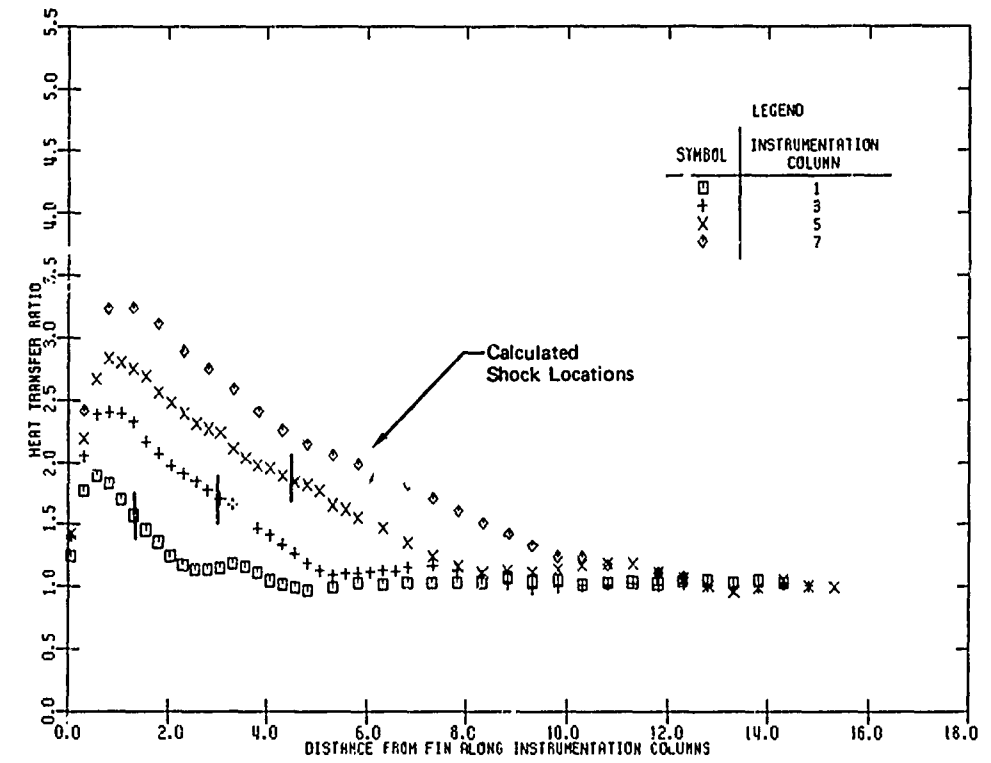

c. Short, Sharp Fin, $\alpha = 14^{o}$, Re/Ft = 3.5×10^{6}

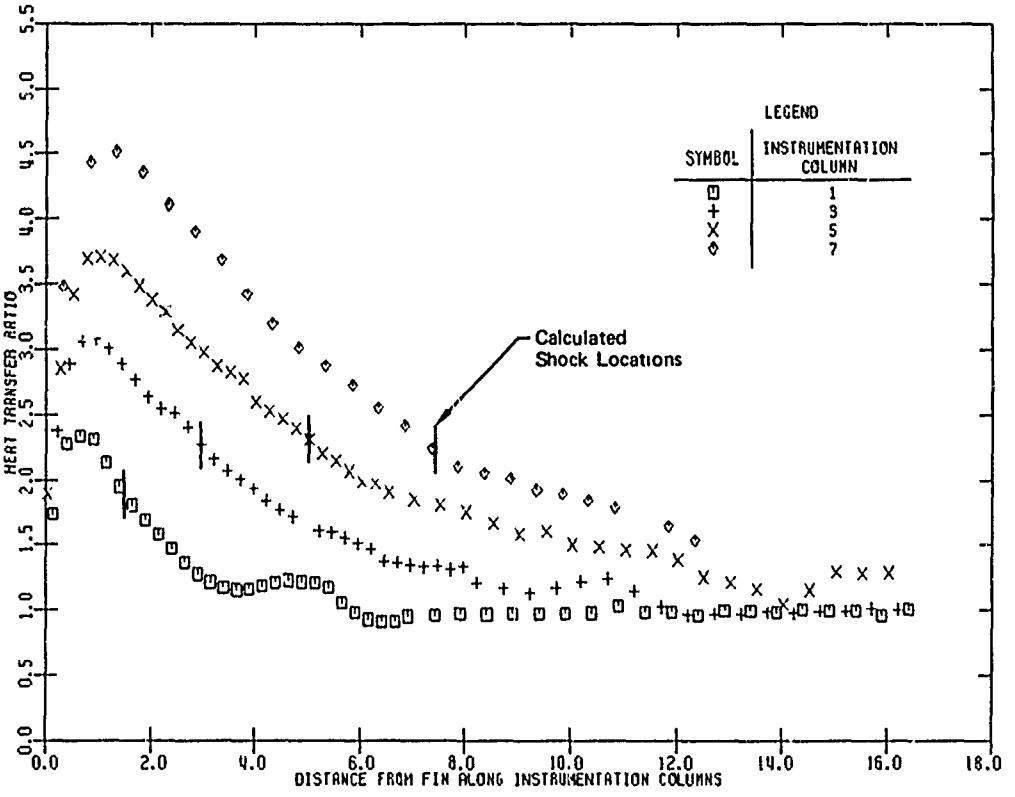

d. Short, Sharp Fin, $\alpha = 20^{o}$, Re/Ft = 3.5×10^{6}

FIGURE 13 SAMPLE SURFACE HEAT TRANSFER COEFFICIENT MACHINE PLOTS (Continued)

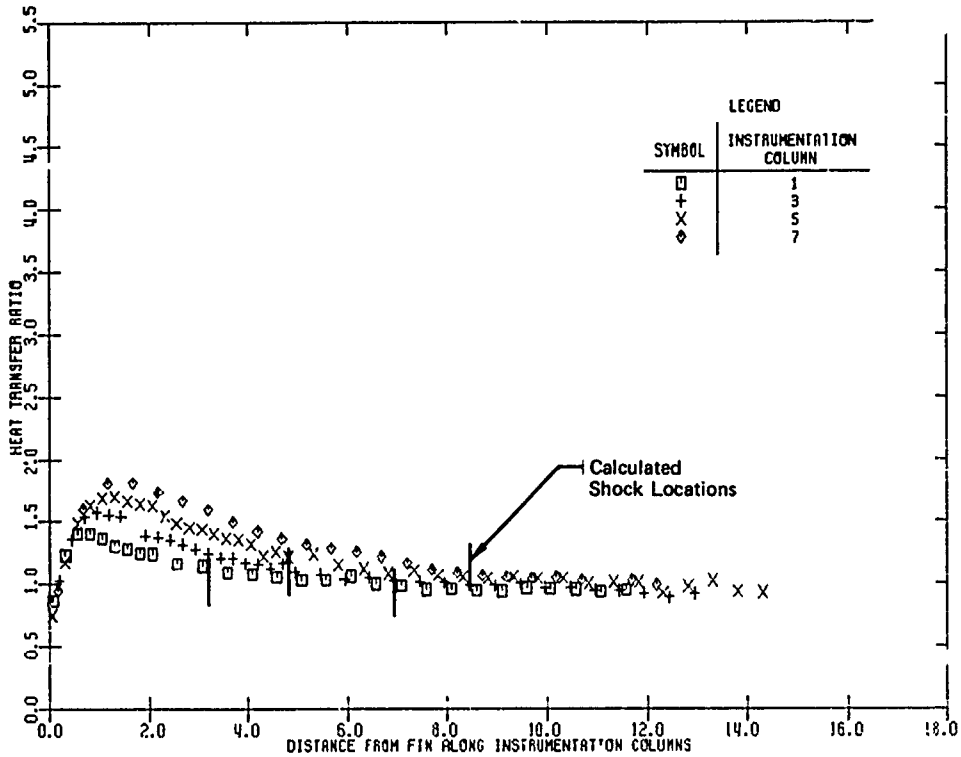

e. Extended, Sharp Fin, $\alpha = 6^{o}$, Re/Ft = 3.5×10^{6}

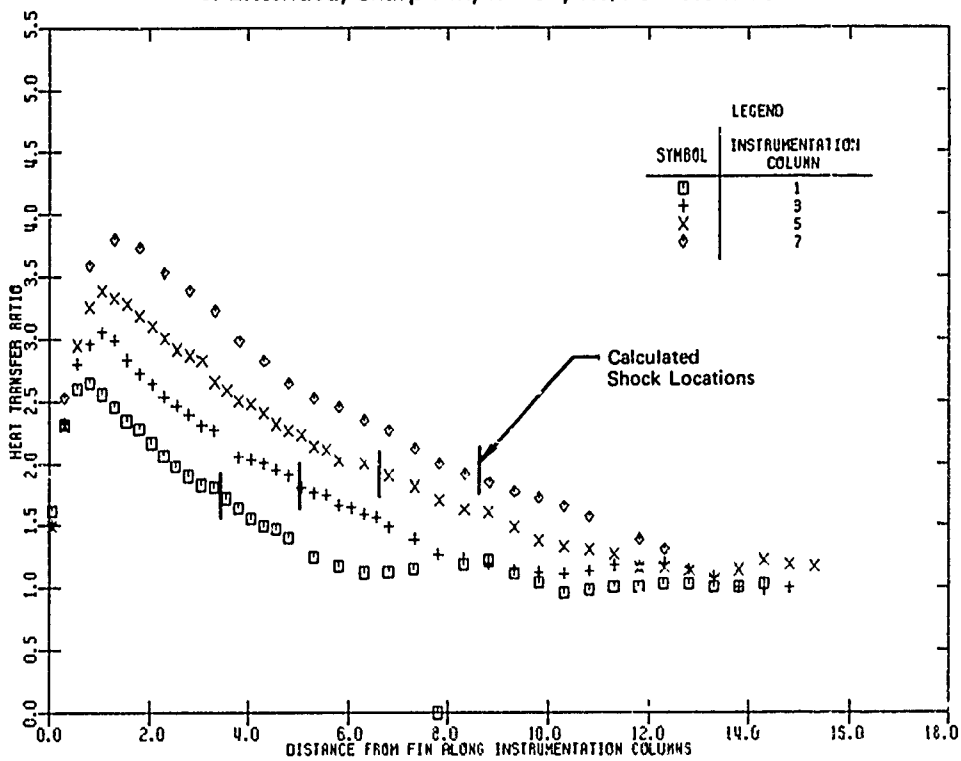

f. Extended, Sharp Fin, $\alpha = 14^{o}$, Re/Ft = 3.5×10^{6}

FIGURE 13 SAMPLE SURFACE HEAT TRANSFER COEFFICIENT MACHINE PLOTS (Continued)

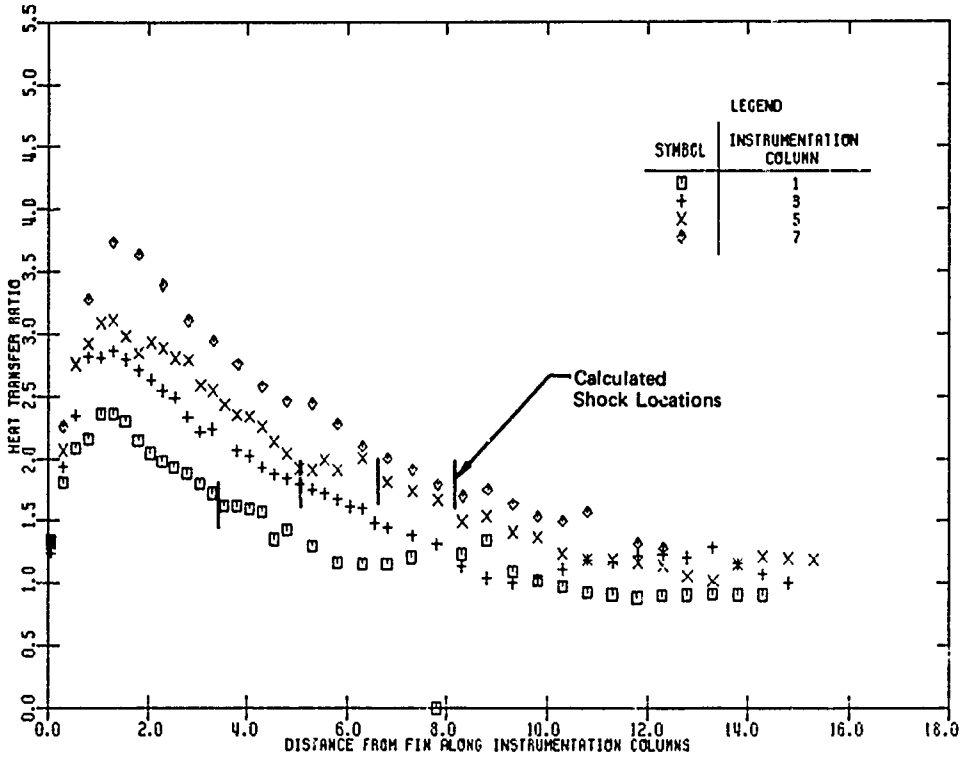

g. Extended, Sharp Fin, $\alpha = 14^{o}$, Re/Ft = 1.5×10^{6}

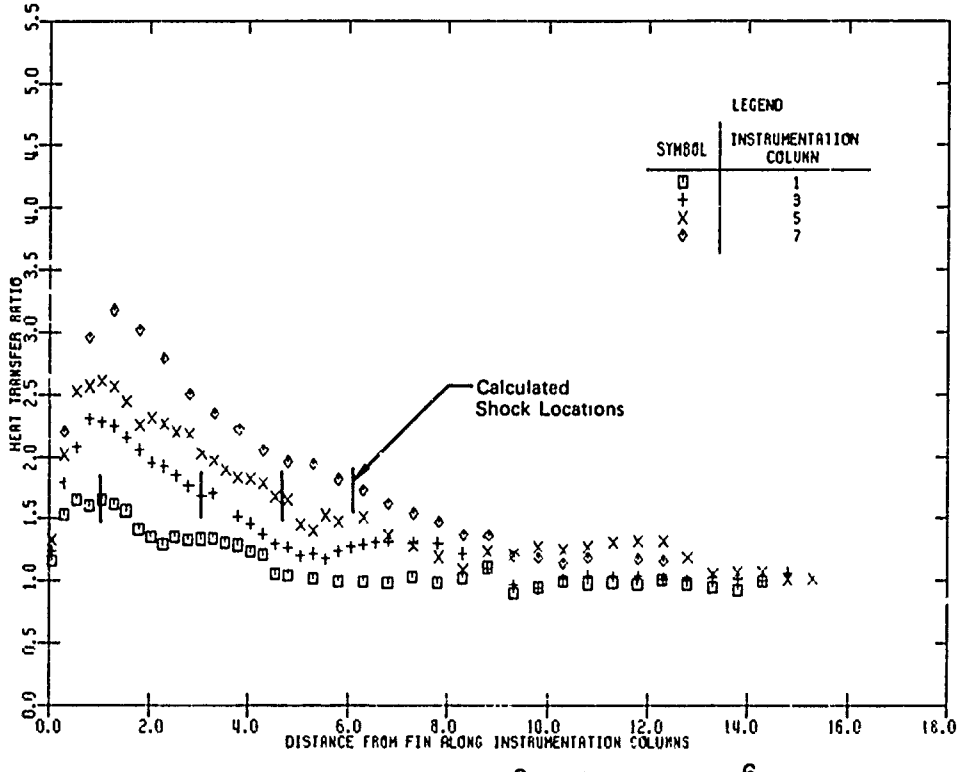

h. Short, Sharp Fin, $\alpha = 14^{o}$, Re/Ft = 1.5×10^{6}

FIGURE 13 SAMPLE SURFACE HEAT TRANSFER COEFFICIENT MACHINE PLOTS (Continued)

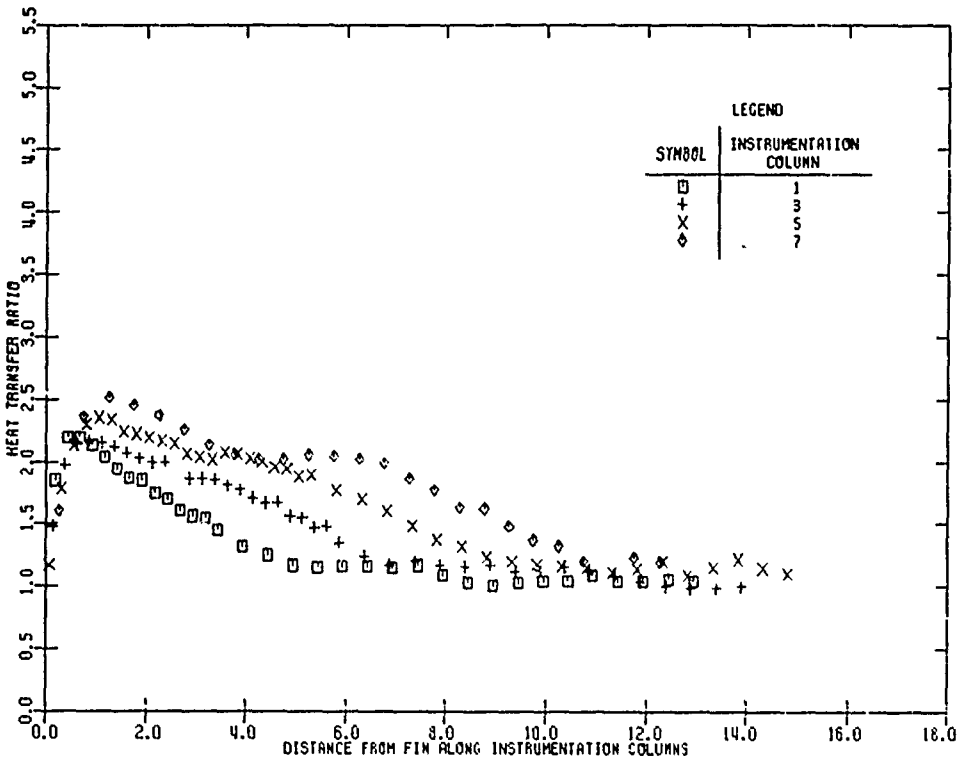

i. Blunt, No Sweep Fin, $\alpha = 10^{o}$, Re/Ft = 3.5×10^{6}

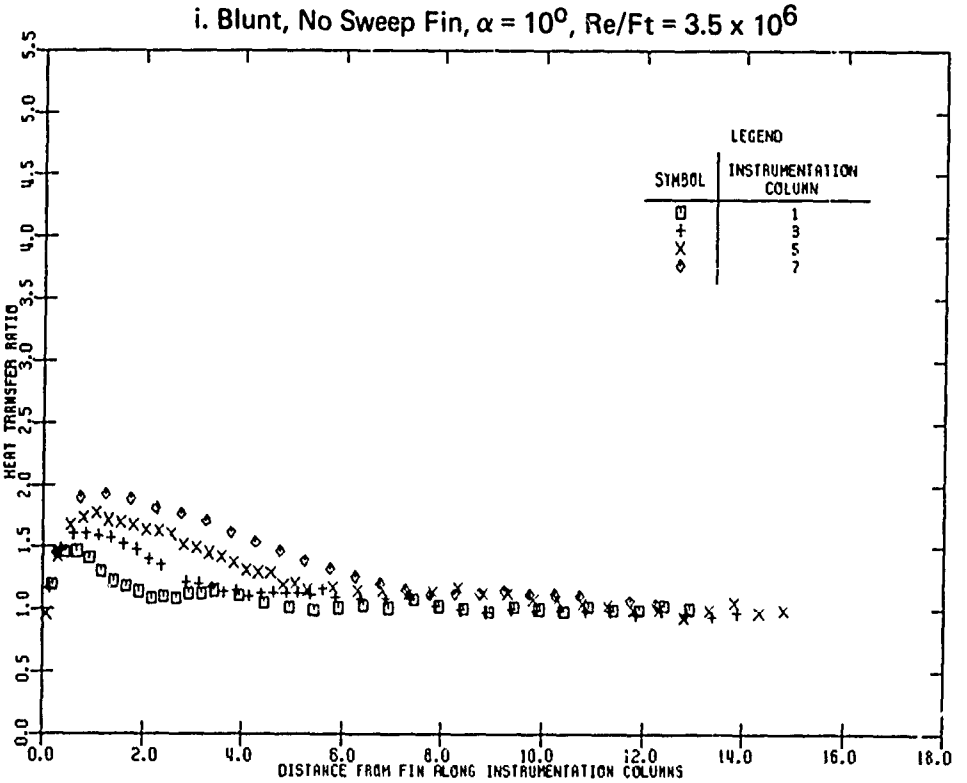

j. Blunt, 45^{o} Sweep Fin, $\alpha = 10^{o}$, Re/Ft = 3.5×10^{6}

FIGURE 13 SAMPLE SURFACE HEAT TRANSFER COEFFICIENT MACHINE PLOTS (Continued)

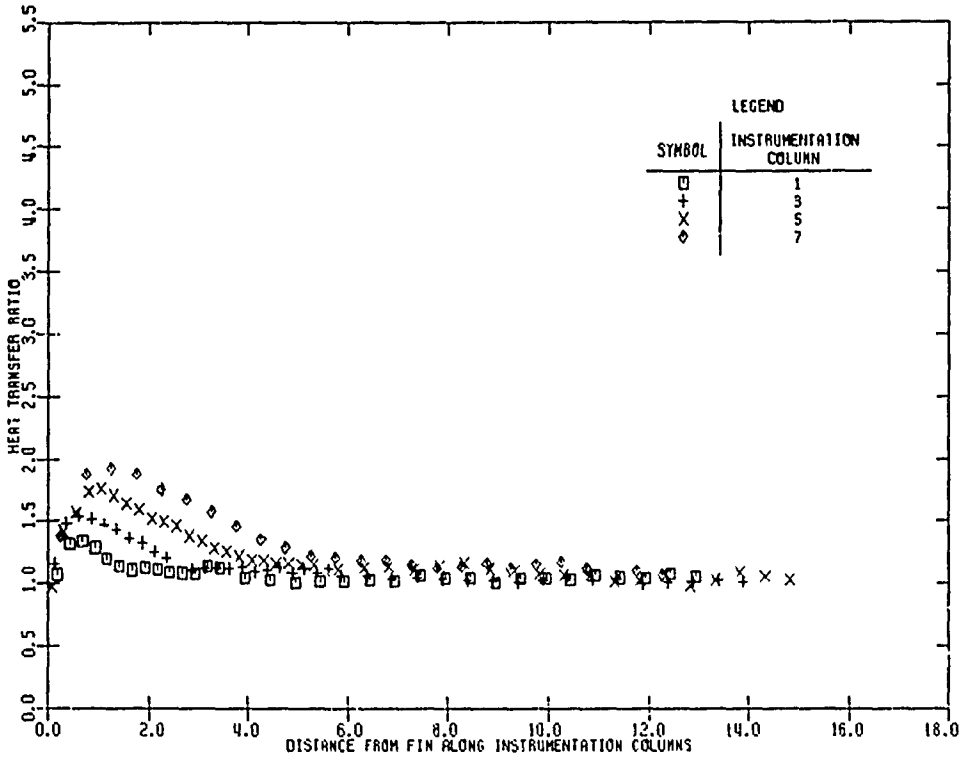

k. Blunt, 60° Sweep Fin, $\alpha = 10^{o}$, Re/Ft = 3.5×10^{6}

FIGURE 13 SAMPLE SURFACE HEAT TRANSFER COEFFICIENT MACHINE PLOTS (Concluded)

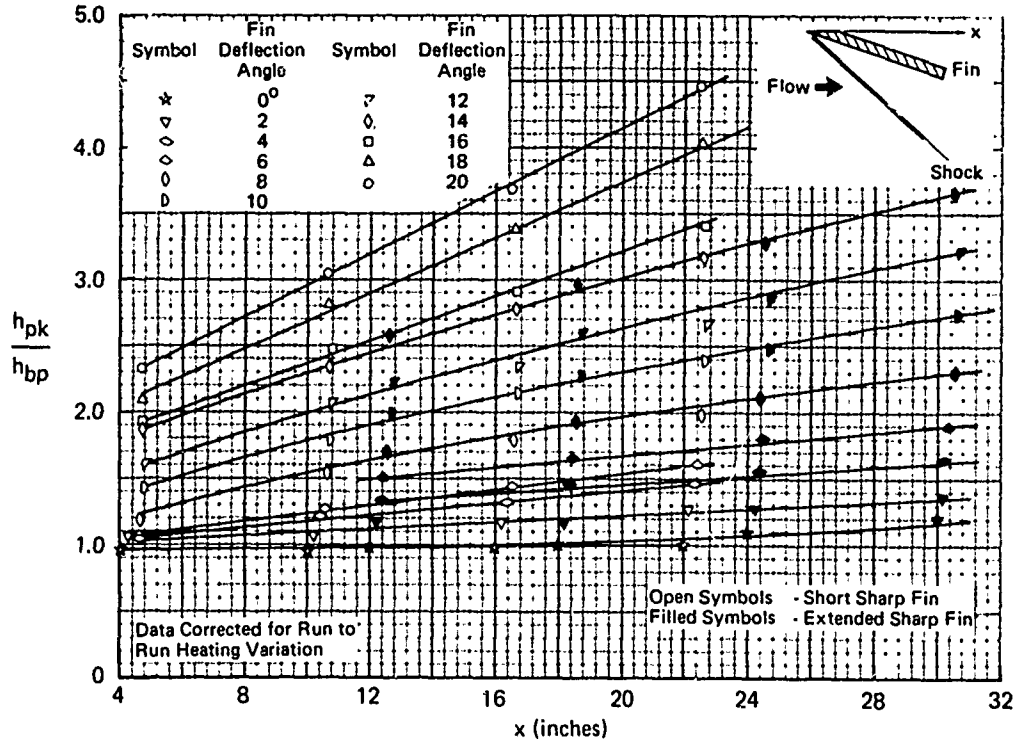

a. Re/Ft = 3.5×10^6

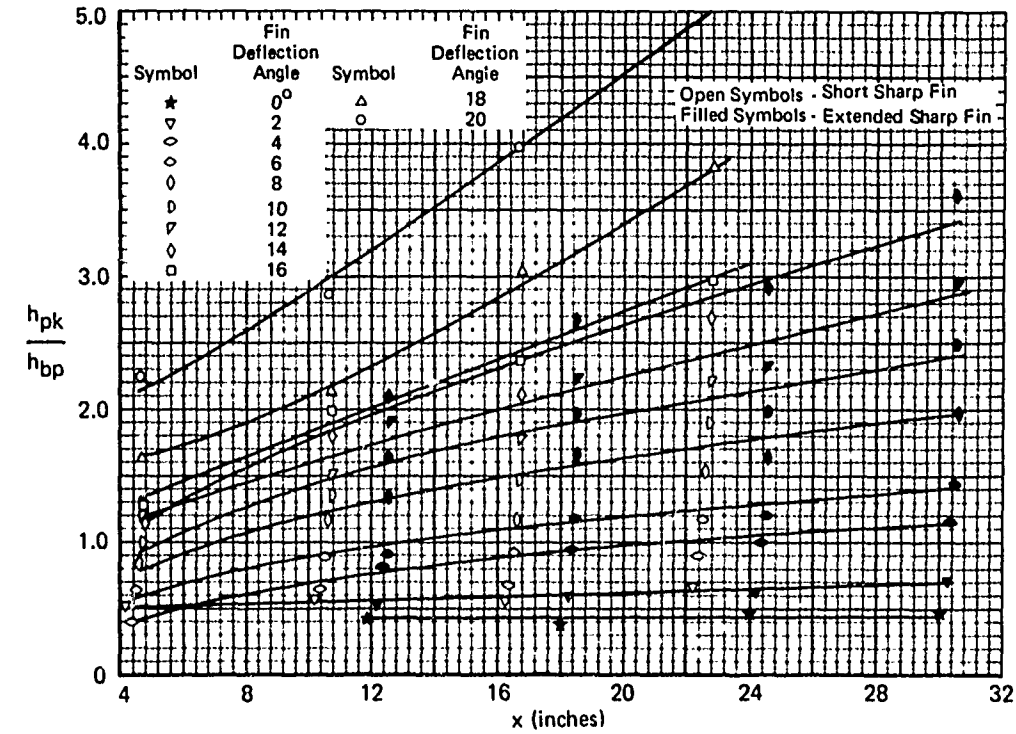

b. Re/Ft = 1.5×10^6

FIGURE 14 PEAK HEATING VARIATION WITH DISTANCE FROM FIN LEADING EDGE

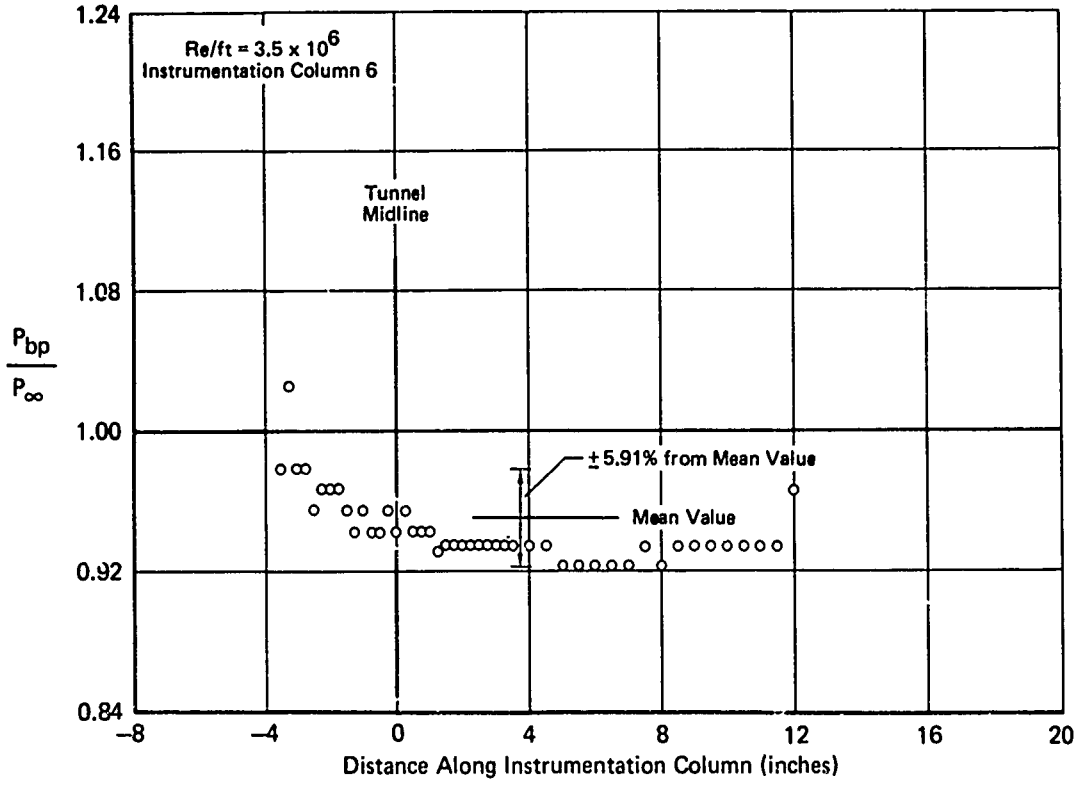

FIGURE 15 SAMPLE BARE PLATE PRESSURE VARIATION

TABLE 4
BARE PLATE PRESSURE LEVEL

	$Re = 1.5 \times 10^6$/ft		$Re = 3.5 \times 10^6$/ft	
Column	Mean Value of P_{bp}/P_∞	Maximum Deviation from Mean Value of P_{bp}/P_∞ (%)	Mean Value of P_{bp}/P_∞	Maximum Deviation from Mean Value of P_{bp}/P_∞ (%)
2	0.975	3.79	1.005	2.84
4	0.933	14.36	0.961	4.06
6	0.952	7.04	0.950	5.91
8	0.912	2.91	0.935	1.28
Average	0.943	7.02	0.963	3.52

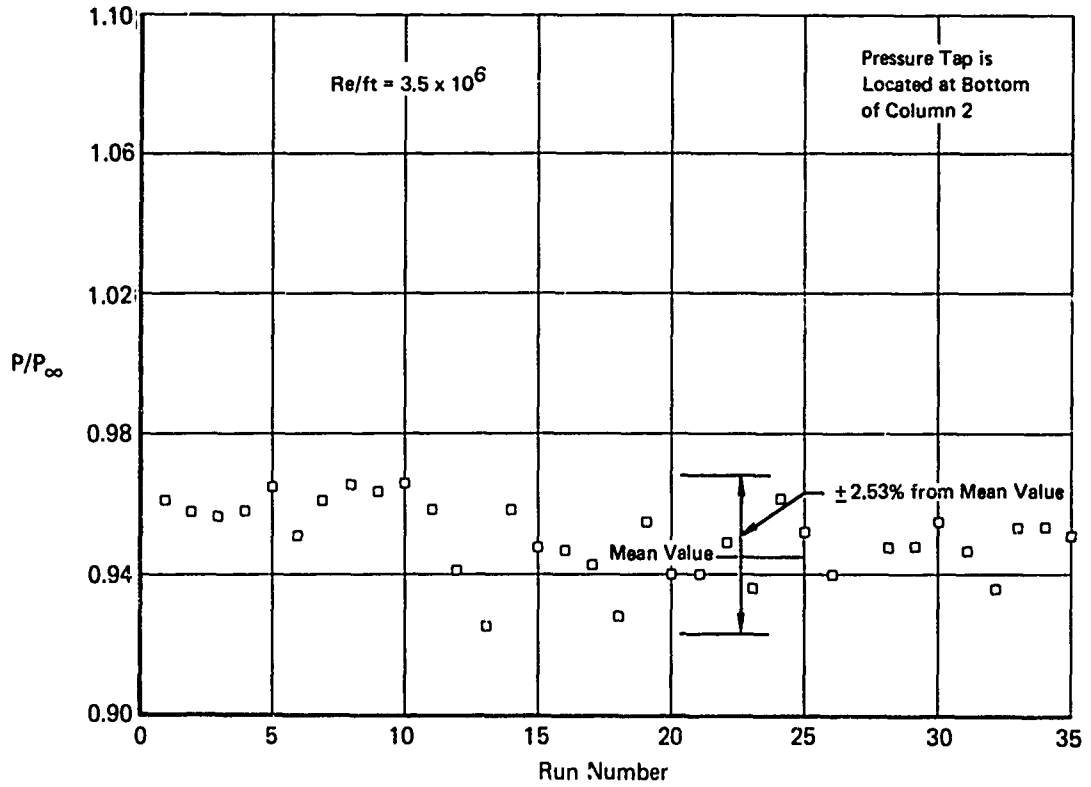

FIGURE 16 RUN TO RUN PRESSURE VARIATION

surface pressure reading from a surface pressure tap which was always in the undisturbed stream regardless of fin deflection angle. The run to run variation in pressure reading was $\pm$ 2.53% of the mean value which to within data accuracy is constant. Thus, to within data measurement accuracy, the bare sidewall surface pressure can be considered constant spatially and independent of tunnel run. Pressures measured upstream of the interaction region at locations depicted in Figure 6 concur with these results.

Sample machine plots of surface pressure variation are illustrated in Figure 17. The selected cases plotted are for both high and low Reynolds number, and all fin configurations at selected fin deflection angles. The data shows the pressure variation across the interaction region from the fin surface outboard along instrumentation columns defined in Figure 6. The column number 8 data decrease rapidly in the vicinity of the fin. This data behavior is caused by the Prandtl-Meyer expansion eminating from the fin base. This spurious data is not characteristic of the interaction region with longer fins. The data on columns 2, 4, and 6 are not affected by the fin base expansion and indicate that the peak surface pressure at any axial station occurs at the fin-plate interface. The sharp fin peak surface pressure increases with distance aft and never reaches the inviscid pressure level calculated by oblique shock relations. The location of the impinging shock wave has been superimposed on sharp fin data for reference. Since the surface pressure disturbance propagates considerably outboard of the sharp fin inviscid shock location, the surface pressure data support the same large outboard influence observed from the heat transfer data in Figure 13. The surface pressure appears to attain a pseudo plateau level outboard of the shock wave before decreasing to freestream values. For the higher fin deflection angle cases, a small dip in the plateau can be observed. At somewhat smaller fin deflection angles the plateau pressure is more nearly flat, and at even smaller fin deflection angles the plateau does not exist.

Plots of the sharp fin peak surface pressure variation with distance aft are illustrated in Figure 18. In each case the peak pressure occurred at or near the fin surface and increased with distance aft. This data trend is shown in Figure 18a for the high Reynolds number data and in Figure 18b for the low Reynolds number data. Data shown on both these figures incorporate all fin deflection angles from both the short and extended sharp leading edge fins.

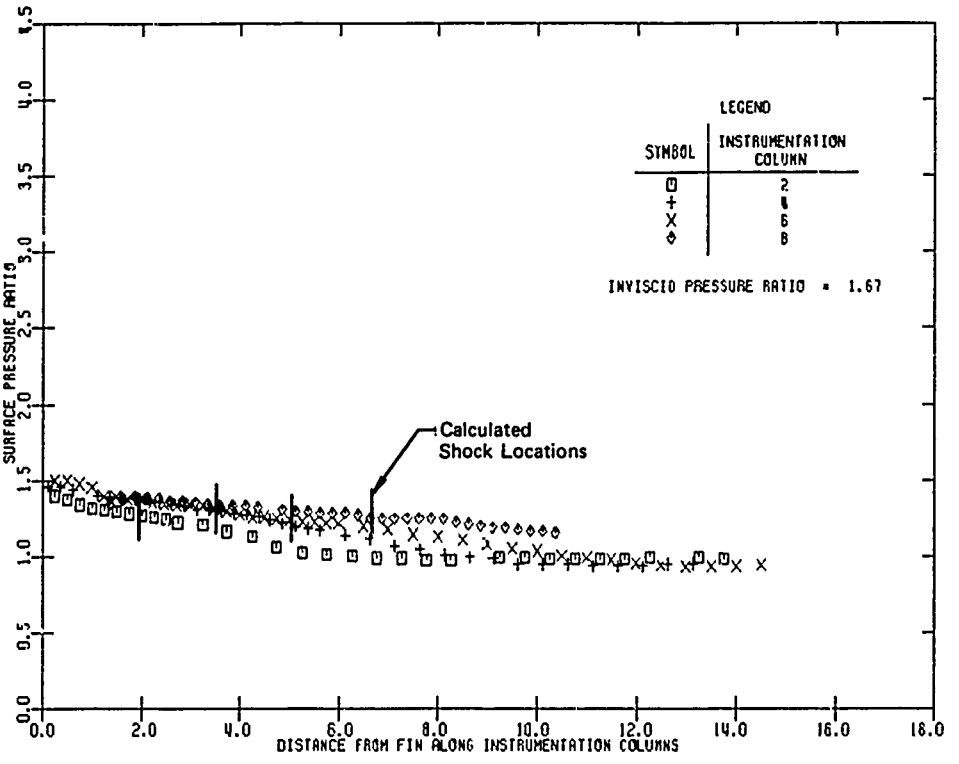

a. Short, Sharp Fin, $\alpha = 6^{o}$, Re/Ft = 3.5×10^{6}

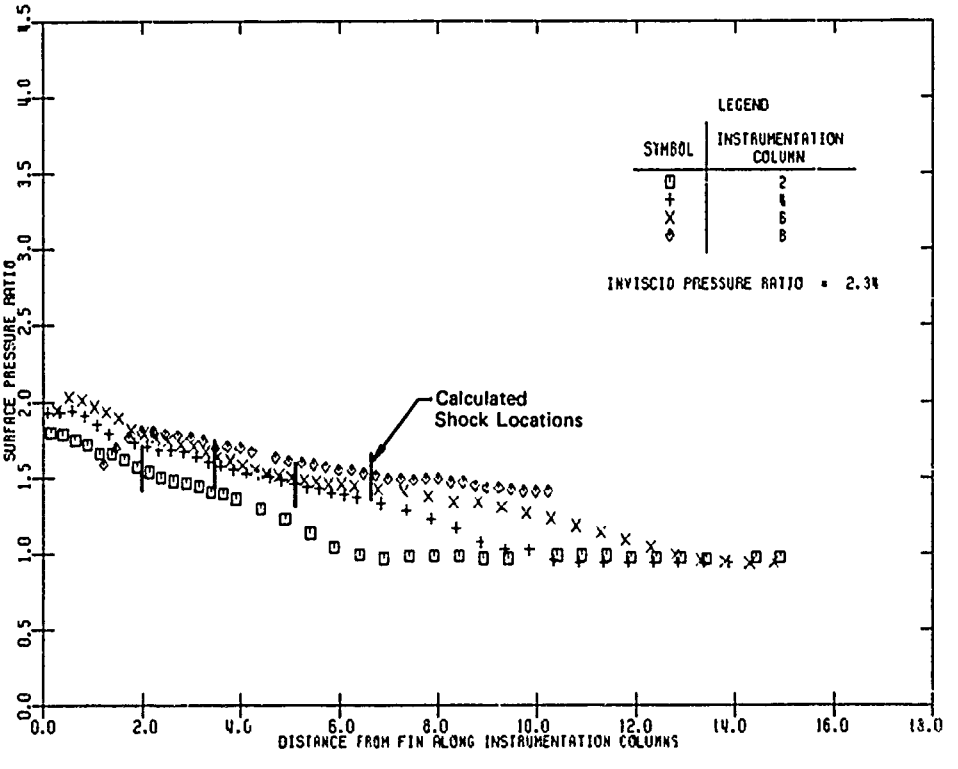

b. Short, Sharp Fin, $\alpha = 10^{o}$, Re/Ft = 3.5×10^{6}

FIGURE 17 SAMPLE SURFACE PRESSURE MACHINE PLOTS

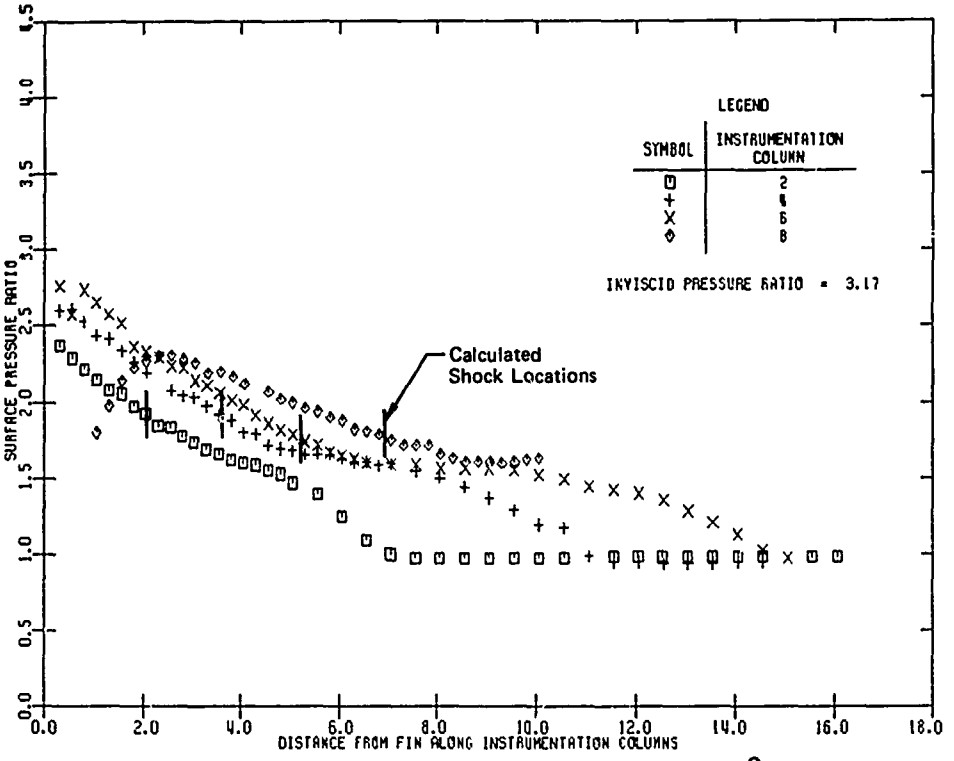

c. Short, Sharp Fin, $\alpha = 14^{o}$, Re/Ft = 3.5×10^{6}

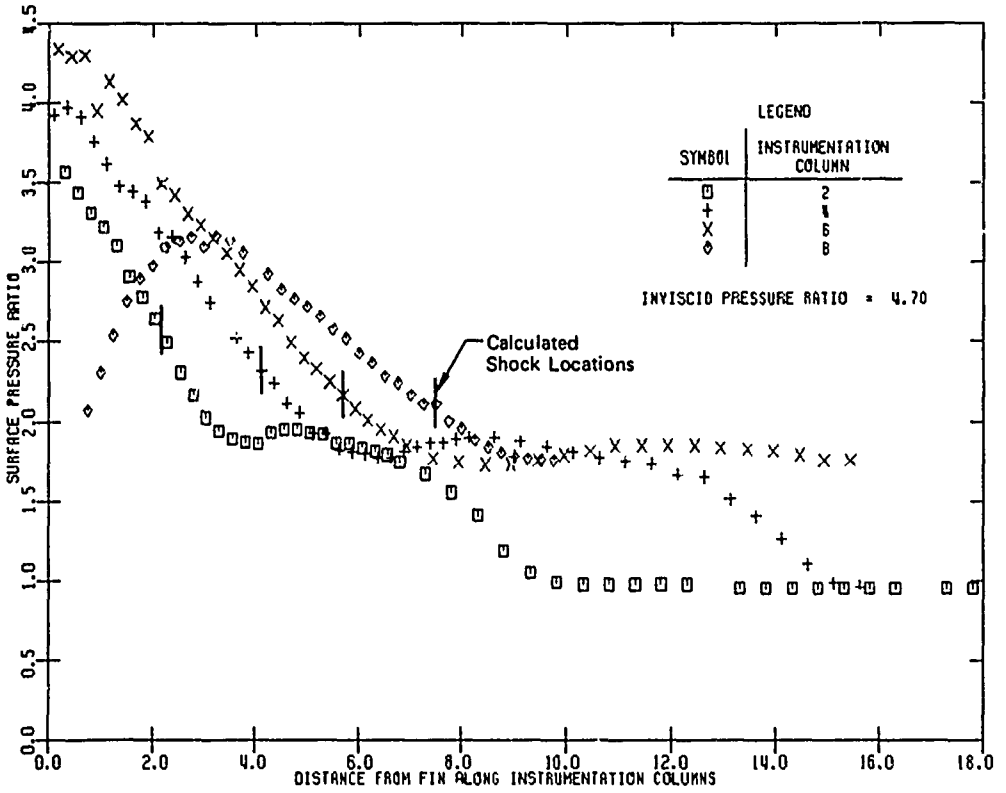

d. Short, Sharp Fin, $\alpha = 20^{o}$, Re/Ft = 3.5×10^{6}

FIGURE 17 SAMPLE SURFACE PRESSURE MACHINE PLOTS (Continued)

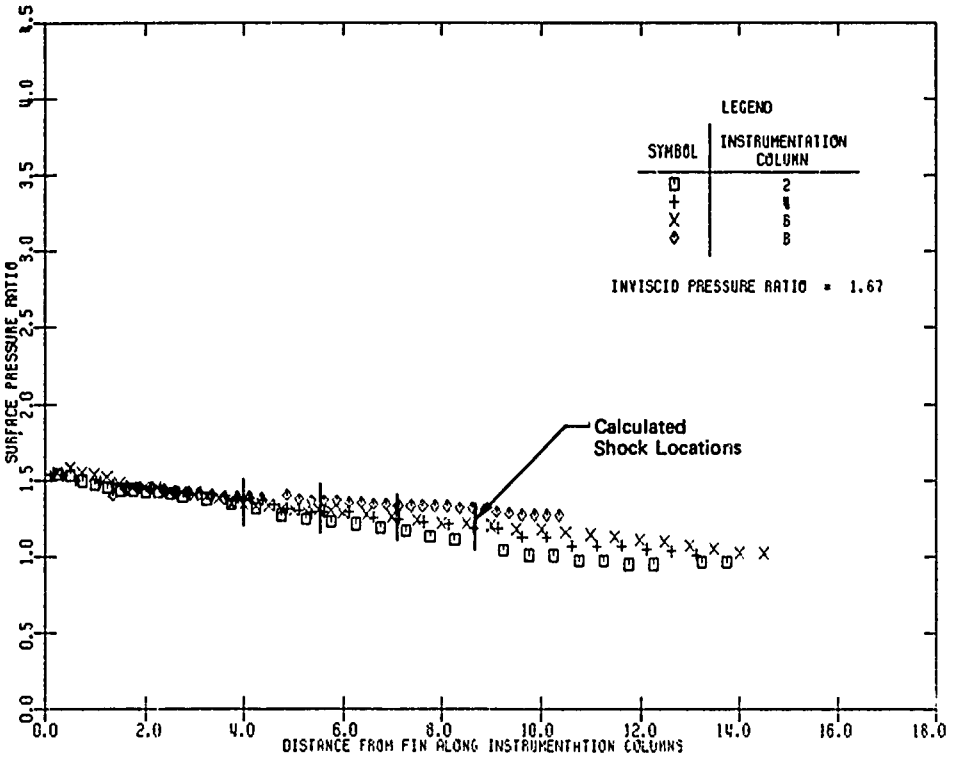

e. Extended, Sharp Fin, $\alpha = 6^{o}$, Re/Ft = 3.5 x 10^{6}

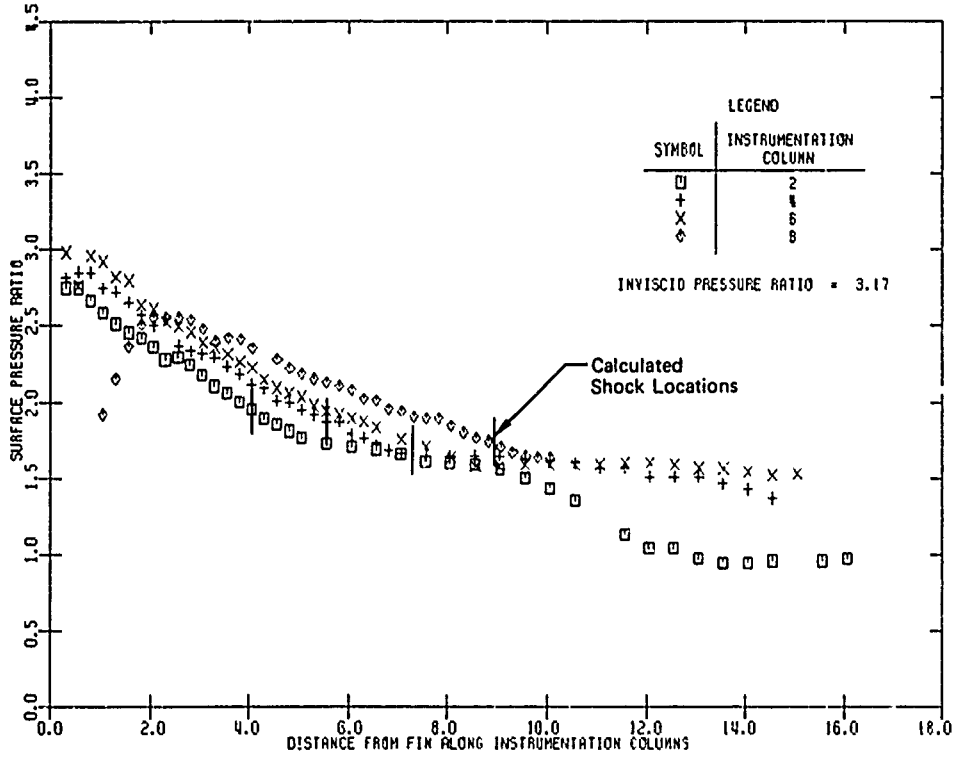

f. Extended, Sharp Fin, $\alpha = 14^{o}$, Re/Ft = 3.5 x 10^{6}

FIGURE 17 SAMPLE SURFACE PRESSURE MACHINE PLOTS (Continued)

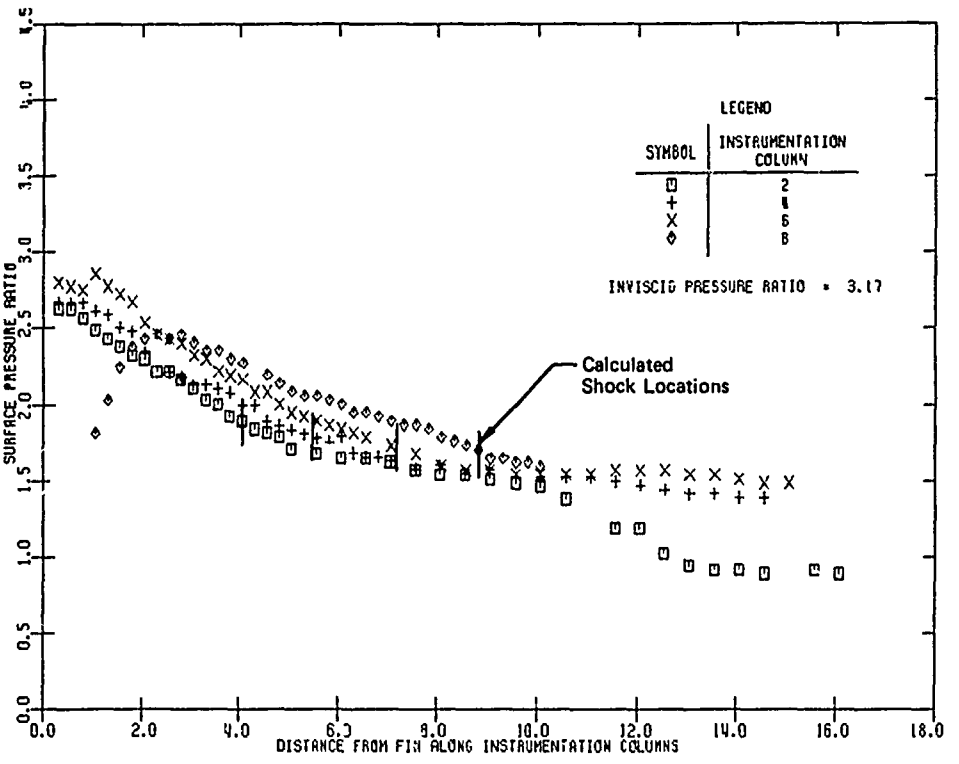

g. Extended, Sharp Fin, $\alpha = 14^{o}$, Re/Ft = 1.5×10^{6}

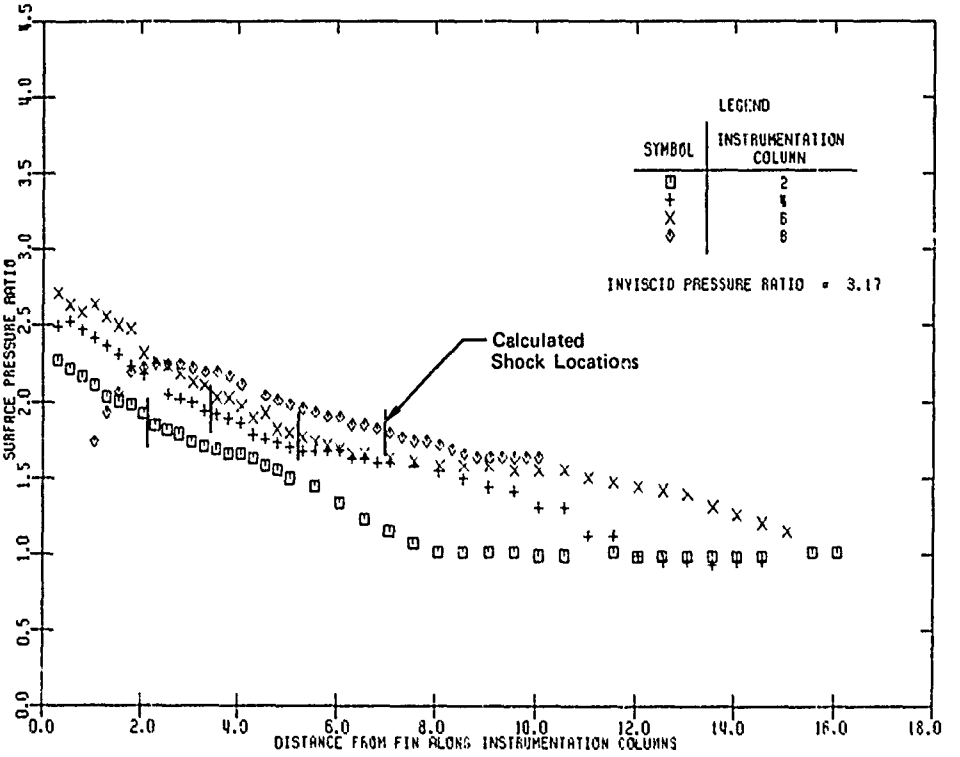

h. Short, Sharp Fin, $\alpha = 14^{o}$, Re/Ft = 1.5×10^{6}

FIGURE 17 SAMPLE SURFACE PRESSURE MACHINE PLCTS (Continued)

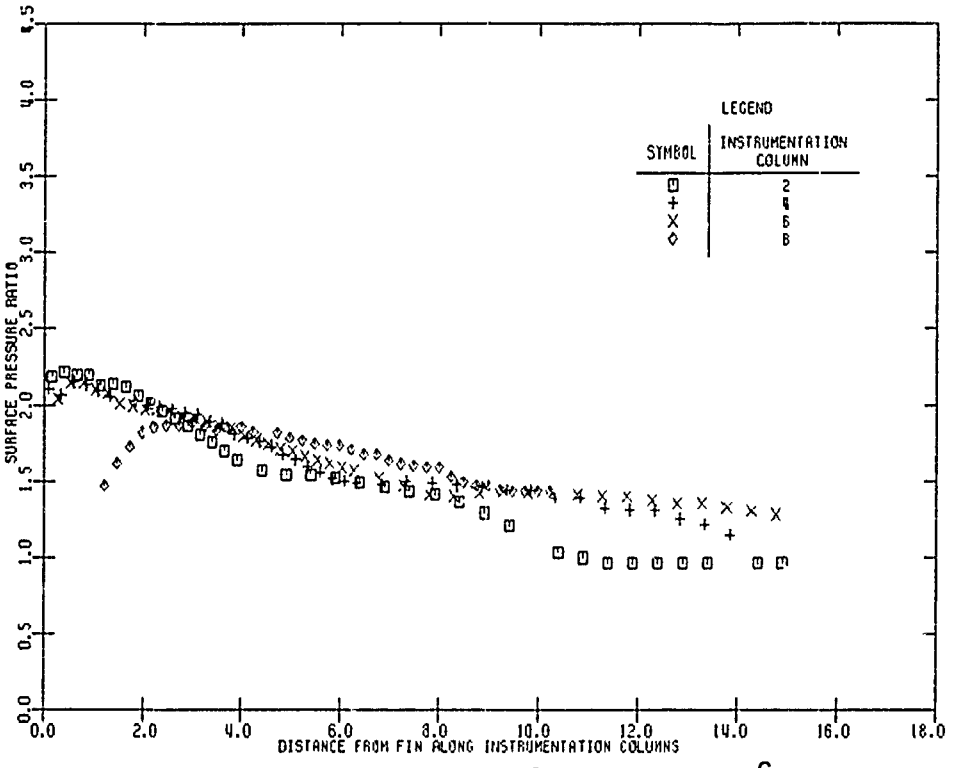

i. Blunt, No Sweep Fin, $\alpha = 10^{o}$, Re/Ft = 3.5×10^{6}

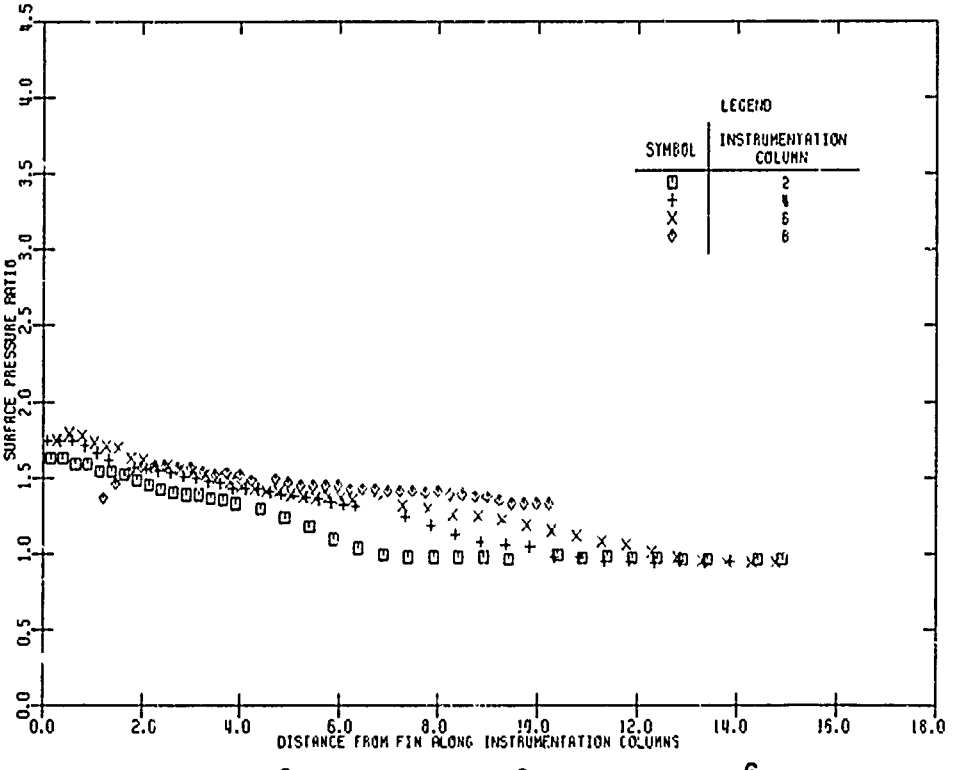

j. Blunt, 45^{o} Sweep Fin, $\alpha = 10^{o}$, Re/Ft = 3.5×10^{6}

FIGURE 17 SAMPLE SURFACE PRESSURE MACHINE PLOTS (Continued)

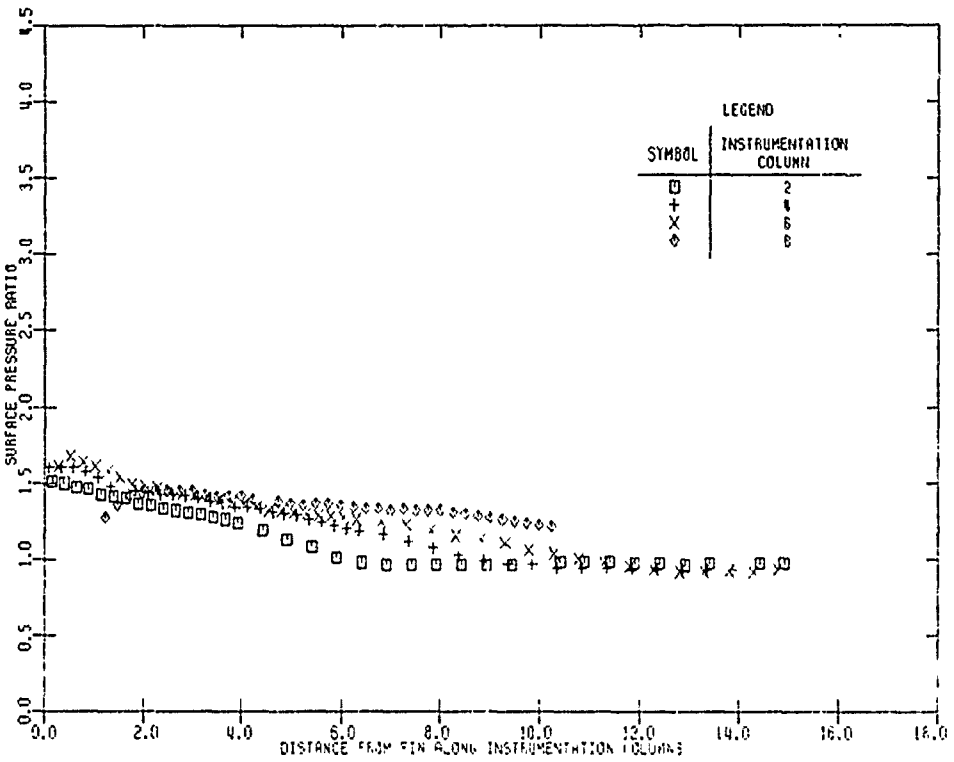

k. Blunt, 60° Sweep Fin, $\alpha = 10°$, Re/Ft = 3.5×10^6

FIGURE 17 SAMPLE SURFACE PRESSURE MACHINE PLOTS (Concluded)

Some surface pressure measurements on the fin surface were greater than the measured values on the wall surface and greater than the inviscid values calculated by oblique shock equations. Other fin surface pressure measurements were less than wall surface values and those calculated by oblique shock equations. Due to the sparse instrumentation density on the fin surface, no data trends were observed. The fin surface pressure variations were larger than the instrumentation accuracy bandwidths and are presented in Section 3.3.1.2, Figure 43.

2.2.3 Pitot Pressure Results - Pitot pressure profiles were obtained at the fixed locations indicated in Figures 6 and 9 throughout the fin deflection angle range indicated in Table 2. The pitot pressure measurement accuracy indicated in Table 1 does not incorporate probe losses. Figure 19 presents the yaw sensitivity measured with a similar pitot probe at Mach 3.71 and reported in Reference 5. The data indicate a rather large yaw sensitivity. Since local interaction region flow deflection angles are not known, the probe data must be considered qualitative, or the possibility of a large pitot pressure error must be accepted. Since the rake was positioned approximately at

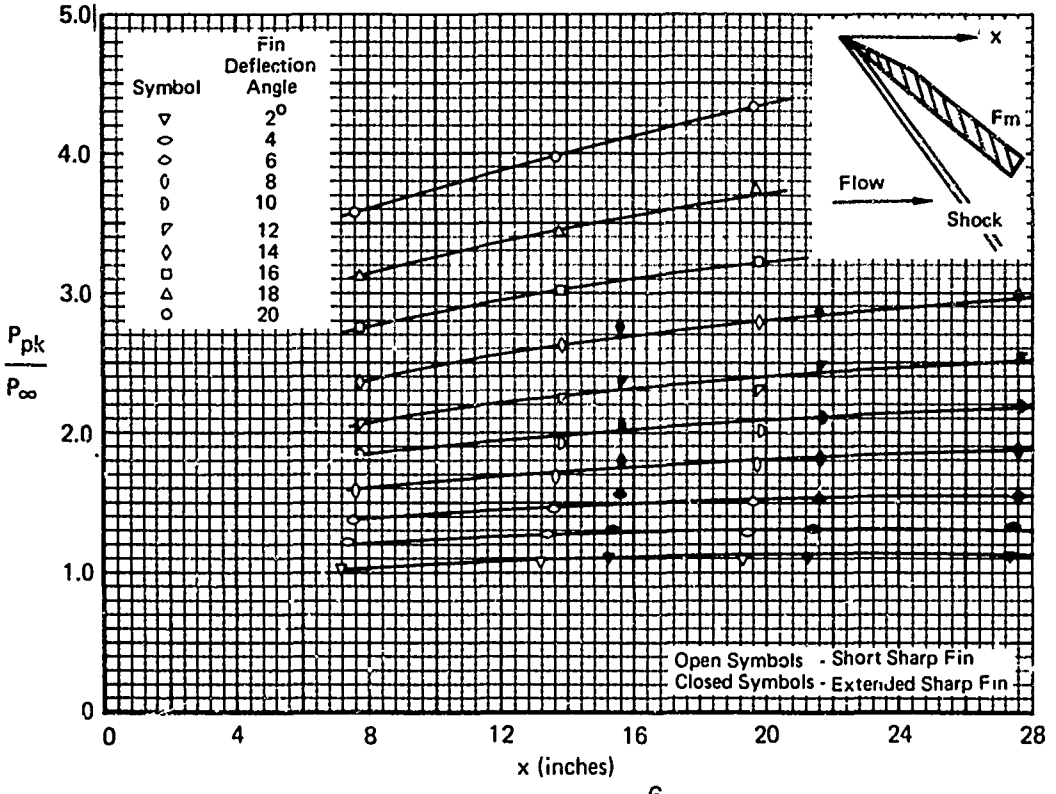

a. Re/Ft = 3.5×10^6

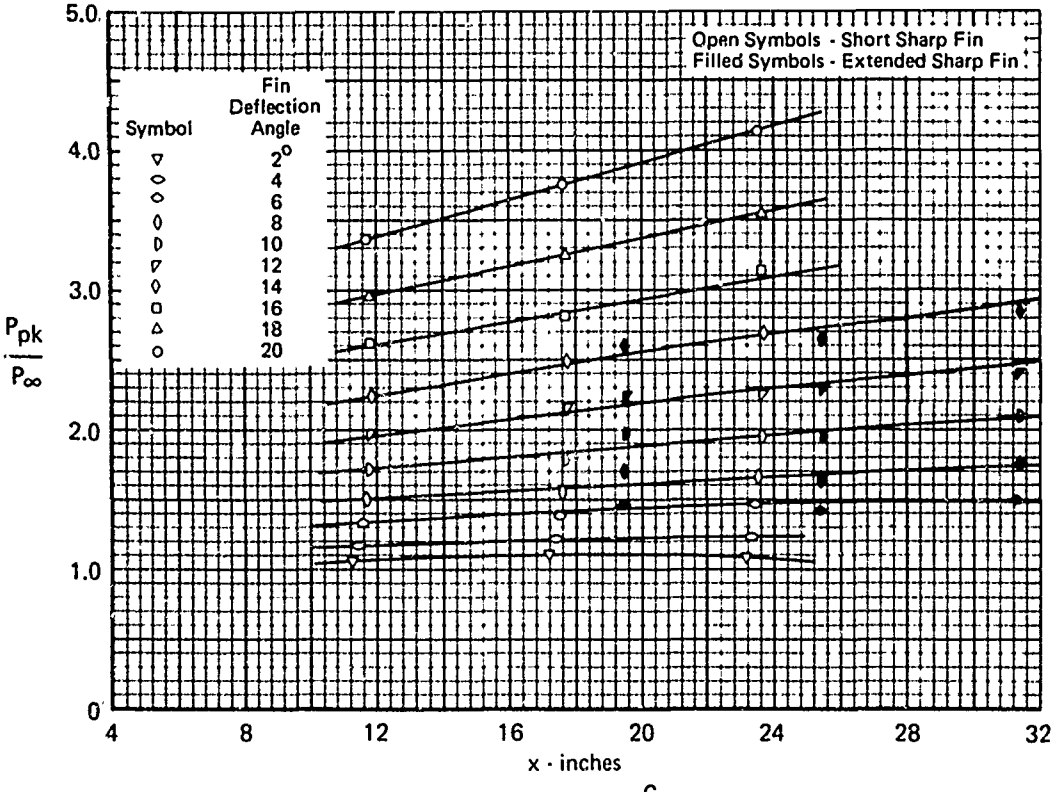

b. Re/Ft = 1.5×10^6

FIGURE 18 PEAK PRESSURE VARIATION WITH DISTANCE FROM FIN LEADING EDGE

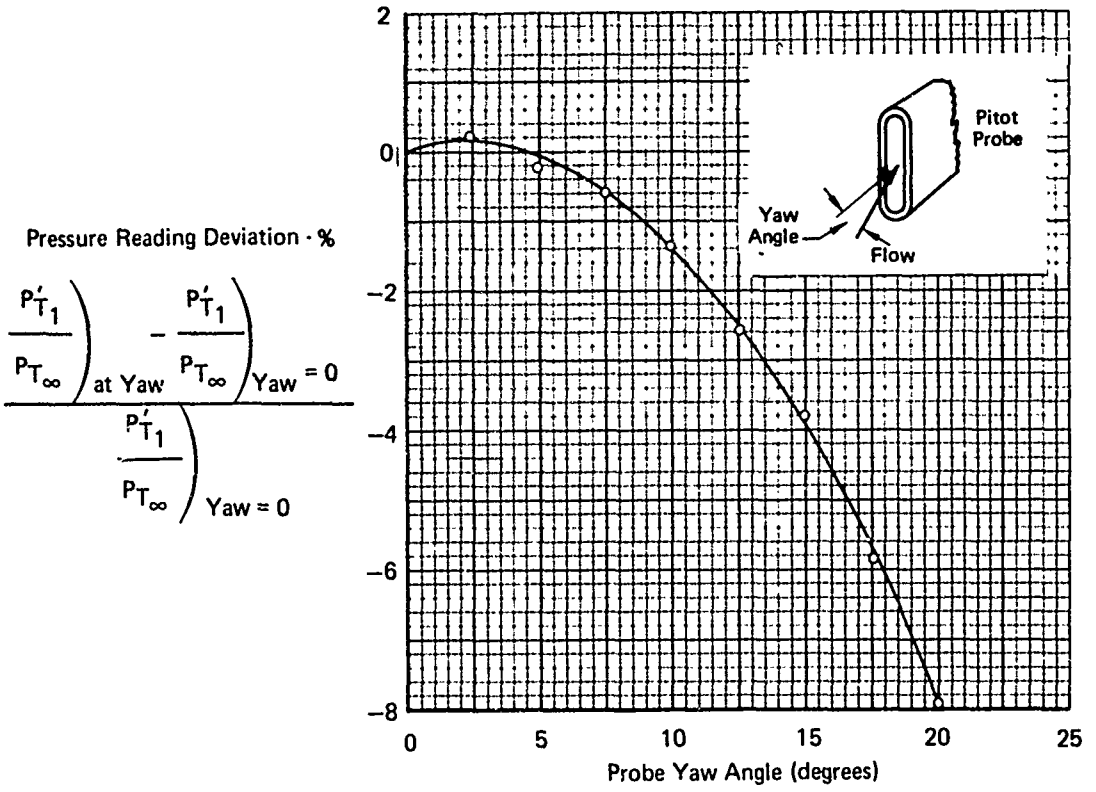

FIGURE 19 PITOT PROBE YAW SENSITIVITY

the same axial station as the fin pivot point, the probe remained essentially at a constant distance from the fin surface throughout the fin deflection angle range. The position of the rake did, however, vary relative to the impinging shock as the fin deflection angle was changed.

Selected machine plots of pitot pressure profiles in the interaction region for the bare sidewall and with the short sharp fin deployed at deflection angles from 4 through 20 degrees are illustrated in Figure 20. All 5 pitot pressure profiles are shown. The average bare plate pitot pressure profile is shown for cases when the fin was deployed. Figures 6 and 9 provide the probe spacing and position.

At distances sufficiently far removed from the test plate, the pitot pressure recovery in the interaction region is above bare test plate values. This increased pressure recovery is due to the increased efficiency of multiple shock compressions compared to a single normal shock which occurs when the pitot probes sense the freestream flow. Probe number 5 (far outboard) exhibits an even larger pitot pressure recovery relative to bare plate values. This higher recovery implies that the probe is sampling streamlines which have been compressed even more efficiently. Eventually the probe

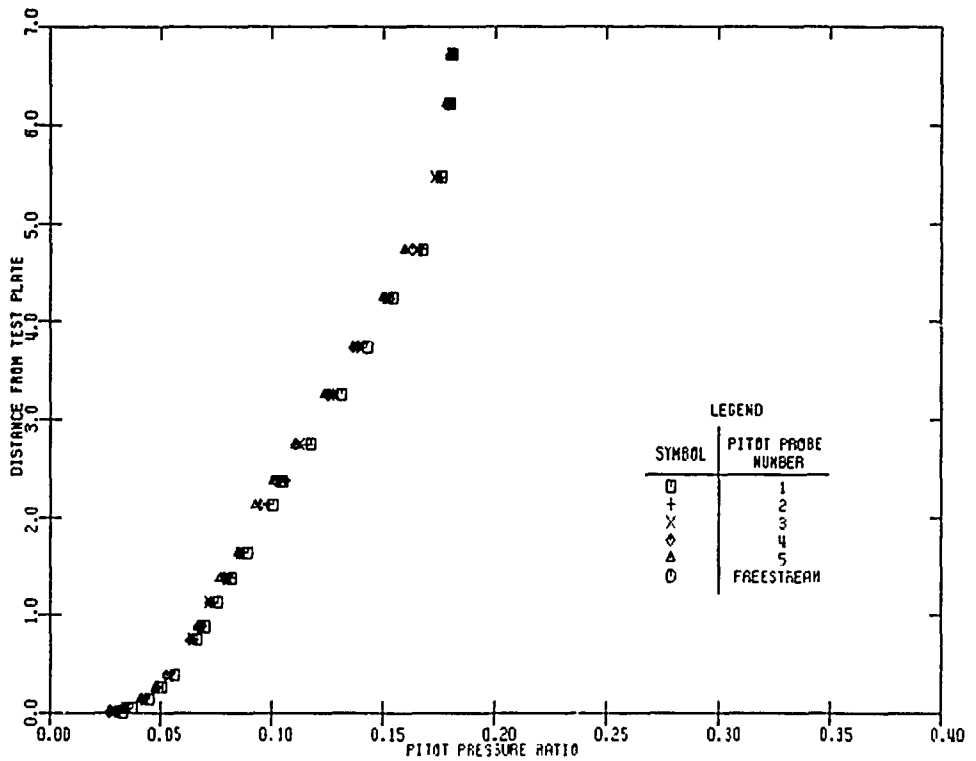

a. Bare Plate, Re/Ft = 3.5×10^6

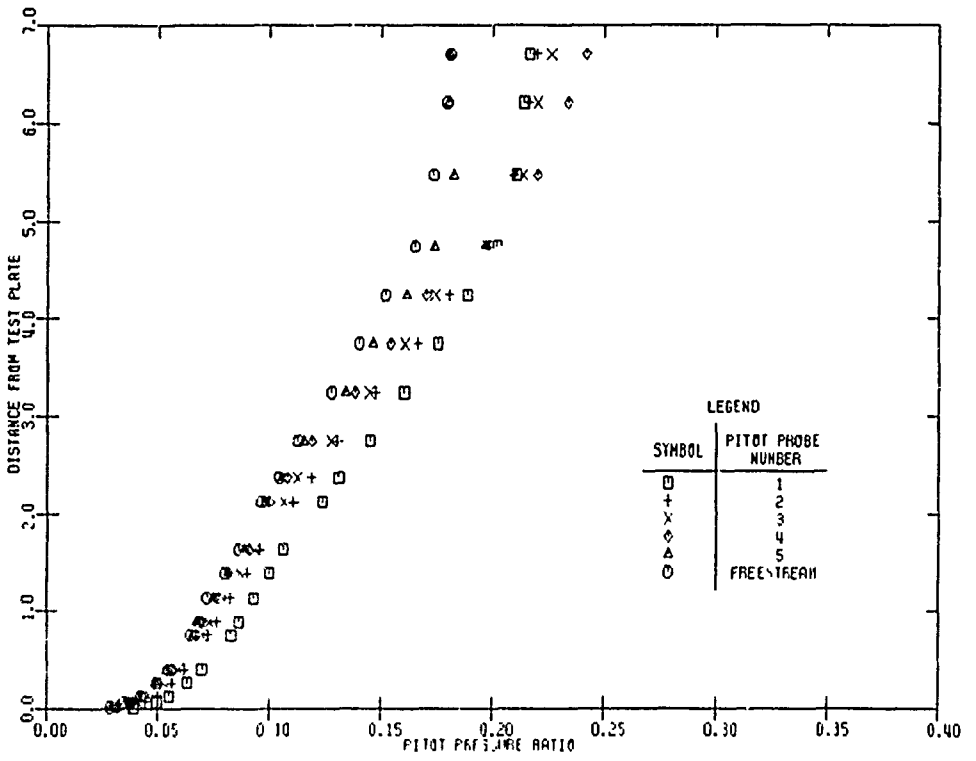

b. Short, Sharp Fin, $\alpha = 4^o$, Re/Ft = 3.6×10^6

FIGURE 20 SAMPLE PITOT PRESSURE MACHINE PLOTS

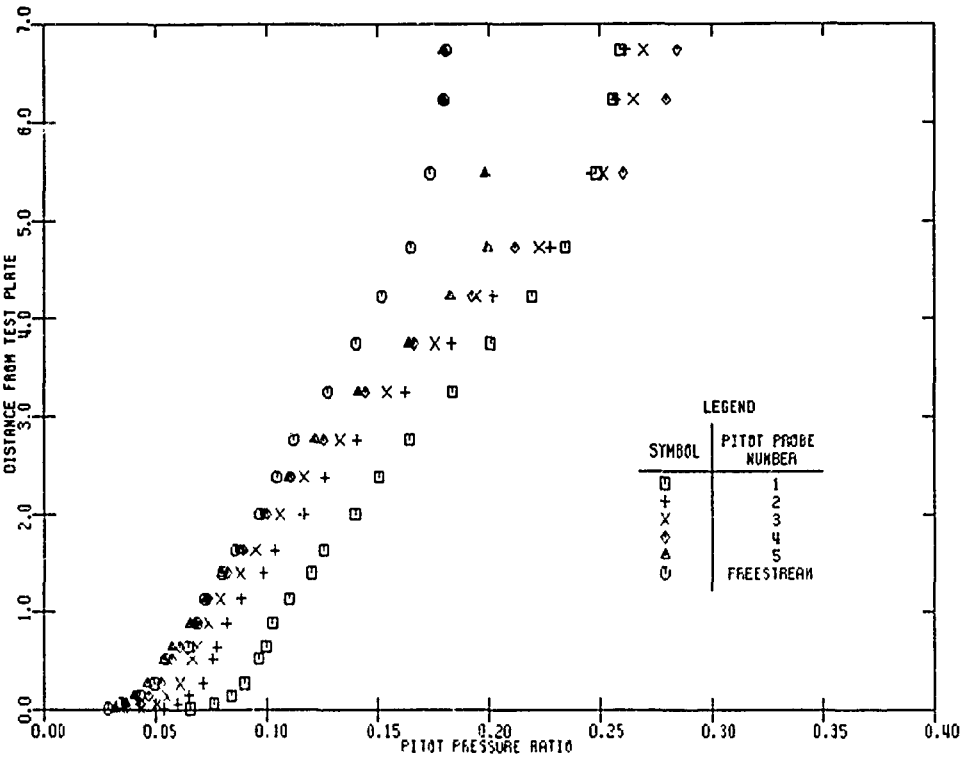

c. Short, Sharp Fin, $\alpha = 8^{o}$, Re/Ft = 3.5×10^{6}

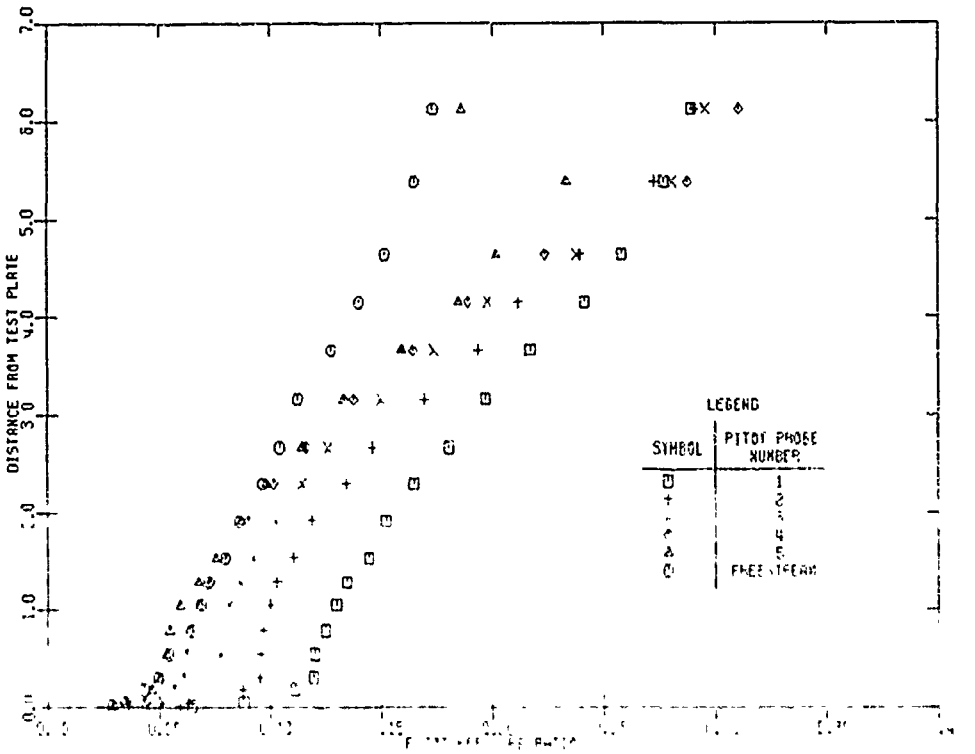

d. Short, Sharp Fin, $\alpha = 12^{o}$, Re/Ft = 3.5×10^{6}

FIGURE 20 SAMPLE PITOT PRESSURE MACHINE PLOTS (Continued)

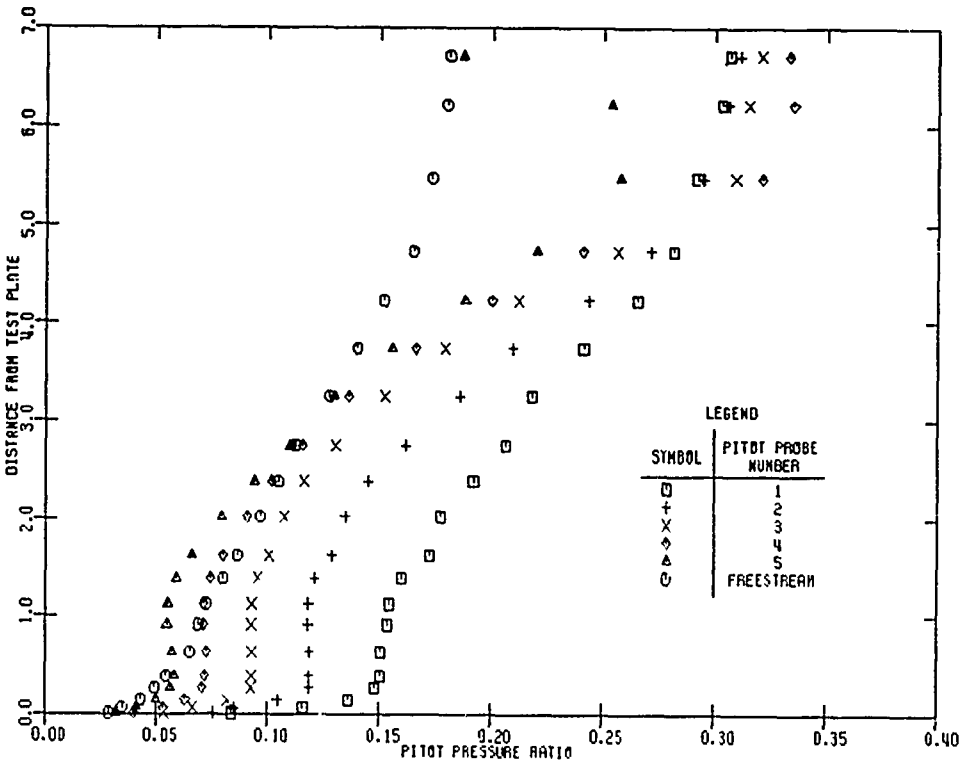

e. Short, Sharp Fin, $\alpha = 16^{o}$, Re/Ft = 3.5×10^{6}

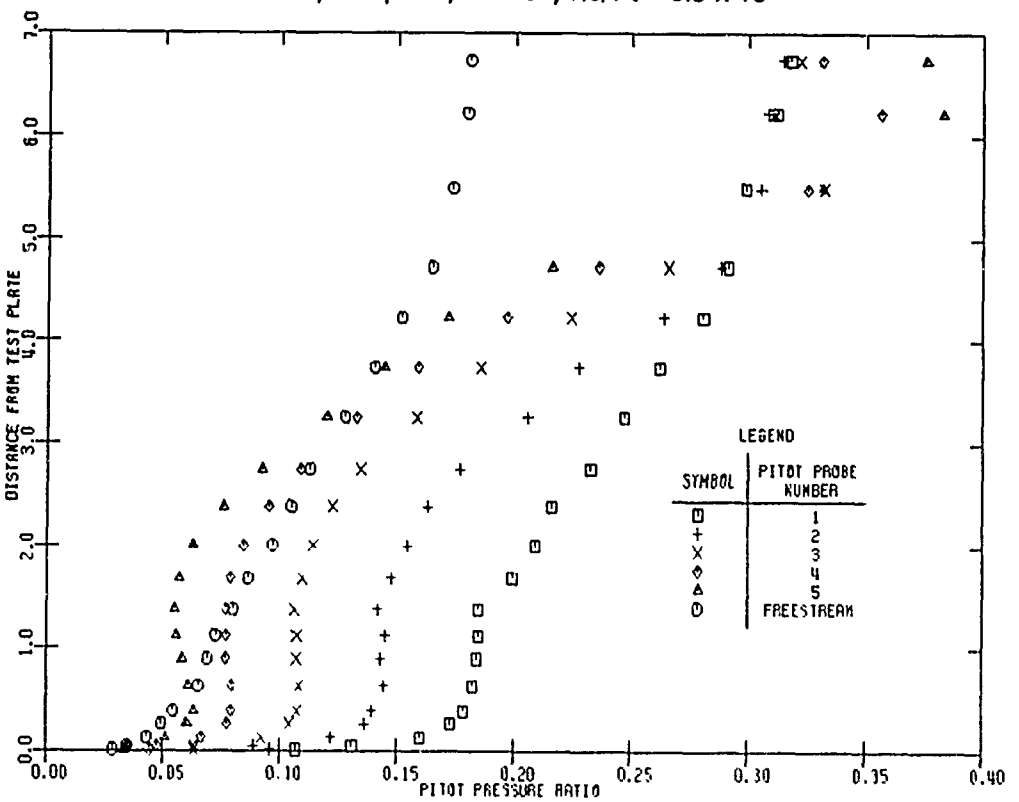

f. Short, Sharp Fin, $\alpha = 20^{o}$, Re/Ft = 3.5×10^{6}

FIGURE 20 SAMPLE PITOT PRESSURE MACHINE PLOTS (Concluded)

number 5 reading returns to the bare plate value for fin angles less than 20° which indicates that at a given distance above the test plate it senses freestream values for fin angles less than 20 degrees. The smaller probe numbers lie closest to the fin, hence, the surface shear decreases with distance outboard from the peak heating location as evidenced by the shape of the pitot pressure profile near the surface. Sufficiently far outboard the pitot profiles near the surface, for fin deflection angles of 12° and higher, exhibit a reversal which may indicate separation. Because of the qualitative character of the measurement, no definite conclusions could be reached.

2.2.4 Oil Flow Results - Surface oil flow tests were conducted at selected fin angles for both the sharp and blunt unswept fins. Figure 21 illustrates the oil flow pattern obtained for two sharp leading edge fin deflections. As illustrated in Figure 21a, the flow turns outboard at angles larger than the fin deflection angle when the fin is deflected at 4 degrees. The oil streaks indicate this is a gradual turning of the surface streamlines. By contrast, Figure 21b illustrates the oil flow pattern obtained with the sharp leading edge fin at a 20 degree deflection angle. The freestream surface oil streak lines terminate abruptly at an oil accumulation line. This feature is characteristic of three-dimensional separation based on Maskell's criterion, Reference 7. The oil accumulation line exhibits large curvature in the vicinity of the fin leading edge. However, the curvature appears to decrease with distance away from the leading edge. Immediately adjacent to the fin surface oil streak lines appear to progress downstream on paths parallel to the fin surface. Somewhat outboard of that region, the surface oil streak lines are swept outboard toward the impinging shock wave. They attain maximum deflections relative to the freestream direction and subsequently turn aft in the vicinity of the impinging shock wave. Outboard of the impinging shock location the oil streak lines are relatively straight and are deflected at a small angle relative to the oil accumulation line. Figure 22 illustrates the influence of fin deflection angle on the measured oil streak deflection angles at several characteristic locations on the tunnel sidewall between the fin and the oil accumulation line.

The surface oil pattern obtained with the blunt leading edge fin at a 16 degree deflection angle is illustrated in Figure 23. Except for the region in the immediate vicinity of the fin leading edge, the oil flow pattern is

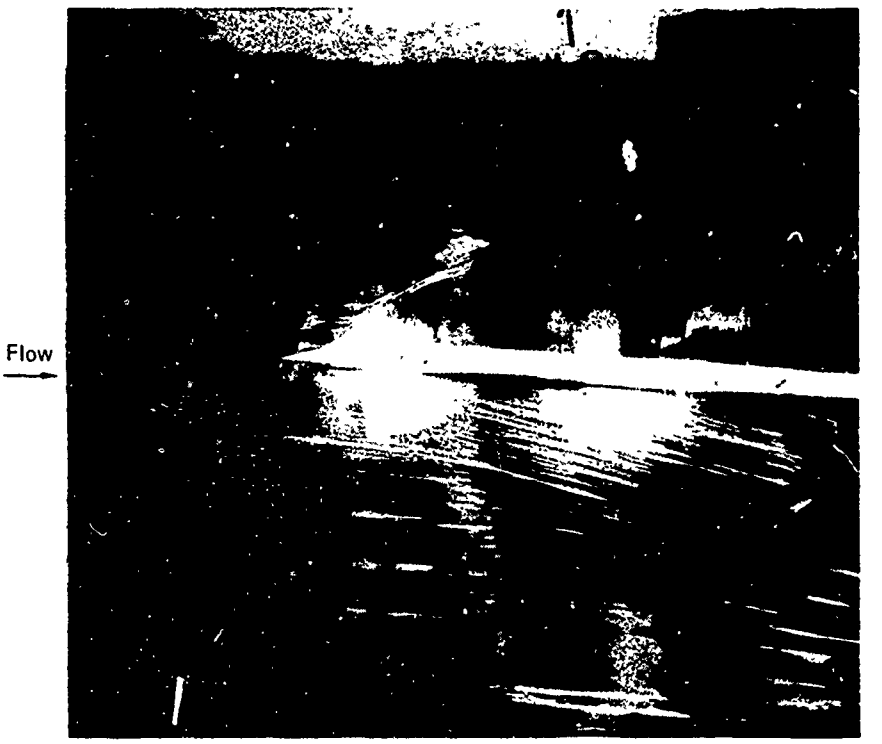

a. $\alpha = 4^{o}$

b. $\alpha = 20^{o}$

FIGURE 21 OIL FLOW PATTERN - SHARP FIN

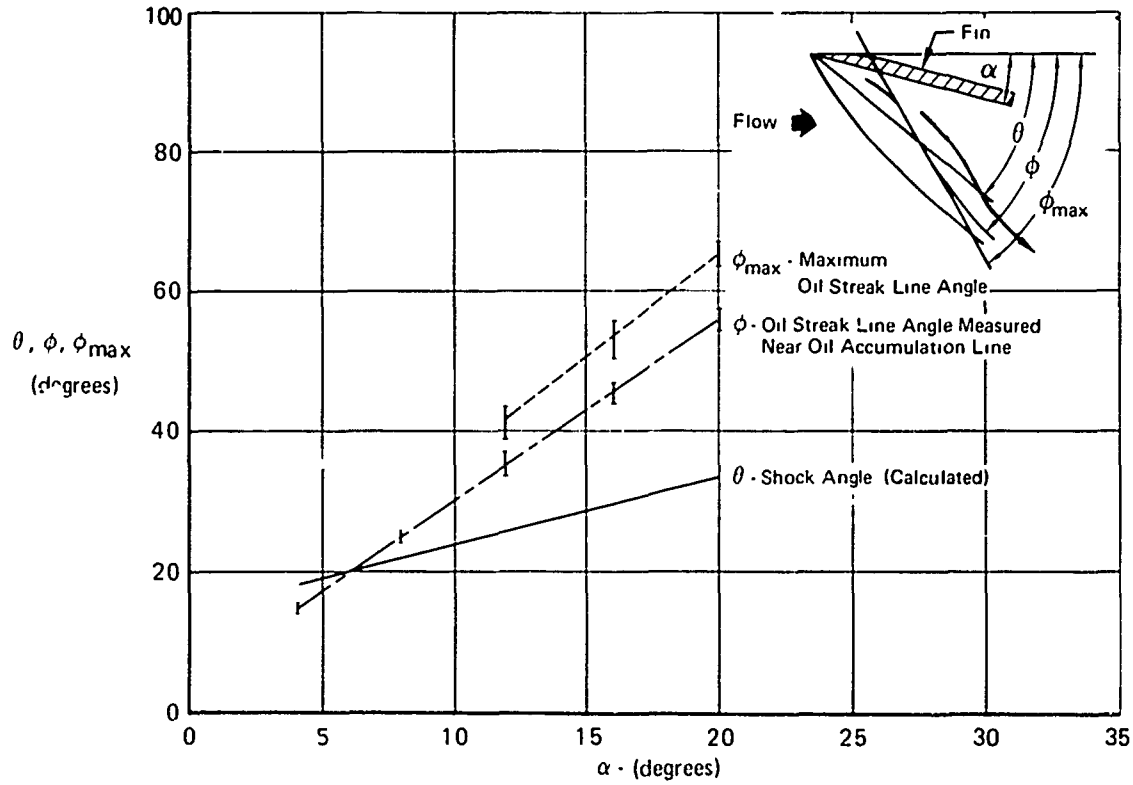

FIGURE 22 CHARACTERISTIC SURFACE OIL STREAK LINE DEFLECTION ANGLES

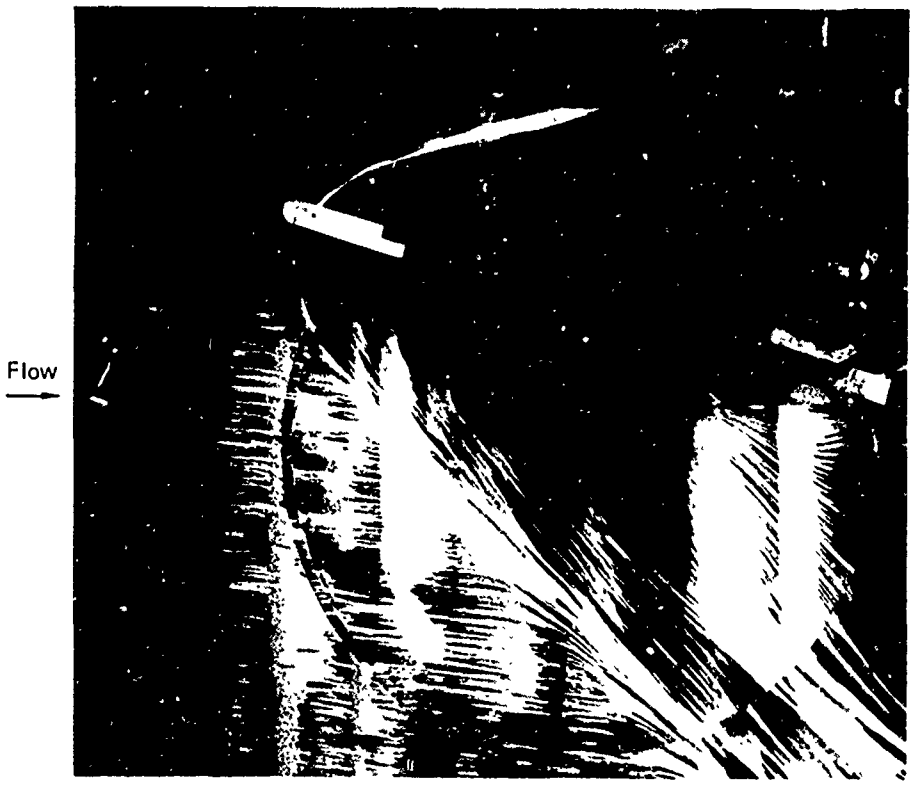

FIGURE 23 OIL FLOW PATTERN - BLUNT FIN - $\alpha = 16^{o}$

very similar to that observed for the sharp leading edge fin at large deflection angles. In the fin leading edge region the blunt fin oil flow pattern illustrates both separation and reattachment characteristic of blunt proturberances with detached bow shock waves such as those discussed in Reference 1.

2.2.5 Summary of Sharp Fin Results - A summary of sharp fin results is schematically shown in Figure 24. This overlay of interaction region characteristics is based upon data measured with the sharp fin deflected at a sufficiently large angle to cause separation. The shock wave location is calculated. The fin surface and the shock wave serve as reference lines in Figure 24. The separation line was identified outboard of the impinging shock by observed surface oil accumulation. The separation line is highly curved in the vicinity of the fin tip, however, the curvature appears to decrease rapidly with distance downstream.

A locus of peak heating was measured close to the fin surface and at a small angle relative to the fin surface. The magnitude of the peak heating continually increased along the peak heating locus to the most downstream instrumentation location. Based on the shape of the heating gradient along the locus, it is anticipated that the peak heating will increase for some distance downstream.

In the region between the peak heating line and the fin, the surface pressure increased to its maximum at the fin. The heating level decreased from its peak to a lower level at the fin and surface oil streak lines were essentially parallel to the fin. From a line slightly inboard of the peak heating line, surface oil streak lines turn abruptly outboard in a high shear region.

In the region between the peak heating line and the calculated shock, the surface heating and surface pressure decrease with outboard distance. The surface oil streak lines indicate a large outflow which begins to decrease in the vicinity of the shock.

In the region between the shock and the separation line, the surface pressure becomes essentially constant at a plateau level, while the surface heating continues to decrease. Both eventually decrease toward freestream levels in the vicinity of the separation line. In this region the oil streak lines asymptotically approach straight lines inclined at a small angle relative to the oil accumulation line. All data displayed consistency and

adequate accuracy for meaningful comparison and correlation with analytical techniques.

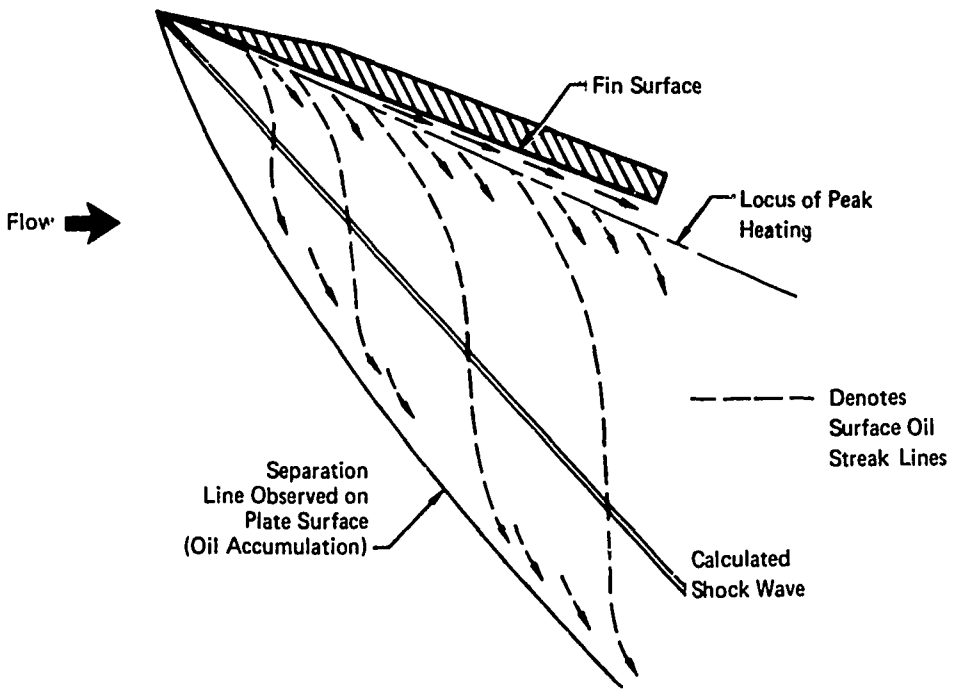

FIGURE 24 SKETCH OF OBSERVED SURFACE PHENOMENA

3. ANALYTICAL PROGRAM

The qualitative results of the experimental program, discussed in Section 2.2, indicate that three-dimensional shock wave boundary layer interaction flow fields and surface heating distributions are complex. The surface heating in such regions is intimately coupled to the flow field. The purpose of the analytical program is to develop a simplified, semi-empirical approach for quantitative definition of surface heating parameters.

The approach for obtaining these quantitative expressions is to evaluate the ramifications of two simplified models of the flow field as discussed in Section 3.1. A model of the interaction region which is based on the existance of a vortex is subsequently adopted. New analytical expressions based on the "vortex dominated flow model" are developed in Section 3.2 for defining the heat transfer distributions. Empirical parameters required to develop the technique are determined using a selected group of data. This data was chosen since it is thought to be most accurate.

Comparisons and correlations of sharp fin flow field data are presented in Section 3.3. The developed heating correlations and analytical techniques are compared to the sharp fin data in Section 3.3.

The heating correlations and analytical techniques are compared to blunt and blunt swept fin data in Section 3.4. In order to make comparisons with data for the more complex fin geometry, the analytical approach defined using sharp fin data is modified as required.

3.1 Flow Models

Simplified models of the interaction flow field are hypothesized and compared to the data base provided in Section 2. One model of the interaction flow structure, termed the "Effective New Boundary Layer Flow Model," is an extension of an available technique for defining the magnitude of peak heating. A new flow field hypothesis is suggested and termed the "Vortex Dominated Flow Model." It is then used to develop an analytical expression for calculating heating distributions in the flow interaction region.

3.1.1 Comparison of Flow Models with Results - Qualitative comparisons between observed flow field and heating data and the implications of each of the two interaction flow models are presented below.

3.1.1.1 Effective New Boundary Layer Flow Model - The Effective New Boundary Layer Flow Model is an extension of the effective new boundary layer

method for calculating peak heating magnitude in the interference flow region presented in Reference 3. The flow model is based on the hypothesis that the impinging shock wave destroys the existing boundary layer entering the interaction region. An effective new boundary layer is formed at the shock impingement location and its downstream development and state determines the heating variation. This simplified view of the flow structure is conceptually sketched in Figure 25.

The implications of this model can be compared to measured data trends. As indicated on Figure 25, the establishment of a new boundary layer introduces a new characteristic length. Regardless of the state of the new boundary layer, the new characteristic length downstream of the shock would imply that heating is constant along lines parallel to the shock wave. Figure 26 is a plot of the measured normalized heat transfer coefficient along an inviscid streamline. The data on Figure 26 show that, to very good approximation, the normalized heat transfer coefficient is constant along lines parallel to the shock wave. These data agree with the flow model.

The effective new boundary layer model also suggests that the peak heating line would be parallel to the impinging shock wave. This latter implication, which is directly related to the concept of a new characteristic length, is not validated by the data presented on Figure 26. The data, which are a composite of data points from the four instrumentation columns, indicate that the heating increases downstream and that the peak heating locus is not parallel to the shock wave. The local peak heating data points can be recognized as the most downstream data point for each instrumentation column. This applies to both the short and extended sharp leading edge fin data. The data indicates that the peak heating line is oriented at a more oblique angle with respect to the flow direction. This anomaly was apparently recognized in Reference 3 since the authors also introduced a correlation for the location of peak heating along a line which is more oblique relative to the free-stream direction than the shock line.

When the boundary layer entering the interaction region is turbulent, Reference 3 suggests that the effective new boundary layer downstream of the impinging shock wave will also be turbulent. Thus, the theoretical peak heating value must decrease along its locus downstream. This type of heating variation was not experimentally observed. The data presented in Figure 26

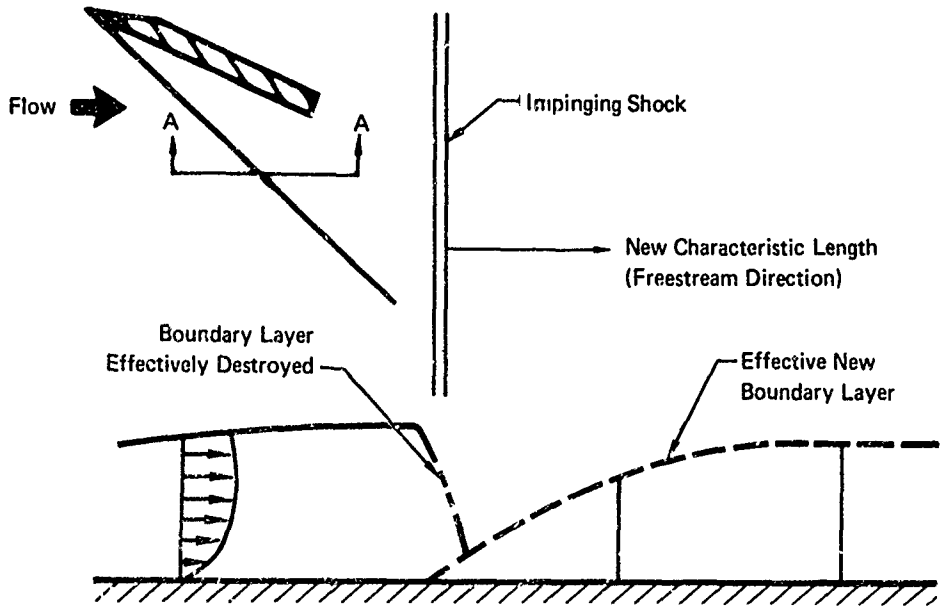

FIGURE 25 EFFECTIVE NEW BOUNDARY LAYER FLOW MODEL

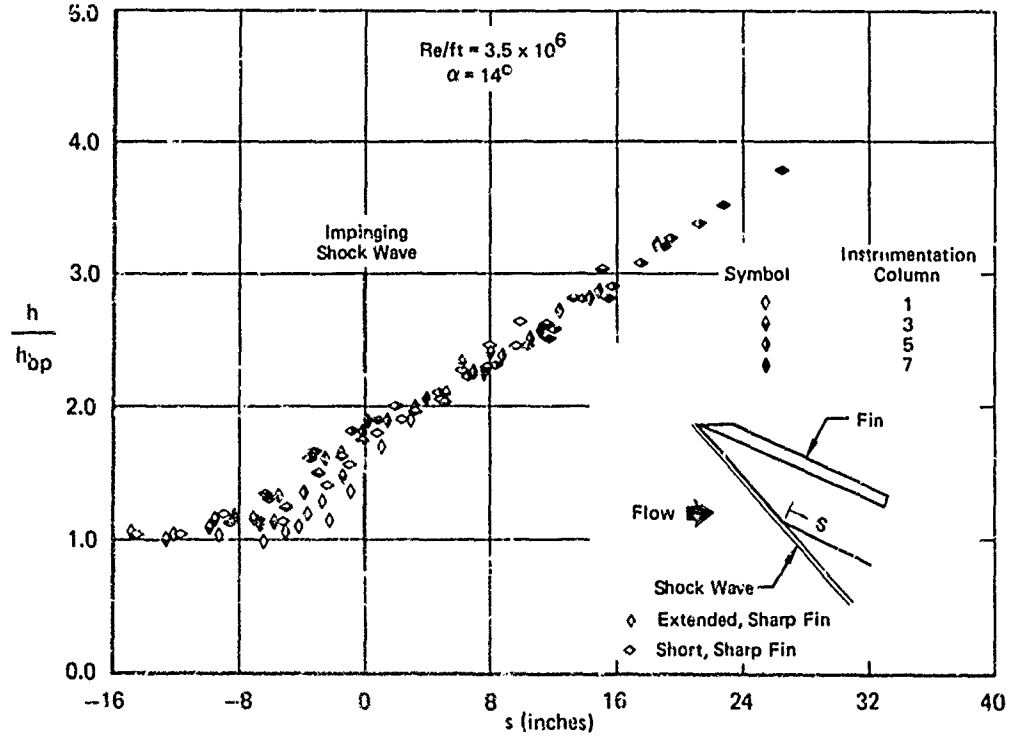

FIGURE 26 HEATING DISTRIBUTION ALONG AN INVISCID STREAMLINE

indicates that the peak heating magnitude increases with downstream distance.

Finally, the effective new boundary layer model does not distinguish between separated and unseparated boundary layer cases. Since separation has been experimentally observed for sufficiently strong interactions, the model is not physically realistic.

3.1.1.2 Vortex Dominated Flow Model - The Vortex Dominated Flow Model is based on a new concept of the interference flow structure formulated from the data trends discussed in Section 2. As noted in Section 2, the available data are not adequate to completely specify the interference flow structure.

The hypothesized interaction flow structure is dominated by a spiralling vortex which is caused by three-dimensional separation at sufficiently large fin deflection angles. The region most probably contains more than one vortex. However, for conceptual simplicity one large vortex is hypothesized as illustrated in Figure 27. This vortex entrains higher energy air as it grows with downstream distance. The entrained air is visualized as impinging on the plate surface in close proximity to the fin and subsequently flowing out away from the fin in response to both the pressure gradient induced by the impingement of the entrained flow and the momentum exchange with the cross flow component of the vortex. In the cross flow plane an imbedded turbulent boundary layer with its origin at the induced flow impingement location is initiated. It is envisioned as determining the heating distribution normal to the inviscid streamlines.

Qualitatively this flow model requires that both peak heating and peak pressure must increase with downstream distance due to flow entrainment. This variation is validated by data in Figures 26 and 28. According to the model, the peak heating and peak pressure will increase to a maximum value some point downstream where the vortex is entraining maximum energy flow. Maximum energy flow consists of those streamlines which have not directly experienced viscous effects caused by the surface boundary layers. In this sense, the interaction would scale with the boundary layer thickness of the flow entering the interaction region.

The main thrust of the vortex dominated interaction region hypothesis is that the cross flow component of the imbedded boundary layer will determine the heating distribution in the cross flow plane, and that the vortex growth and entrainment rates will define the peak heating increases with distance aft.

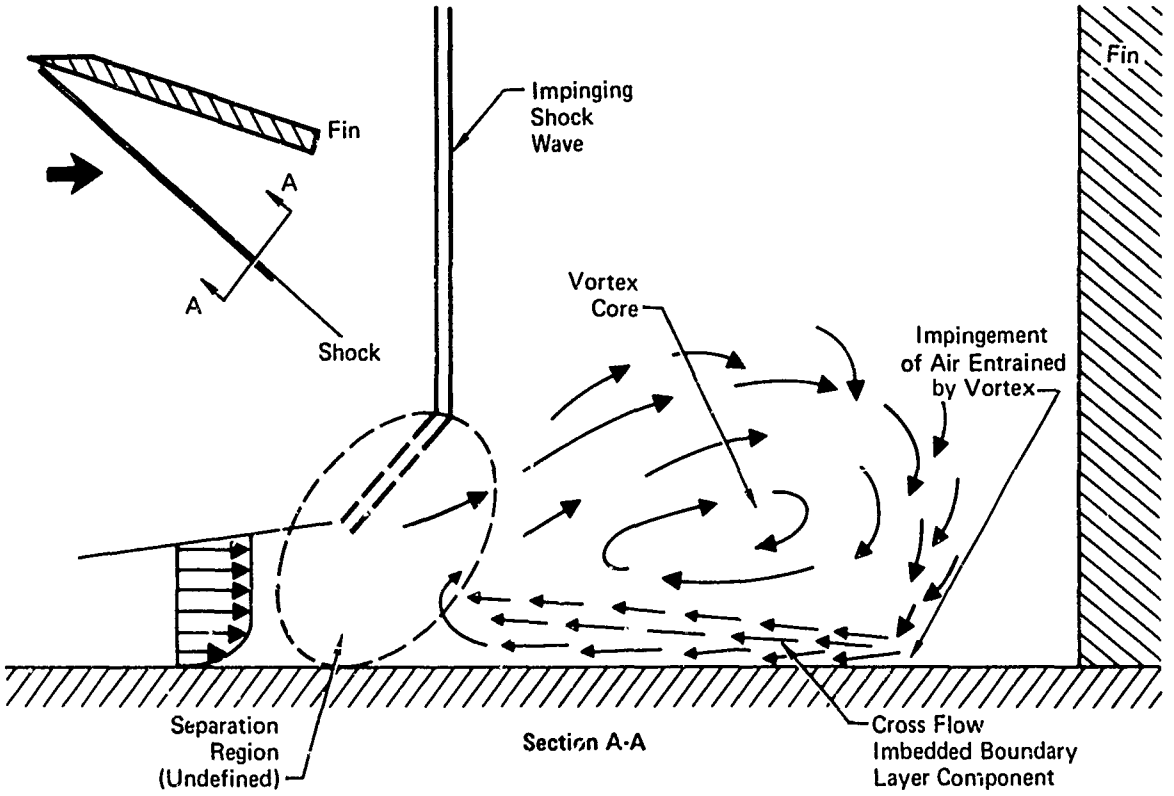

FIGURE 27 VORTEX DOMINATED FLOW MODEL

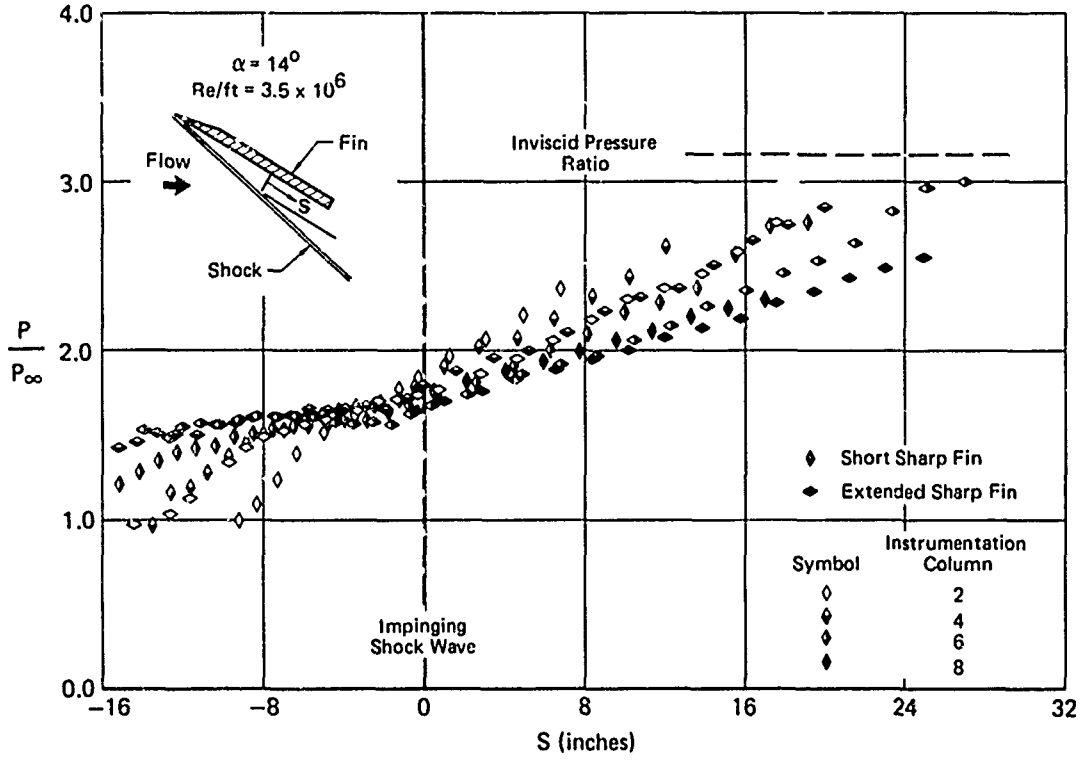

FIGURE 28 PRESSURE DISTRIBUTION ALONG AN INVISCID STREAMLINE

Since the vortex also grows in width as well as height, it is expected that the heating distributions will be invariant with downstream distance. In the separated flow region this model will predict a heating rate which is a constant multiple of the bare plate value invariant with downstream distance. This is in accord with two-dimensional separated flow heating. The invariance is illustrated on Figure 26 where it is shown that, independent of instrumentation streamwise location, the heating under the impinging shock wave location is constant for a given fin deflection angle.

3.1.2 Selection of Vortex Dominated Flow Model - The vortex dominated flow model is selected for development and data correlation based on the superior qualitative agreement with data trends it exhibits. The region of applicability of the Vortex Dominated Model lies between the impinging shock and the line of peak heating which is in close proximity to the fin-plate interface. Furthermore, the model is only expected to be applicable in interactions of sufficient strength to cause separation which develops the vortical motion.

3.2 Heat Transfer Analysis Technique

An analytical expression for the heat transfer distribution in the flow interaction region can be developed by suitable approximation of the imbedded cross flow component of the boundary layer under the vortex. Figure 29 is a sketch of the interaction region. In order to develop the analytical heat transfer distribution between the impinging shock and the peak heating line, the location of these two boundaries must be determined. The shock location is calculated by inviscid gas dynamic equations. The location of peak heating is specified by data correlation. The heating magnitudes at the two boundaries are also required. Both of these values are specified by data correlation. With the location and heating magnitudes known at the shock impingement line and on the peak heating line, the analytical technique to calculate heating distributions are developed using analytical approximations to the Vortex Dominated Flow Model.

3.2.1 Derivation of Governing Equation - The adopted physical view of the interaction flow is that an imbedded vortex is brought on by three-dimensional separation, and that this vortex will entrain flow and give rise to a cross flow component along the surface. Viscous effects will cause velocity gradients normal and parallel to the surface. Thus by approximation the region

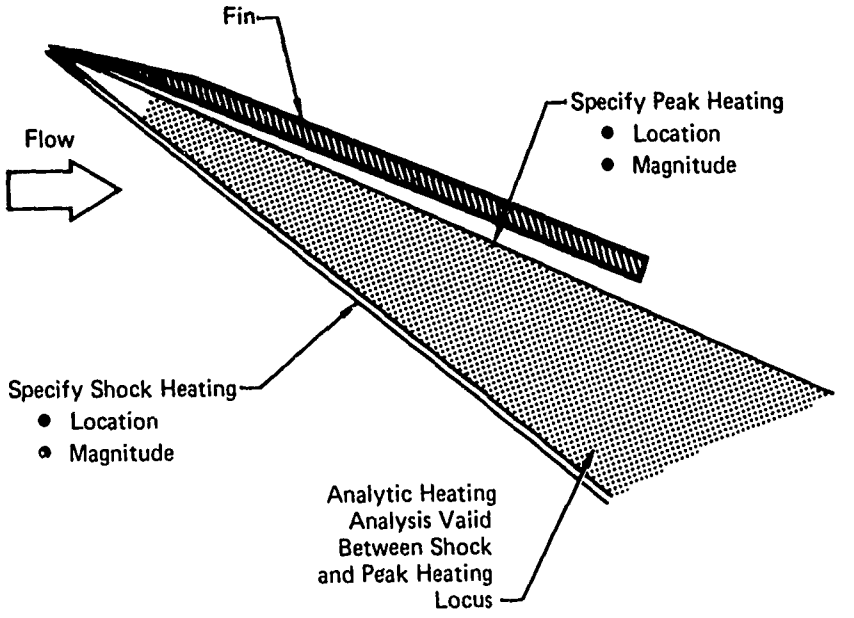

FIGURE 29
BOUNDARY CONDITIONS FOR HEATING DISTRIBUTION ANALYSIS

is treated as a turbulent boundary layer developing in a region of velocity and pressure gradient. One simple expression for the heat transfer rate in such a region is the general form introduced by Van Driest in Reference 8, for heating in the vicinity of a turbulent stagnation point:

$$q = f_3 \beta^{4/5} \rho_e^{4/5} \bar{\psi}^{3/5} C_p \mu_e^{1/5} (T_{aw} - T_w). \quad (2)$$

Thus the heat transfer coefficient is:

$$h = f_3 \beta^{4/5} \rho_e^{4/5} \bar{\psi}^{3/5} C_p \mu_e^{1/5}. \quad (3)$$

where f_3 equals a constant multiplied by a function of $Pr^{2/3}$, $\beta(\bar{\psi})$ is the velocity gradient, and $\bar{\psi}$ is the distance measured away from the stagnation point. In order to apply this to the interaction problem, the entrained flow impingement point is considered as Van Driest's stagnation point, where $\bar{\psi}$ is measured normal to the inviscid streamlines (cross flow plane) from the peak heating line toward the shock impingment point as defined in Figure 30. ρ_e, C_p, μ_e, nd h are defined in the nomenclature.

The derivation proceeds by expressing all heat transfer coefficients in normalized form in order to develop an expression independent of distance downstream of the fin tip.

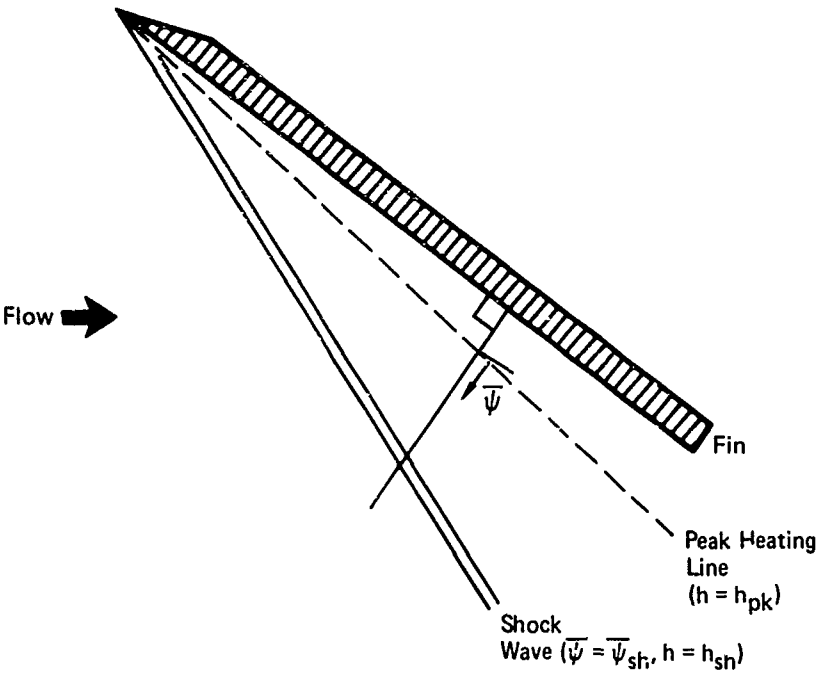

FIGURE 30 - DEFINITION OF $\overline{\psi}$

As discussed in Section 2.2.6, the peak heating magnitude increases with distance from the fin tip as does the distance between the peak heating line and the shock wave. The heat transfer coefficient at the shock remains constant for the sharp fin data at a given fin angle and flow conditions. In order to establish a relationship that is valid at any downstream station, the heating expression is written in normalized form as:

$$\frac{h - h_{sh}}{h_{pk} - h_{sh}}; \text{ where: } \begin{array}{l} h_{sh} = \text{value of h @ the shock} \\ h_{pk} = \text{value of h @ the peak heating line} \end{array} \quad (4)$$

Note that this normalized heat transfer coefficient parameter is restricted to values between 0 and 1,

$$\underbrace{0 \leq}_{\text{@ the shock}} \underbrace{\frac{h - h_{sh}}{h_{pk} - h_{sh}} < 1}_{\text{at the peak heating line}} \quad \bullet$$

By substitution of Equation (3) into Equation (4)

$$\frac{h - h_{sh}}{h_{pk} - h_{sh}} = \frac{f_3\, \beta^{4/5}\, \rho_e^{4/5}\, (\bar{\psi})^{3/5}\, C_p\, \mu_e^{1/5} - f_{3_{sh}}\, \beta_{sh}^{4/5}\, \rho_{sh}^{4/5}\, (\bar{\psi})_{sh}^{3/5}\, C_{p_{sh}}\, \mu_{sh}^{1/5}}{f_{3_{pk}}\, \beta_{pk}^{4/5}\, \rho_{pk}^{1/5}\, (\bar{\psi})_{pk}^{3/5}\, C_{p_{pk}}\, \mu_{pk}^{1/5} - f_{3_{sh}}\, \beta_{sh}^{4/5}\, \rho_{sh}^{4/5}\, (\bar{\psi})_{sh}^{3/5}\, C_{p_{sh}}\, \mu_{sh}^{1/5}}. \tag{5}$$

For simplicity the thermophysical properties are assumed constant, thus,

$$C_p \simeq C_{p_{sh}} \simeq C_{p_{pk}},$$

$$\mu_e \simeq \mu_{sh} \simeq \mu_{pk}, \tag{6}$$

$$f_3 \simeq f_{3_{sh}} \simeq f_{3_{pk}}.$$

Substituting Equation (6) into Equation (5) and normalizing by the factor $\beta_{sh}^{4/5}\, \rho_{sh}^{4/5}\, (\bar{\psi})_{sh}^{3/5}$

$$\frac{h - h_{sh}}{h_{pk} - h_{sh}} = \frac{\left(\frac{\beta_e}{\beta_{sh}}\right)^{4/5} \left(\frac{\rho_e}{\rho_{sh}}\right)^{4/5} \left(\frac{\bar{\psi}}{\bar{\psi}_{sh}}\right)^{3/5} - 1}{\left(\frac{\beta_{pk}}{\beta_{sh}}\right)^{4/5} \left(\frac{\rho_{pk}}{\rho_{sh}}\right)^{4/5} \left(\frac{\bar{\psi}_{pk}}{\bar{\psi}_{sh}}\right)^{3/5} - 1}. \tag{7}$$

If the edge of the imbedded boundary layer is assumed isothermal:

$$\frac{\rho_e}{\rho_{sh}} \simeq \frac{P_e}{P_{sh}} \tag{8}$$

By assuming the pressure gradient is linear between the shock wave and the peak heating line, the density ratio can be written as

$$\frac{\rho_e}{\rho_{sh}} = \frac{P_e}{P_{sh}} = 1 + C\left(1 - \frac{\bar{\psi}}{\bar{\psi}_{sh}}\right), \tag{9}$$

where C is the pressure parameter defined as:

$$C = \frac{P_{pk} - P_{sh}}{P_{sh}}.$$

Therefore:

$$\frac{h - h_{sh}}{h_{pk} - h_{sh}} = \frac{\left(\frac{\beta}{\beta_{sh}}\right)^{4/5}\left[1 + C\left(1 - \frac{\bar{\psi}}{\bar{\psi}_{sh}}\right)\right]^{4/5}\left(\frac{\bar{\psi}}{\bar{\psi}_{sh}}\right)^{3/5} - 1}{\left(\frac{\beta_{pk}}{\beta_{sh}}\right)^{4/5}\left[1 + C\left(1 - \frac{\bar{\psi}_{pk}}{\bar{\psi}_{sh}}\right)\right]^{4/5}\left(\frac{\bar{\psi}_{pk}}{\bar{\psi}_{sh}}\right)^{3/5} - 1}. \tag{10}$$

In order to reduce Equation (10) further, the variation of β must be specified. Let β be expressed as $\beta = b(\bar{\psi})^n$; b = constant. This assumption which diverges from the stagnation point solution of Van Driest is that the velocity gradient is not constant, but rather varies with $\bar{\psi}$. In order to derive Equation (10), β was assumed constant. The assumption that β is a function of $\bar{\psi}$ in Equation (10) is an assumption of local similarity. With the assumed form for β,

$$\frac{\beta}{\beta_{sh}} = \left(\frac{\bar{\psi}}{\bar{\psi}_{sh}}\right)^n ; \frac{\beta_{pk}}{\beta_{sh}} = \left(\frac{\bar{\psi}_{pk}}{\bar{\psi}_{sh}}\right)^n . \tag{11}$$

Then by substitution

$$\frac{h - h_{sh}}{h_{pk} - h_{sh}} = \frac{\left(\frac{\bar{\psi}}{\bar{\psi}_{sh}}\right)^{\frac{1}{5}(4n+3)}\left[1 + C\left(1 - \frac{\bar{\psi}}{\bar{\psi}_{sh}}\right)\right]^{4/5} - 1}{\left(\frac{\bar{\psi}_{pk}}{\bar{\psi}_{sh}}\right)^{\frac{1}{5}(4n+3)}\left[1 + C\left(1 - \frac{\bar{\psi}_{pk}}{\bar{\psi}_{sh}}\right)\right]^{4/5} - 1}. \tag{12}$$

Note that the term $(\bar{\psi}_{pk}/\bar{\psi}_{sh})^{\frac{1}{5}(4n+3)}$ is identically zero if $n \neq -3/4$, since $\bar{\psi}_{pk}$ is zero. Assuming that n is greater than minus 3/4, then Equation (12) becomes:

$$\frac{h - h_{sh}}{h_{pk} - h_{sh}} = 1 - \left(\frac{\bar{\psi}}{\bar{\psi}_{sh}}\right)^{\frac{1}{5}(4n+3)}\left[1 + C\left(1 - \frac{\bar{\psi}}{\bar{\psi}_{sh}}\right)\right]^{4/5}. \tag{13}$$

Note that:

$$\lim_{\bar{\psi} \to \bar{\psi}_{pk}} \left(\frac{h - h_{sh}}{h_{pk} - h_{sh}}\right) = 1, \text{ implying } \lim_{\bar{\psi} \to \bar{\psi}_{pk}} (h) = h_{pk},$$

$$\lim_{\bar{\psi} \to \bar{\psi}_{sh}} \left(\frac{h - h_{sh}}{h_{pk} - h_{sh}}\right) = 0, \text{ implying } \lim_{\bar{\psi} \to \bar{\psi}_{pk}} (h) = h_{sh}.$$

For convenience the coordinate system is changed such that

$$\psi = \bar{\psi}_{sh} - \bar{\psi}, \text{ where } |\psi_{pk}| = |\bar{\psi}_{sh}|. \tag{14}$$

By substituting Equation (14) into Equation (13)

$$\frac{h - h_{sh}}{h_{pk} - h_{sh}} = 1 - \left(1 - \frac{\psi}{(\psi_{pk})}\right)^{\frac{1}{5}(4n+3)} \left[1 + C \frac{\psi}{\psi_{pk}}\right]^{4/5}. \tag{15}$$

Equation (15) is the expression for the heating distribution between the peak heating line and the impinging shock wave. Numerical values for the exponential term (n) and the pressure parameter (C) are to be specified by empiricism. Terms in the normalized location (ψ/ψ_{pk}) and normalized heat transfer coefficient parameter $\left[(h - h_{sh}/h_{pk} - h_{sh})\right]$ are illustrated in Figure 31.

Numerical values for the exponential term (n) and the pressure parameter (C) in Equation (15) can be determined empirically by comparison with data. Prior to determining these values it is of interest to determine the influence of each on the heating distribution, Equation (15). Figure 32 is a plot of Equation (15) for the three indicated values of velocity gradient, which is exponentially dependent on (n), for a constant value of C. As indicated, the value of n has a large effect on the shape of the heating distribution. The 45^{o} line is shown for reference. Figure 33 illustrates the influence of the value of C at a constant value of n. As illustrated, the value of the normalized pressure increase between the shock and the peak heating line (C) does not greatly influence the shape of the distribution. Consistent with the

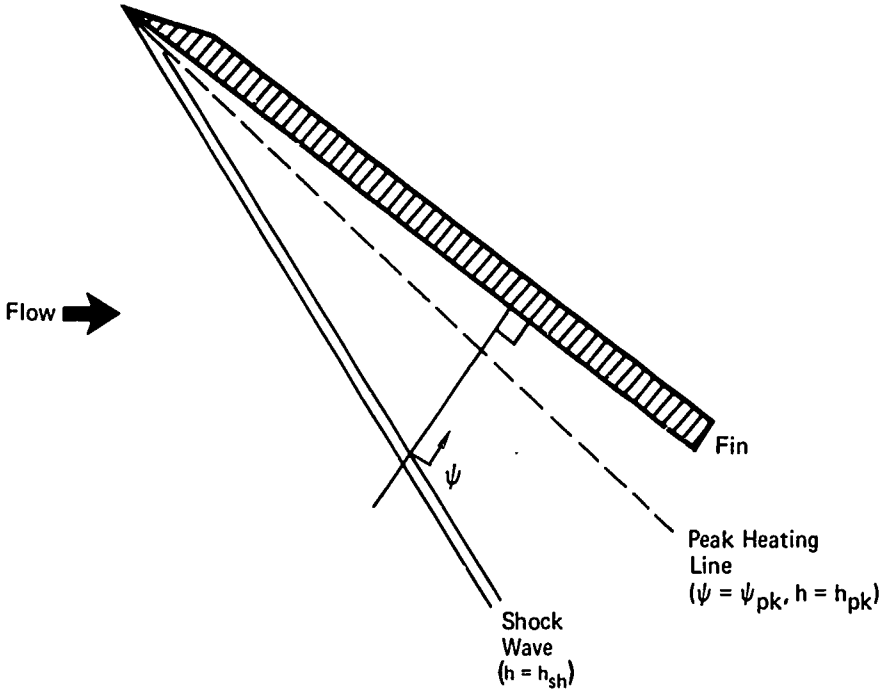

FIGURE 31 DEFINITION OF ψ

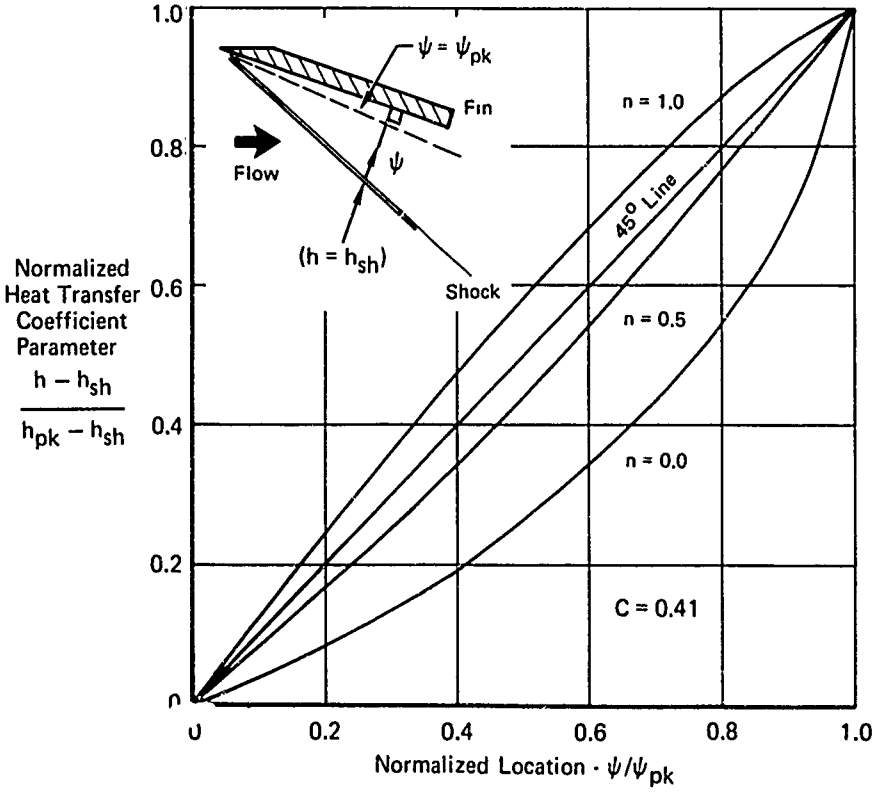

FIGURE 32 INFLUENCE OF VELOCITY GRADIENT PARAMETER (n) ON HEATING DISTRIBUTION

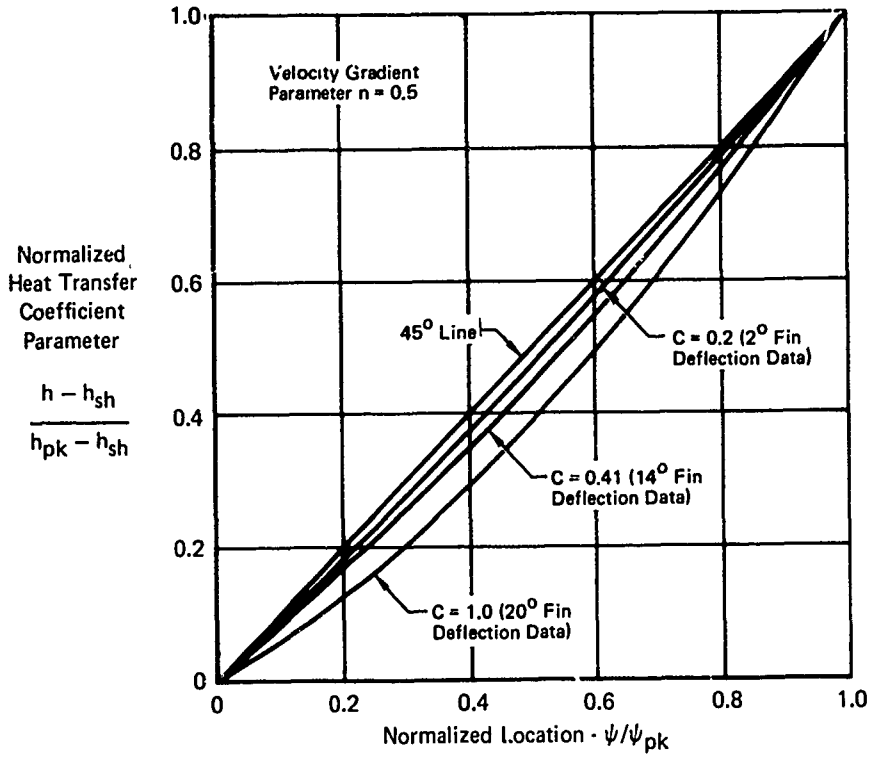

FIGURE 33 INFLUENCE OF PRESSURE PARAMETER (C) ON HEATING DISTRIBUTION

approximations made in the development of Equation (15), C is assumed to be a constant. This assumption reduces the variables which must be determined to values for n and the boundary conditions.

The influence on the velocity and its derivatives for n = 0.5 is illustrated in Figure 34. For comparison, the value of (β) corresponding to n = 0 (Hiemenz flow) is shown. The exponential dependence for β, ($\beta \propto \psi^{1/2}$) is equivalent to the assumption that a large velocity gradient variation occurs in the cross flow direction beginning at the flow impingement point. The corresponding velocity distributions are also shown and support conclusions made regarding the velocity gradient.

3.2.2 Empirical Parameters and Boundary Conditions - The empirical parameters n and C, plus the magnitudes and locations of h_{sh} and h_{pk}, must be specified in order to compare Equation (15) with measured data. These parameters and boundary conditions are evaluated in this section by using selected sharp fin test data.

3.2.2.1 Peak Heating Location - Two peak heating location correlations were obtained. Both correlations are presented in this section. One of these correlations which can account for interaction strength is suggested since it is thought to be more general.

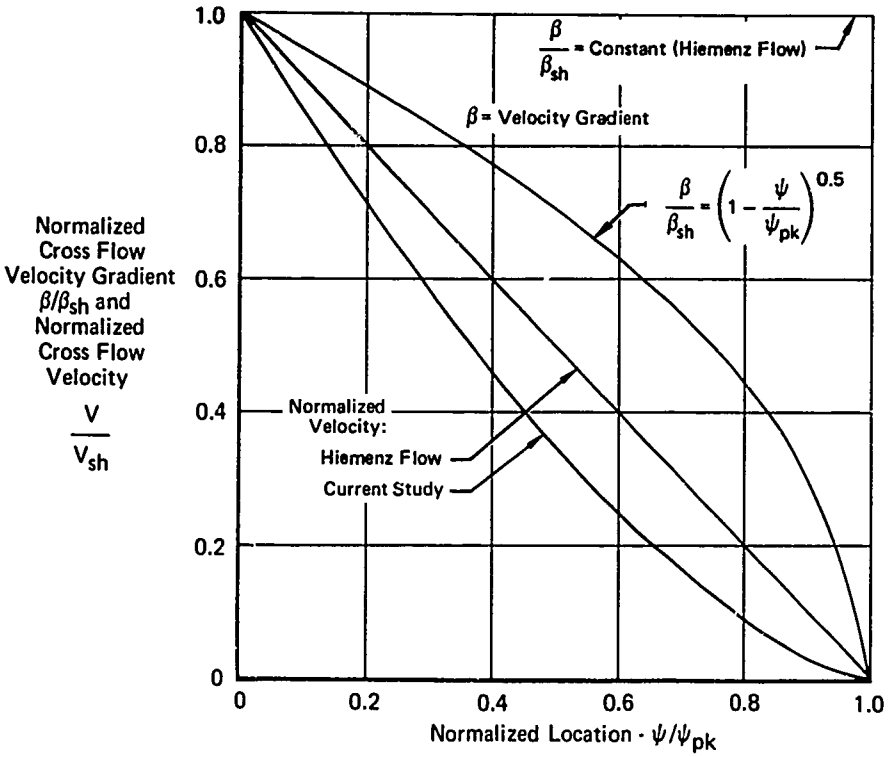

FIGURE 34 CROSS FLOW VELOCITY VARIATION IN INTERACTION REGION; n = 0.5

The sharp fin peak heating data were observed to lie along straight lines within the resolution determined by thermocouple spacing. These lines of peak heating were observed to be close to the fin surface as depicted in Figure 29 and discussed in Section 2.2. It was determined that the orientation of the peak heating line was best fitted by a line oriented at an angle relative to the freestream direction equal to the fin deflection angle plus 2-1/4 degrees. This line, when extended to the free streamline which intersects the fin leading edge, was found to intersect the leading edge streamline approximately 1.5 inches upstream of the leading edge. Figure 35 illustrates the correlation between this highly empirical method and measured data. Although the correlation is adequate, the extensive empiricism does not allow for variation with physical parameters such as Mach number.

In order to retain physical parameters in the peak heating location correlation, the orientation of the peak heating line was chosen somewhat differently. Figure 36 illustrates this second correlation which is represented by a straight line through the data and which intersects the fin leading edge. Over the range of fin deflections tested, it was determined that the included angle between the fin deflection angle and the shock angle for any given Mach

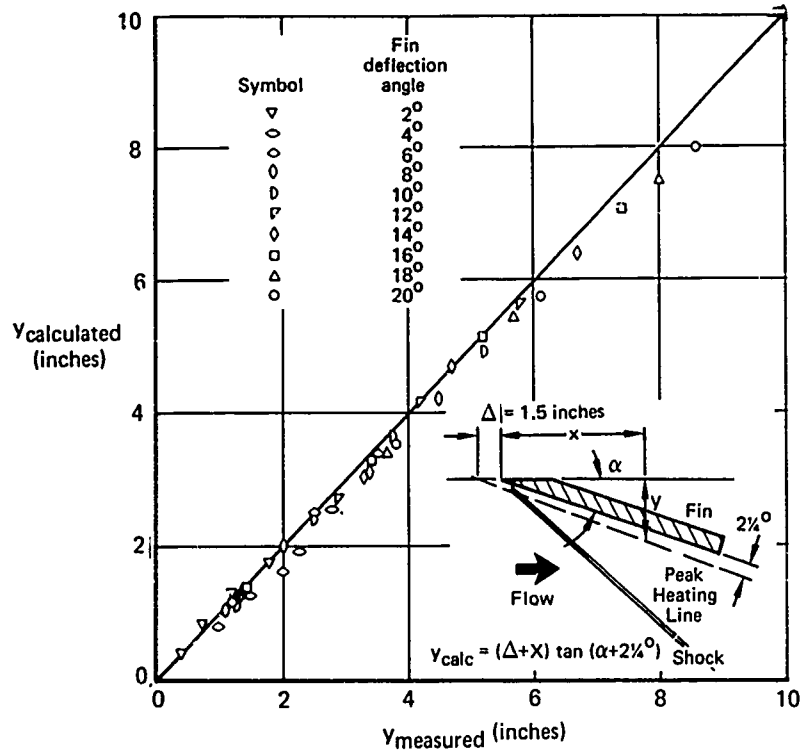

FIGURE 35 COMPARISON OF SHARP FIN PEAK HEATING LOCATION CORRELATION

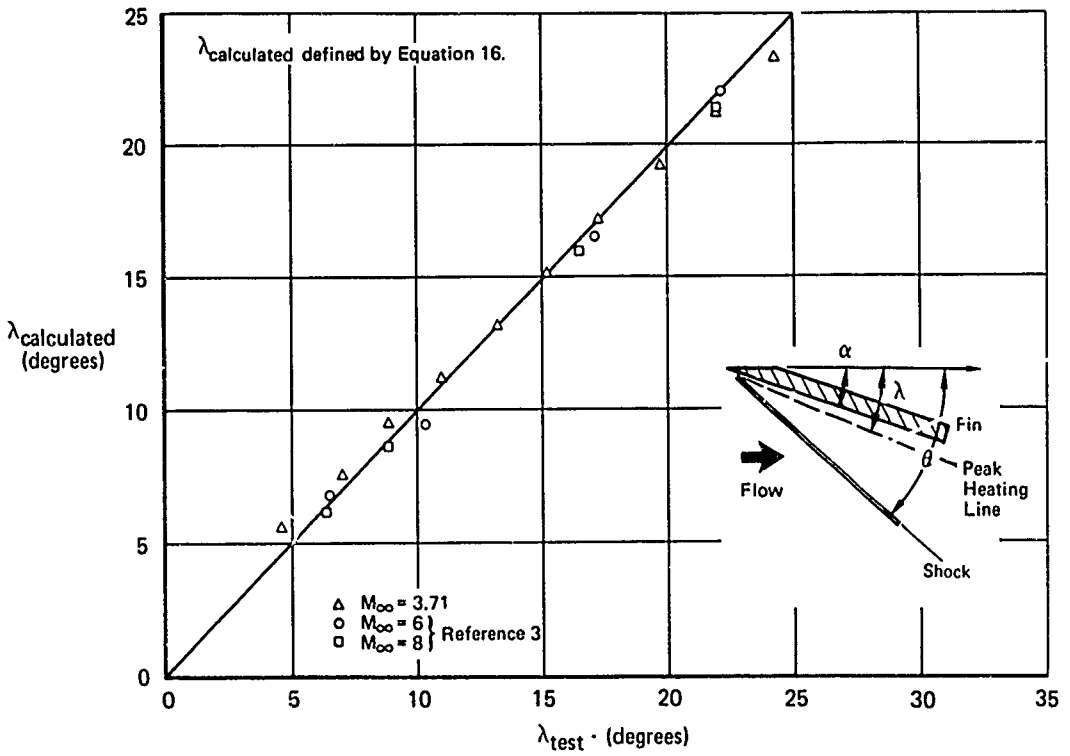

FIGURE 36 .MPROVED SHARP FIN PEAK HEATING LOCATION CORRELATION

number is relatively constant. Furthermore, the orientation of the peak heating locus can be expressed as a constant fraction of that included angle. The correlation is given as

$$\lambda_{calculated} = \mathcal{R}(\theta-\alpha) + \alpha \; ; \quad \mathcal{R} = 0.24 \tag{16}$$

This correlation is shown in Figure 36 with data from Reference 3 at Mach numbers 6 and 8 included. As illustrated, the correlation evidently contains adequate Mach number dependence which is implicit in the relationship between the fin and shock wave angles. Figure 37 is a comparison between the location defined by the correlation of Figure 36 and the measured data. Comparing Figure 37 with Figure 35 indicates that the more physical correlation is not as precise, however, it is sufficiently accurate to define the peak heating location.

3.2.2.2 Peak Heating Magnitude - The peak heating increases with increased fin deflection angle or impinging shock strength and with increasing distance aft of the fin leading edge along the peak heating locus as shown in Figure 14. Figure 18 illustrates a similar downstream influence of the peak

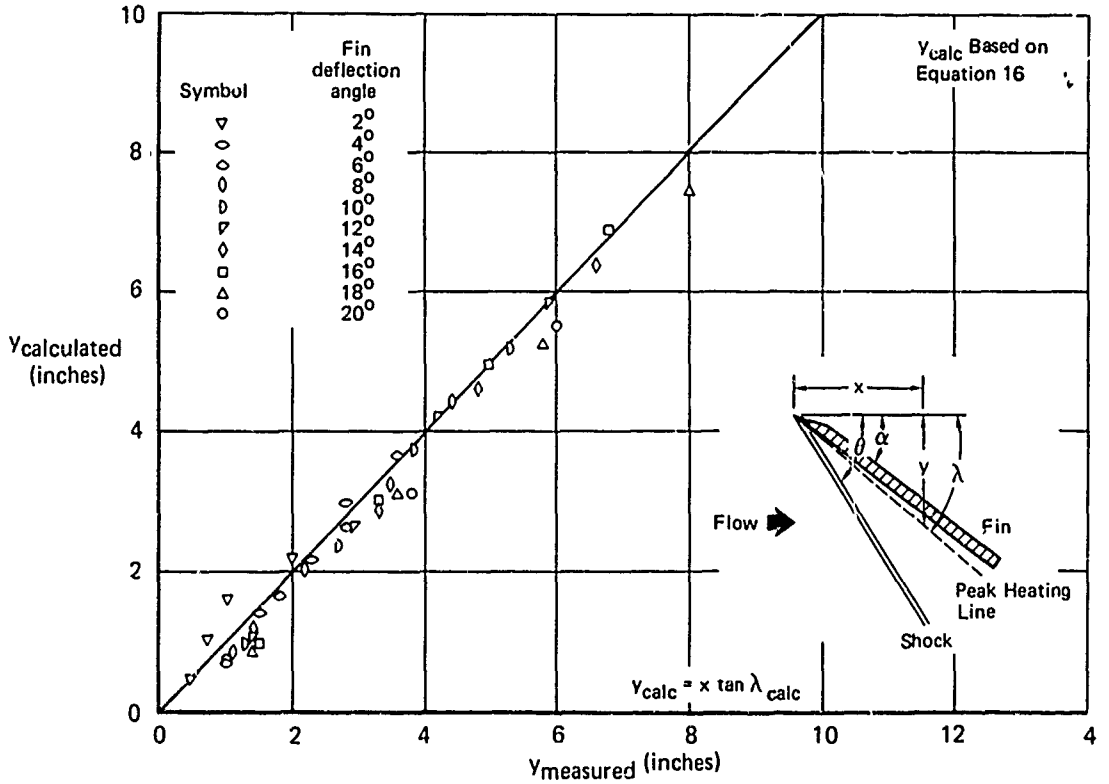

FIGURE 37 COMPARISON OF IMPROVED SHARP FIN PEAK HEATING LOCATION CORRELATION

pressure. Based on the success achieved with two-dimensional flow data discussed in References 9 and 10, the peak heat transfer coefficient was normalized with respect to a function of the inviscid pressure ratio across the impinging shock. The pressure ratio raised to the 9/10 power correlates the data and makes it independent of fin deflection angle. This exponent is usually taken as 0.8 or 0.85 by extrapolation from two-dimensional interaction correlations, References 9 and 10. However, it can be shown by substituting the Spalding and Chi correlation for friction coefficient in the Colburn form of Reynolds analogy and deleting lower order of magnitude terms that the exponent is Reynolds number dependent, in fact equal to one minus the slope of Spalding and Chi's $c_f F_c$ vs. $FR_x\ Re_L$ correlation. For surface to free stream temperature ratios not much difference from unity, the analysis indicates that the appropriate pressure ratio exponent is approximately 0.9 at the test Reynolds number. The correlation is shown on Figure 38. The peak heating data correlation continues to increase with downstream distance.

3.2.2.3 Shock Heating Magnitude and Location - Heating under the impinging shock wave induced by the fin was chosen as an outer boundary for determining heating distributions because it is a readily identifiable location. Physically, the region under the impinging shock is in the separated flow

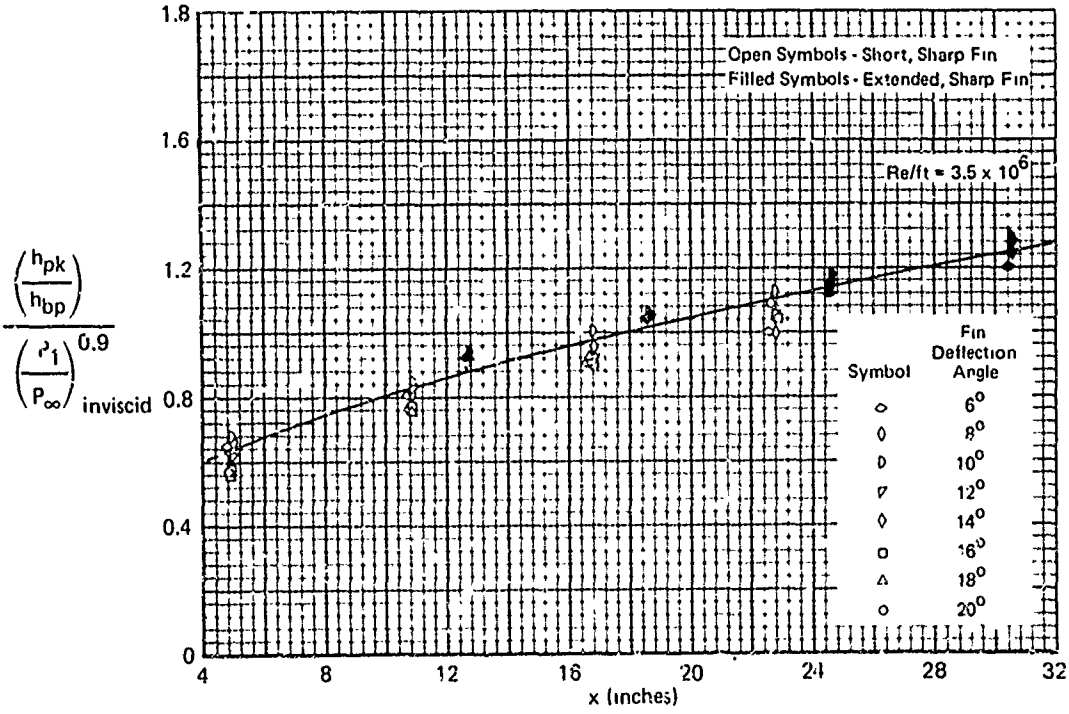

FIGURE 38 PEAK HEATING VARIATION CORRELATION - SHARP FIN

region for fin deflection angles larger than the incipient boundary layer separation angle. The shock wave location can be readily calculated using inviscid gas dynamic equations. These equations reduce to the oblique shock equations for a sharp, planar fin.

The magnitude of the normalized heat transfer coefficient under the shock for the extended sharp leading edge fin is shown in Figure 39. The data indicate an abrupt change in heat transfer coefficient magnitude at a fin deflection angle of approximately 6 degrees. Furthermore, the heating appears to be only weakly dependent on distance downstream of the fin leading edge. The straight lines which have been drawn through the data represent the suggested correlation for this limited group of data. This line is most probably dependent upon Mach number and hence no formal correlation was attempted since, at this writing, data which define this dependence were not available.

3.2.2.4 Determination of Empirical Parameters - The heating distribution analysis technique can be completely specified by determining the values of n and C in Equation (15) since the location and magnitude of peak and shock heating have been correlated or defined. Numerical values for n and C are determined in this section.

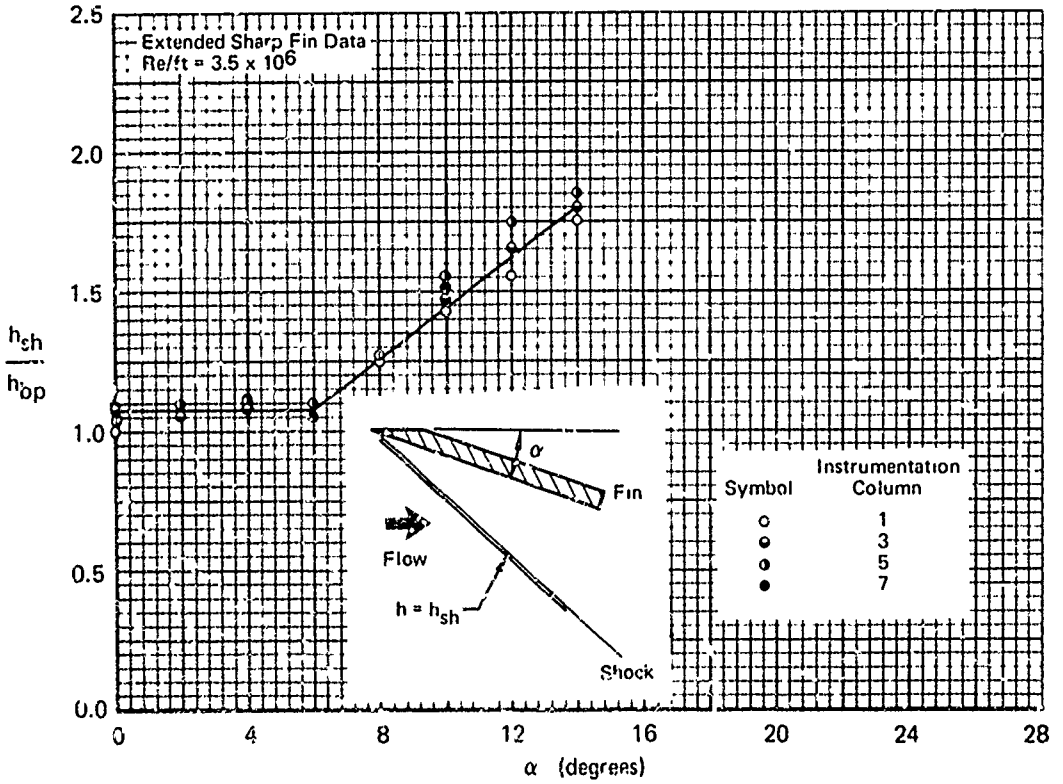

FIGURE 39 HEATING CORRELATION AT IMPINGING SHOCK

The value of C does not have a large influence on the shape of the calculated heat transfer coefficient distribution as shown in Figure 33. The surface pressure data serve to bound the value of C as, $0.2 \leq C \leq 1$. The average value for C over the fin deflection angle range is $C_{avg} = 0.41$. This average value of C is used to correlate the data.

The appropriate value of n can be determined by checking data at any fin angle. Data for a fin deflection angle of 14°, at the higher Reynolds number for the extended sharp leading edge fin, was chosen. This choice was made since it represents data at the highest fin deflection angle for the extended fin and since the value of C is approximately equal to $C_{avg} = 0.41$ at $\alpha = 14°$. Thus, these data are the most precise for evaluating the value of n.

A value of $n = 0.5$ correlates the heating distribution data extremely well, as illustrated in Figure 40. All measured data at $\alpha = 14°$ for the selected fin at $R_e = 3.5 \times 10^6$ per foot are shown in the figure. Hence, n in Equation (15) is set equal to 0.5.

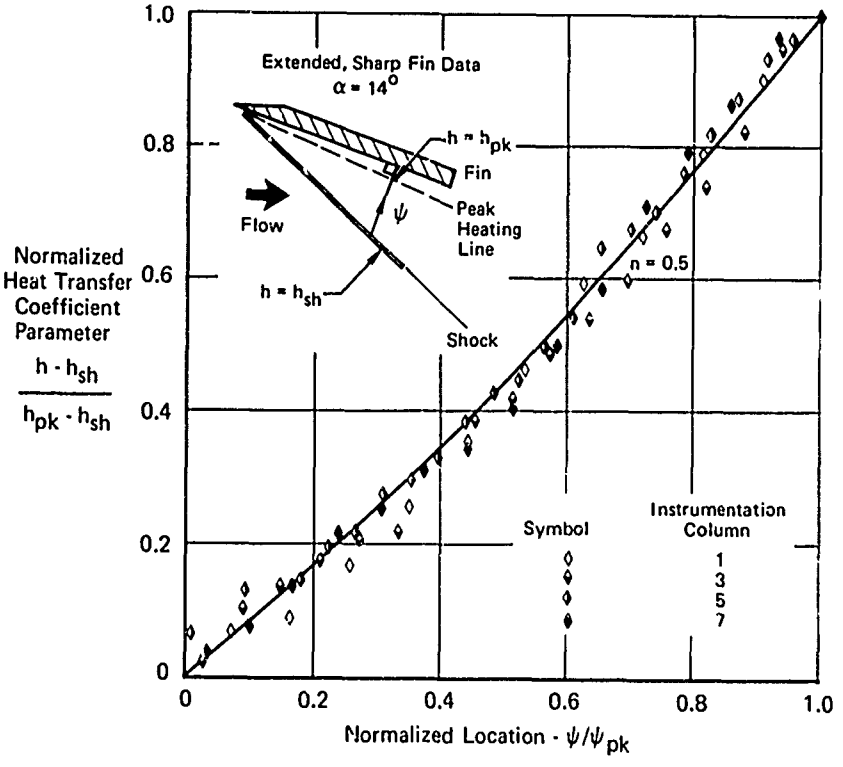

FIGURE 40 HEATING DISTRIBUTION CORRELATION

The heat transfer distribution correlation represented by Equation (15) will be compared with other sharp fin and blunt fin data in Sections 3.3 and 3.4 with n = 0.5 and C = 0.41, and with boundary conditions correlated in Figures 33, 36, and 37.

3.3 Correlation of Sharp Fin Results

Sharp fin flow field and heating data was emphasized in the experimental program discussed in Section 2. Characteristic flow field parameters are correlated and discussed in this section. The sharp fin correlations and analytical heating distribution developed in Section 3.2 are compared with remaining sharp fin data in this section.

3.3.1 Sharp Fin Flow Field Correlations - The flow field in the interaction region is not adequately understood, however, certain aspects of the flow field can be compared and correlated to show dependence on flow parameters and for mutual consistency. Incipient separation, surface pressures and pitot pressure profiles are discussed.

3.3.1.1 Three-Dimensional Incipient Separation - The oil flow data are not adequate for closely bounding the fin deflection angle which causes incipient separation. McCabe, Reference 12, has suggested that the criterion for incipient separation is that the surface streamlines (oil streak lines) must be at an angle greater than the shock wave angle in the separated region. If observed surface oil streak line angles are plotted versus fin deflection angle it can be seen that when this angle is equal to the shock angle, incipient separation has occurred by McCabe's criterion. Figure 41 illustrates this technique graphically. Also shown is the theoretical prediction suggested by McCabe which is based on a conservation of vorticity through the impinging shock wave. Figure 41 defines separation at 6.2 degrees from the experimental data and at 5.8 degrees for McCabe's analytical method. The incipient separation is a function of both fin deflection angle and Mach number since both are required to specify shock strength. The data point obtained from Figure 41 by the McCabe criterion is plotted with other available data and McCabe's theory in Figure 42. The data point obtained from this study is in general agreement with other available data and McCabe's theory. These data alone do not specify incipient separation since they are based on McCabe's definition of separation and not a pure measurement.

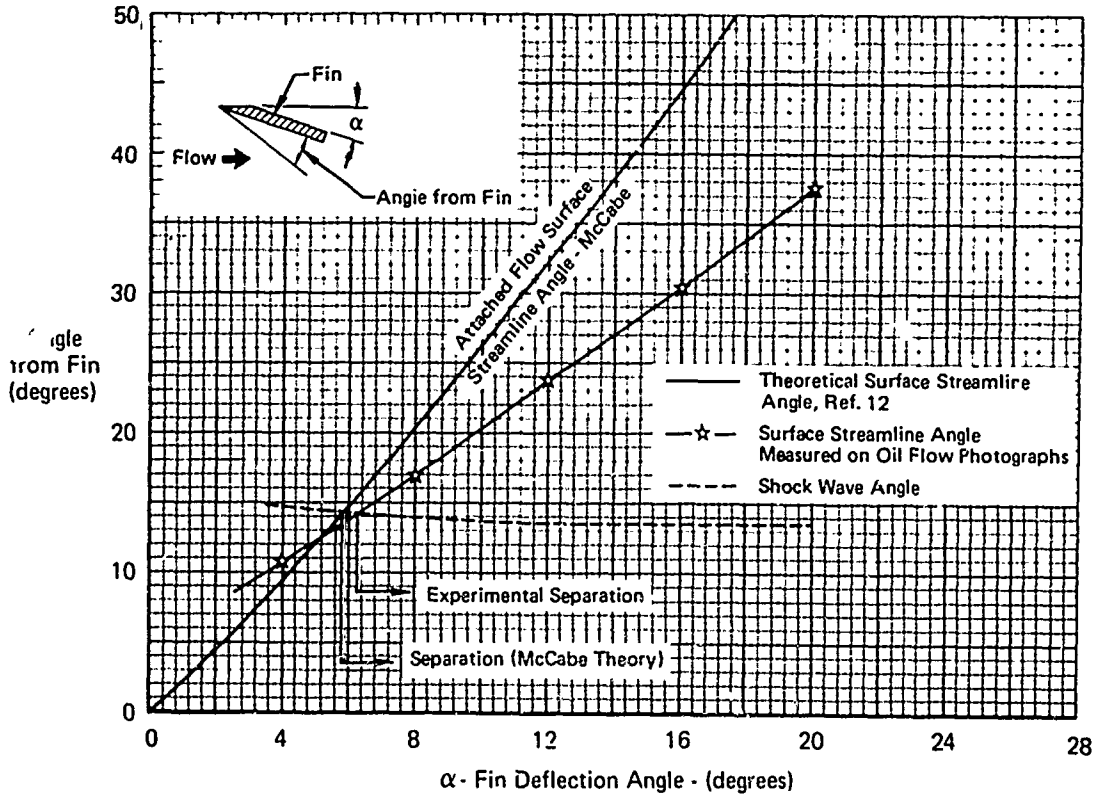

FIGURE 41 INCIPIENT SEPARATION BY McCABE'S CRITERION

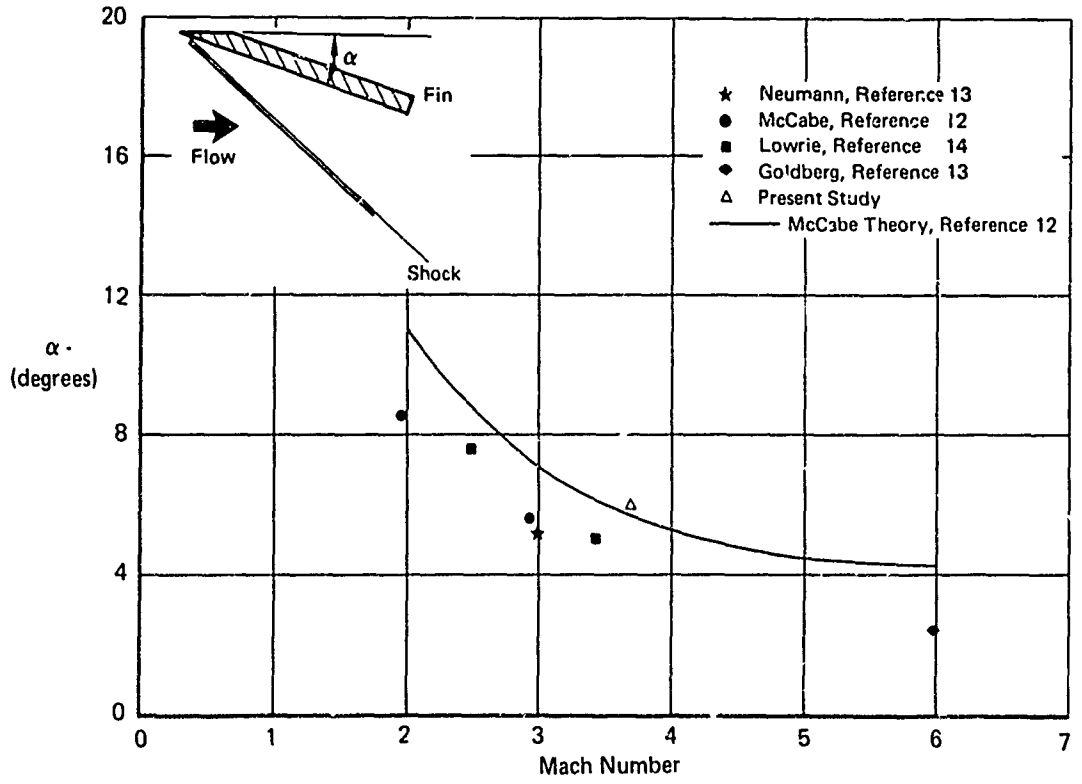

FIGURE 42 INCIPIENT SEPARATION ANGLE BASED ON McCABE'S CRITERION

A rather abrupt change in heat transfer coefficient measured at the impinging shock wave location was observed at about a 6 degree fin deflection angle in Figure 39. This tends to support the McCabe criterion for incipient separation since it implies that a drastic change in local flow field occurs at approximately the 6 degree fin deflection angle for the test Mach number of 3.71.

It is interesting to note that the three-dimensional incipient separation angle obtained by McCabe's criterion is less than the two-dimensional incipient separation angle reported by References 15 and 16. This behavior suggests that the three-dimensional incipient separation problem requires more experimental attention and consideration as a design criterion, particularly as it impacts on engine inlets and control surfaces.

3.3.1.2 Surface Pressures - Pressures measured on the fin surface exhibited a wide variation, attaining values beyond the measurement error bandwidth discussed in Section 2.2. Figure 43 illustrates the maximum, minimum, and average fin surface pressures measured on the fin surface compared to the fin surface pressure levels calculated by oblique shock theory. It is perhaps fortuitious that the average measured pressure level agrees favorably with the theoretical pressure rise across the impinging shock wave. The measured peak sidewall surface pressure in the interaction region rises with downstream distance as shown on Figure 18. However, the sidewall surface pressure never attains the inviscid calculated level within the instrumented region. These non-uniform pressures agree with the concept of a highly non-uniform and three-dimensional interaction flow field.

3.3.1.3 Pitot Pressure Profiles - Sample pitot pressure profiles are shown in Figure 20. Due to the relatively large yaw sensitivity of the pitot pressure probes, as discussed in Section 2.2, no quantitative correlations are presented. The 12 and 16 degree fin deflection results are of particular interest since for these configurations the flow field is separated by McCabs's criterion and the outer pitot probe is located in the freestream. This situation is illustrated in Figure 44. As shown, the outer pitot probe should sense freestream pitot pressure whereas the remaining pitot probes are inside the interaction region. Also shown in the figure is the location of the observed separation line. From surface pressure data at the same fin configuration and flow variables, the plateau surface pressure characteristic of the separated region can be located spatially and its magnitude can be identified. The oblique and swept shock wave angle required to produce the measured plateau

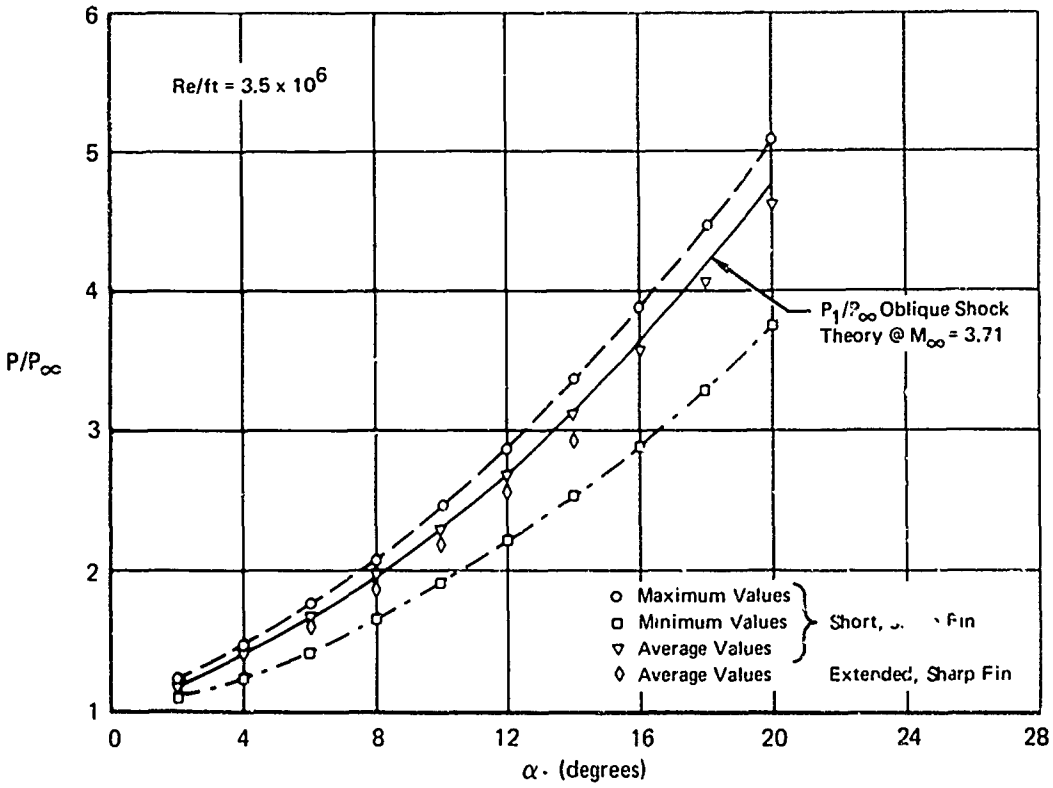

FIGURE 43 FIN SURFACE PRESSURES

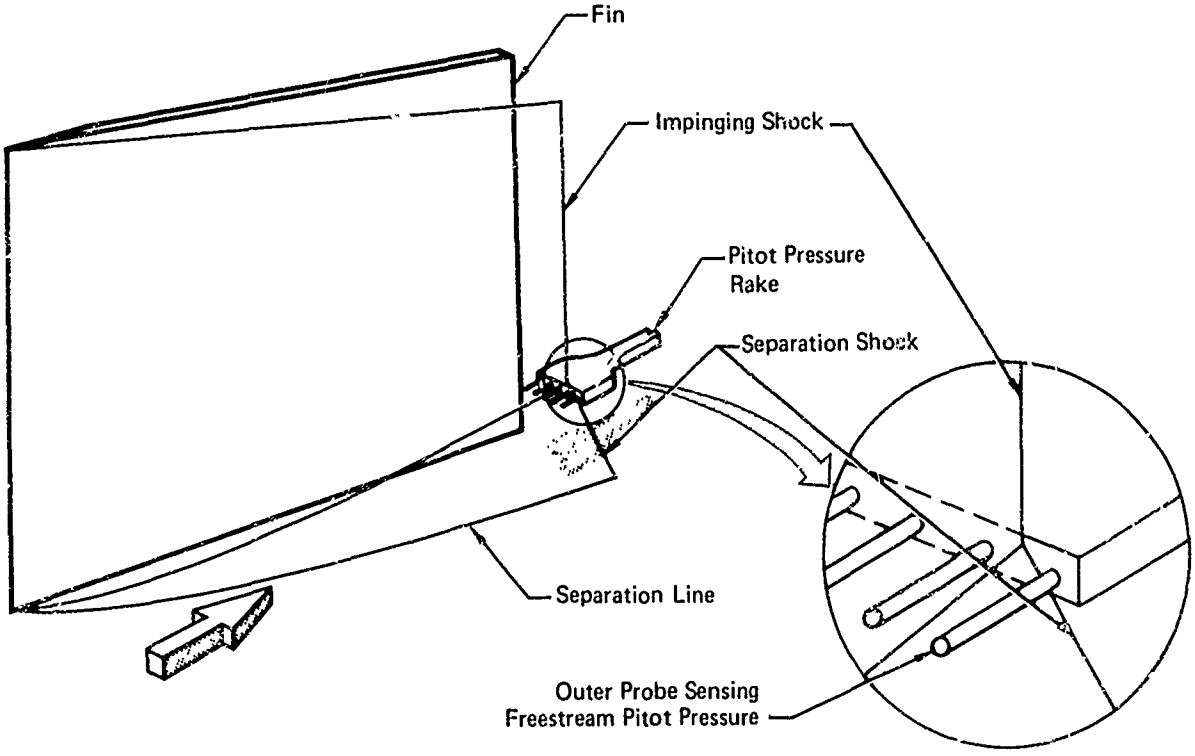

FIGURE 44 PITOT PROBE DATA INTERPRETATION

pressure can be determined. Since this shock must terminate at or near the separation line, the shock can be drawn by assuming that it intersects the separation line on the surface and intersects the impinging shock. As illustrated in Figure 44, the shock passes between the outer pitot probe and remaining probes. This is not a direct validation of impinging shock bifurcation near the plate surface, but it does support that hypothesis. Physically this agrees with the concept of a separation shock lying obliquely upstream of the impingement shock.

3.3.2 Sharp Fin Heat Transfer Correlations - The heat transfer coefficient distribution analytical method and correlations discussed in Section 3.2 are compared to sharp fin interaction region heat transfer data in this section. The heating distribution analysis and correlations were developed for sharp leading edge fin geometries based on high Reynolds number, extended fin data. These correlations are compared to short leading edge fin data, data at fin deflection angles other than 14 degrees, and to data obtained at a Reynolds number of 1.5×10^6 per foot.

3.3.2.1 Peak and Shock Heating Levels - Correlations for sharp fin peak and shock heating levels were obtained for high Reynolds number data and selected fin configurations. The correlations obtained for peak heating location and magnitude in Figures 36 and 38 include data for all fin deflection angles and both short and extended leading edge fins. Figure 45 illustrates that the correlation for peak heating magnitude is also valid for the lower Reynolds number, $Re/ft = 1.5 \times 10^6$.

The correlation obtained for shock heating magnitude at high Reynolds number and for the extended sharp fin in Figure 39 is compared with lower Reynolds number and short fin data in Figure 46. The agreement obtained indicates that the correlations for shock heating are invariant over the Reynolds number range and are independent of location under the shock.

3.3.2.2 Heating Distribution Correlations - The peak and shock heating magnitudes and locations have been shown to be valid at both Reynolds numbers regardless of distance aft of the fin leading edge, or fin angle if the fin deflection angle is greater than the incipient separation angle. The heating technique is compared to data obtained at both Reynolds numbers, at all fin deflections above the incipient separation angle, and at all distances aft of the sharp fin leading edge.

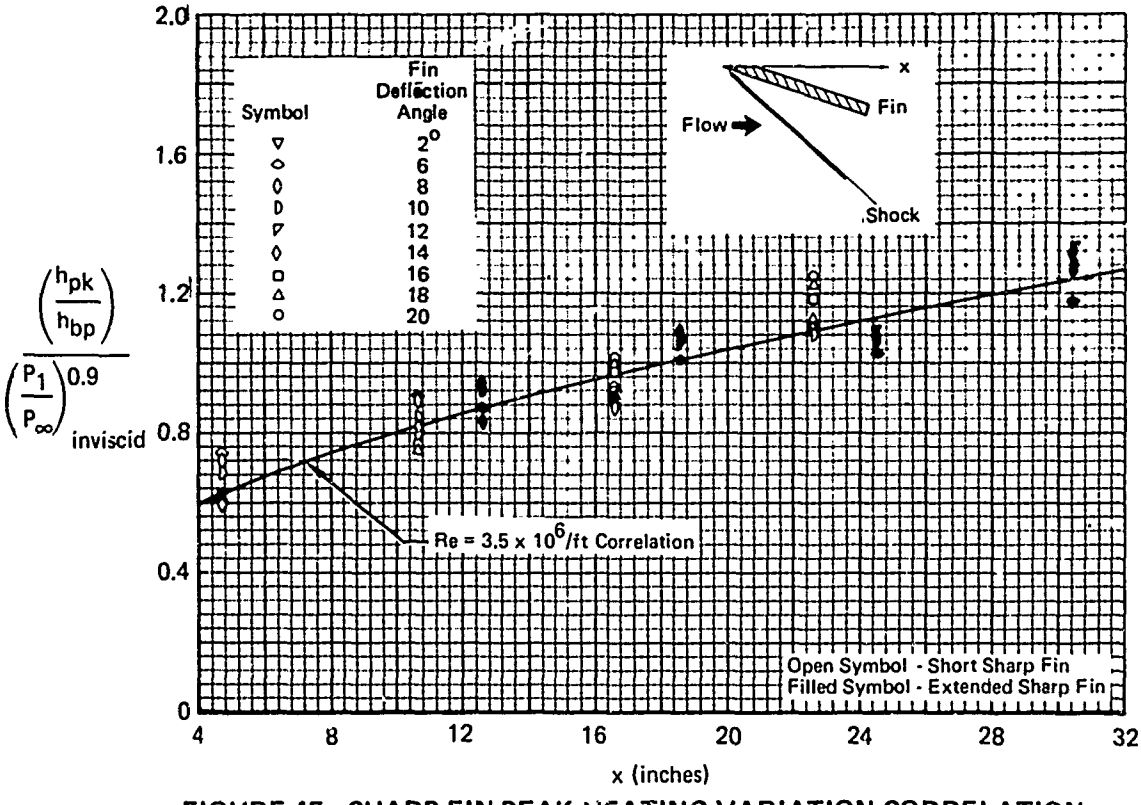

FIGURE 45 SHARP FIN PEAK HEATING VARIATION CORRELATION
Re/FT = 1.5 x 10^6

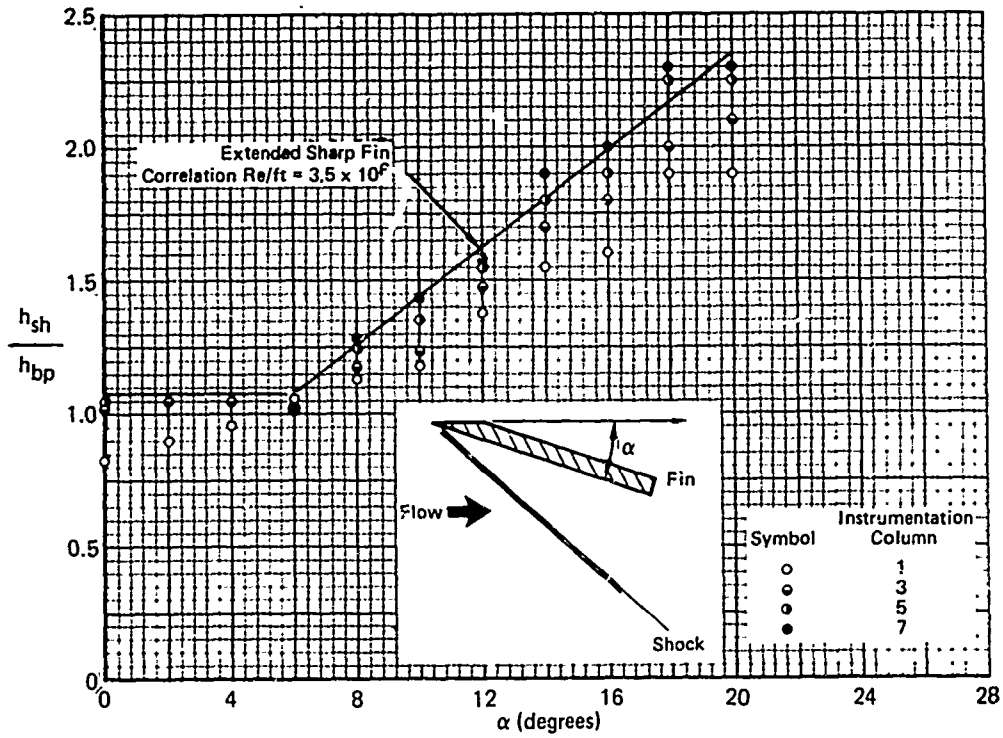

a. Short, Sharp Fin, Re/Ft = 3.5×10^6

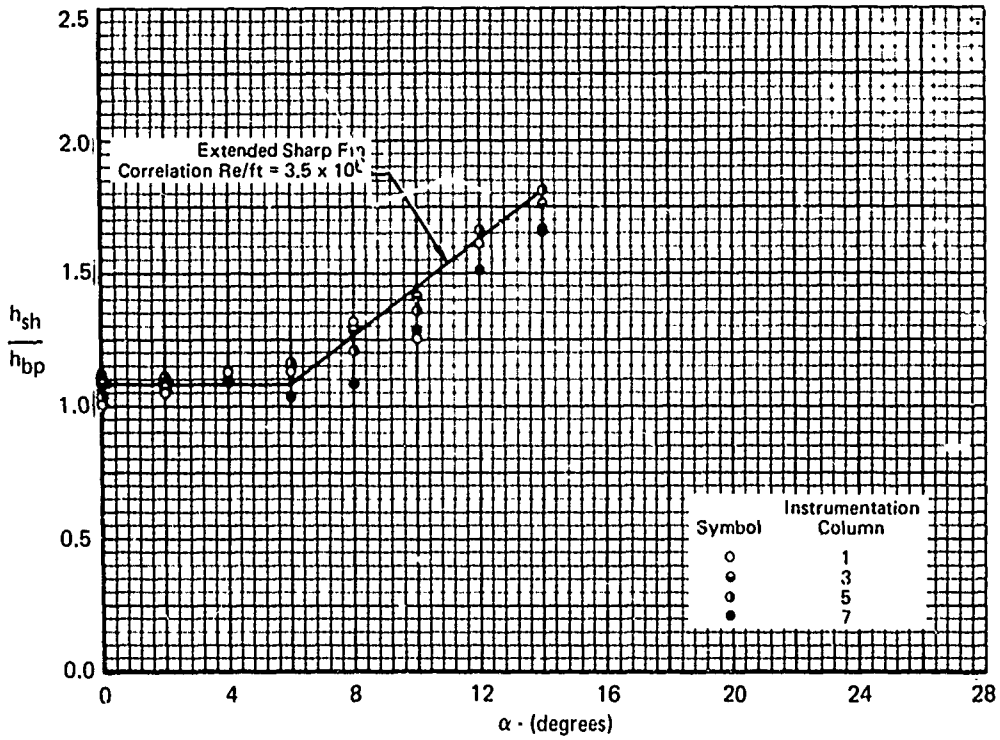

b. Extended Sharp Fin, Re/Ft = 1.5×10^6

FIGURE 46 IMPINGING SHOCK HEATING CORRELATION COMPARISON

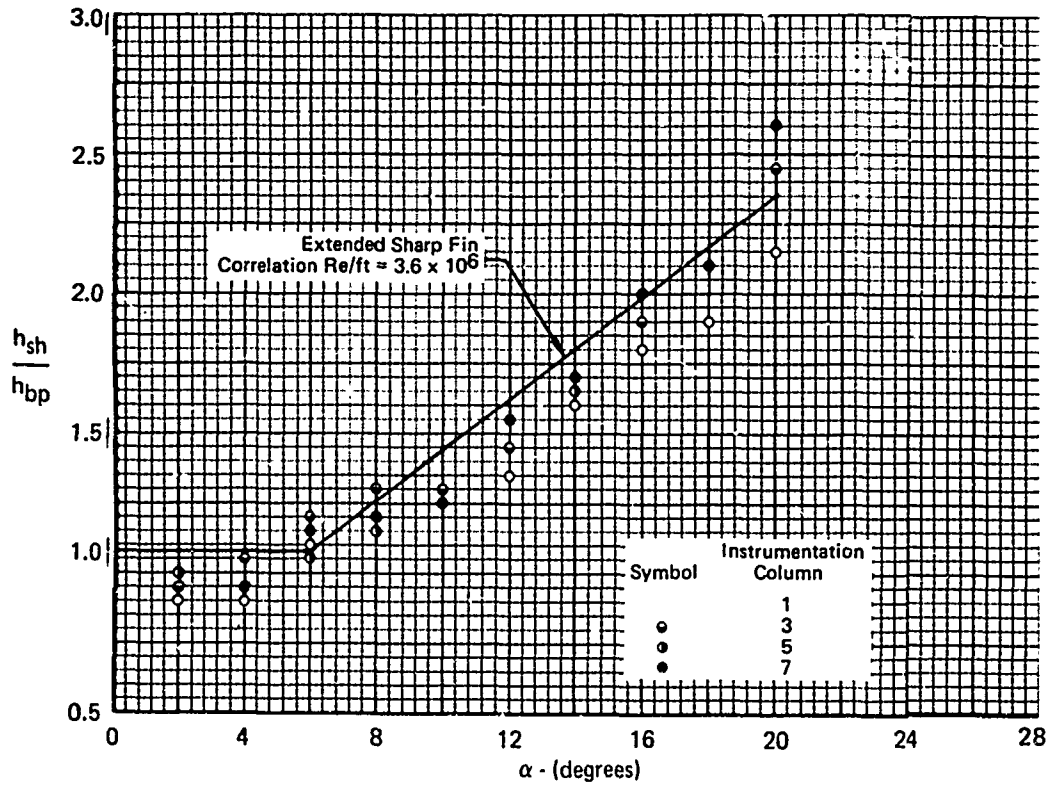

c. Short Sharp Fin, Re/Ft = 1.5 x 10^6

FIGURE 46 IMPINGING SHOCK HEATING CORRELATION COMPARISON (Concluded)

The heating distribution for all fin deflection angles above 6 degrees for the sharp extended fin at a unit Reynolds number of 3.5×10^6 per foot is illustrated in Figure 47a. All of the data are not plotted in order to avoid confusion. Data at fin angles of 6 degrees or less are deleted since they lead to poor agreement as would be expected by McCabe's incipient separation criterion.

The heating distribution obtained at all fin deflection angles above 6 degrees for a unit Reynolds number of 3.5×10^6 per foot, for the short sharp fin is illustrated in Figure 47b. For similar reasons as those used for constructing Figure 47a, the data for fin deflection angles of 6 degrees or less are not shown. In addition, all data from instrumentation column number 1 have been deleted. Column number 1 data for the short fins is close to the fin leading edge (less than 0.8δ), in the region where the separation line and hence the separation shock is highly curved. Similarity in the heating profiles, when plotted in the appropriate non-dimensional form, is attained in regions lying at least a distance greater than 0.8δ downstream of the fin leading edge.

The influence of reduced Reynolds number on the heat transfer distribution correlations is illustrated in Figures 47c and 47d. Consistent with Figures 47a and 47b, data for fin deflection angles of 6 degrees or less have been deleted. Figure 47c contains extended sharp fin data and Figure 47d illustrates the short fin data correlation with column number 1 data deleted. Deletion of column number 1 data is consistent with the data illustrations provided in Figure 47b since column number 1 is apparently too close to the short fin leading edge and presumably in the non-similar portion of the flow field. The wider data spread illustrated in Figures 47c and 47d at lower Reynolds number compared to Figures 47a and 47b at high Reynolds number is consistent with the data accuracy at lower Reynolds number discussed in Section 2.2.1. A Reynolds number influence could not be separated from the data inaccuracy inherent in the low Reynolds number data.

3.4 Blunt Fin Heat Transfer Correlations

The flow field in interaction regions is highly dependent upon local geometry, as discussed in Reference 1. It is anticipated that the surface heating is strongly coupled with and dependent upon the interaction region flow field. Hence, it is anticipated that the surface heating is also highly

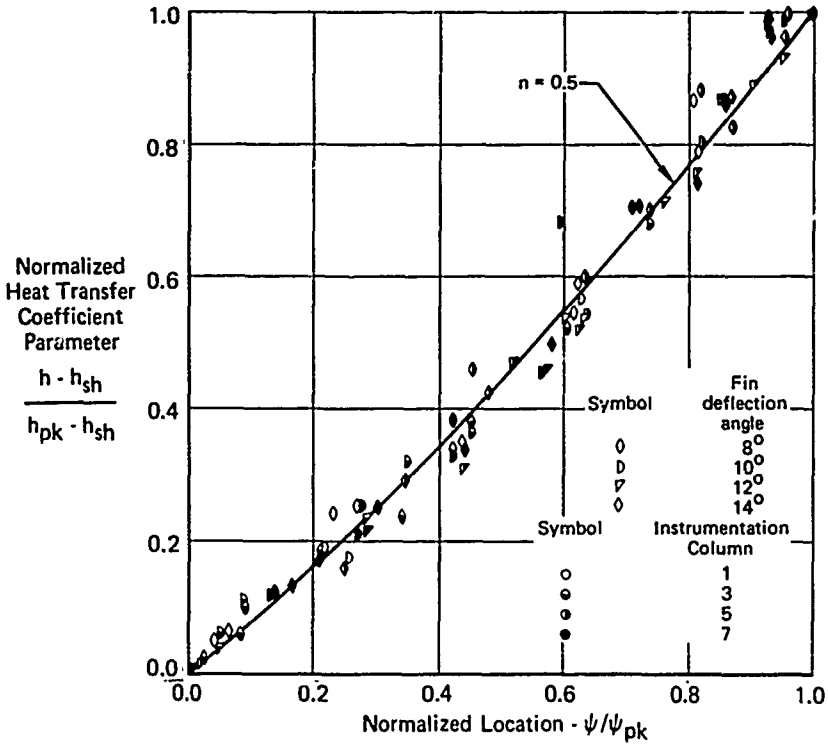

a. Extended Sharp Fin, Re/Ft = 3.5×10^6

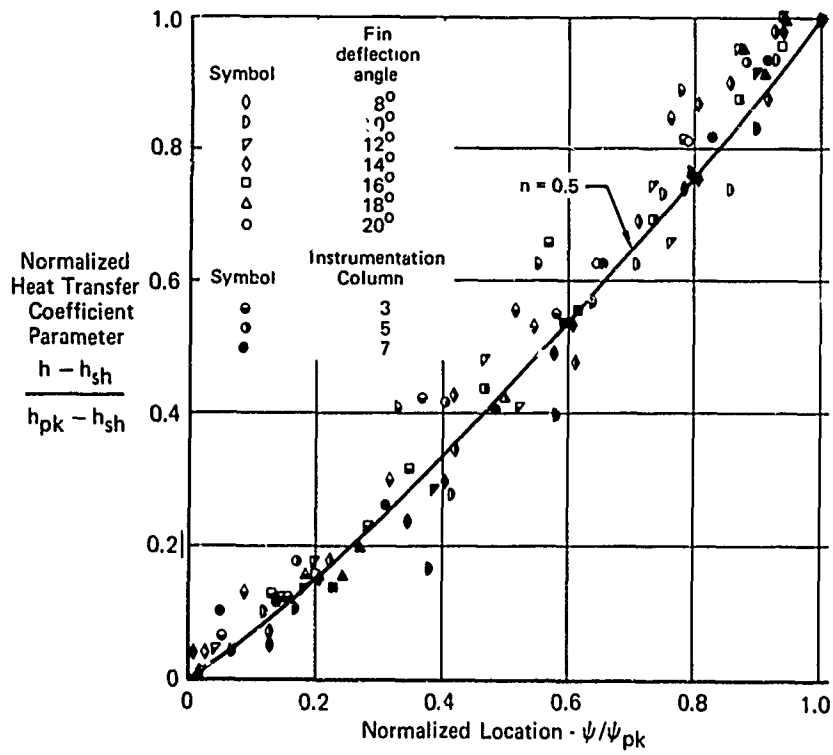

b. Short Sharp Fin, Re/Ft = 3.5×10^6

FIGURE 47 HEATING DISTRIBUTION CORRELATION COMPARISON

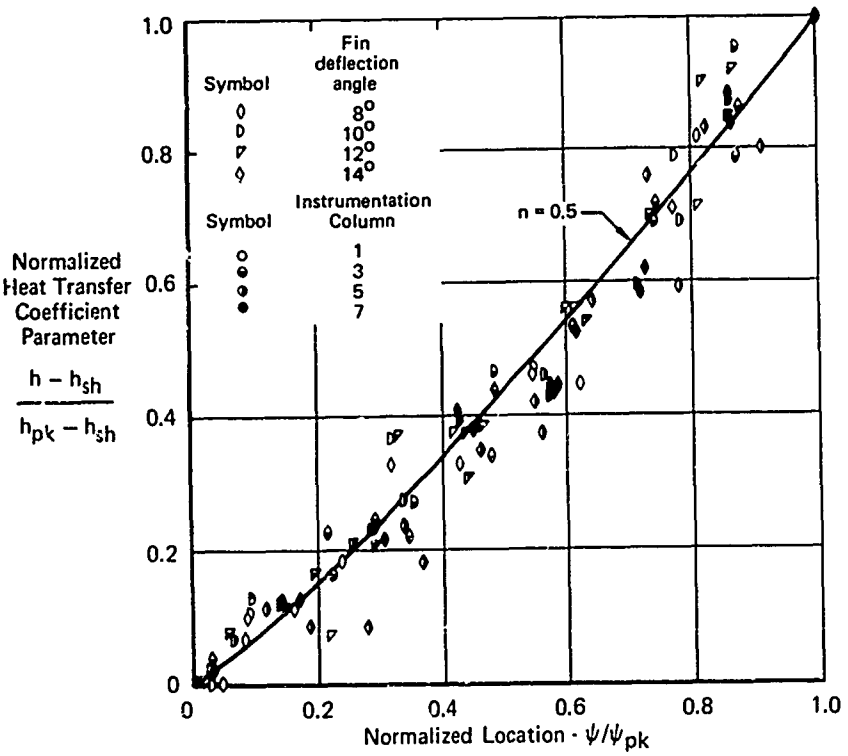

c) Extended Sharp Fin, Re/Ft = 1.5 x 10^6

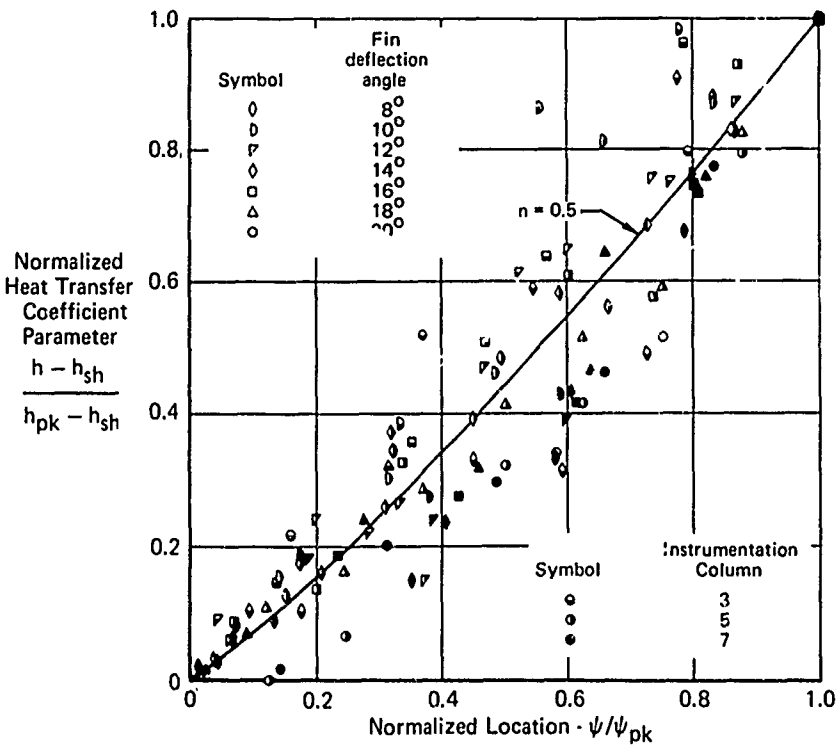

d. Short Sharp Fin, Re/Ft = 1.5 x 10^6

FIGURE 47 HEATING DISTRIBUTION CORRELATION COMPARISON (Concluded)

dependent upon local fin and surface geometry. Nevertheless, it is of interest to determine how well the sharp fin heating correlations of Section 3.2 compare with data from blunt and blunt swept fins.

3.4.1 Blunt and Blunt Swept Fin Peak Heating Magnitude - Due to the fin bluntness, the sidewall boundary layer is always separated in the leading edge region of blunt fins. This occurs even for those cases wherein the fin deflection angle is not sufficient to cause separation for the associated sharp leading edge fin. In Figure 48, the 2 and 6 degree fin deflection angle data are correlated on separate and distinct curves, whereas the 10 and 14 degree data can be correlated with a single curve. The pressure ratio (P_1/P_∞) was obtained by calculating the oblique shock for the associated sharp leading edge fin. In all cases the data appear to asymptotically approach the sharp fin data correlation at a sufficient distance downstream. Even for those cases where the fin deflection angle alone is not large enough to cause separation, the bluntness induced separation effects appear to propagate downstream. The sharp fin peak heating magnitude correlation on Figure 48a, appears to be valid at a distance of 5 to 6 boundary layer thicknesses downstream for all blunt fin deflection angles. The data correlation is not refined further since there is insufficient data to include other physical parameters.

The variation of blunt swept fin peak heating magnitude is shown in Figure 48b. In this figure both 45 and 60 degree sweep effects are indicated and the inviscid pressure ratio used to modify the heat transfer ratio is the sharp unswept fin value calculated by oblique shock equations. The flow field, at least in the vicinity of the fin leading edge, is separated due to fin bluntness. These data are very similar to the unswept blunt fin data on Figure 48a except that the level is reduced. Due to the sparse data no further refinement in the correlation was attempted. The data illustrate the important practical conclusion that fin sweep reduces peak heating magnitude. This conclusion could have been anticipated in view of the reduced pressure level caused by the influence of fin sweep on shock strength.

3.4.2 Blunt and Blunt Swept Fin Peak Heating Location - A correlation of peak heating location is complicated by the blunt fin geometry. A correlation of the type given in Figure 36 is not practical since the leading edge is blunt and a unique shock angle cannot be defined. Recalling the success achieved with the more empirical of the two sharp fin correlations illustrated in Figure 33, the blunt and blunt swept fin peak heating location data was investigated to

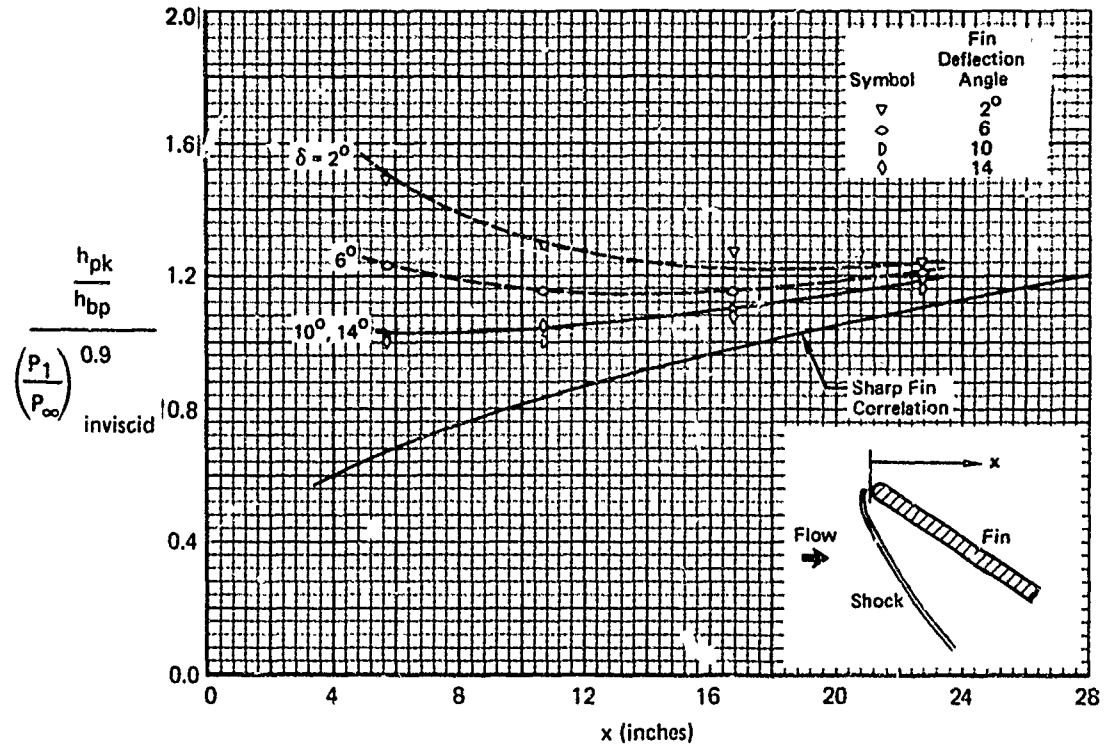

a. Blunt Fin

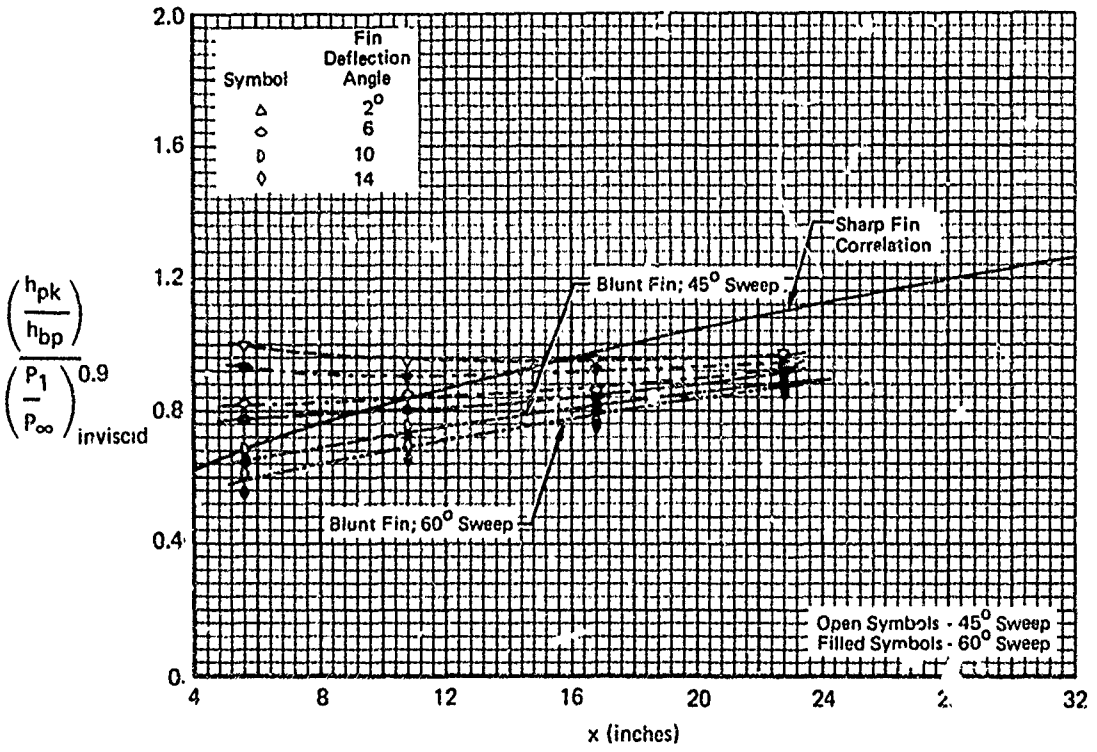

b. Blunt Swept Fins

FIGURE 48 PEAK HEATING VARIATION COMPARISON

determine if the peak heating line was oriented at a unique angle with respect to the fin surface. Within the limits of spatial resolution provided by the thermocouple spacing, the peak heating was found to lie on a straight line oriented at an angle of 2-1/4 degrees with respect to the fin surface. This is the same angular relationship determined for the sharp fin data. The extrapolation of this peak heating line to the stagnation streamline did not intersect the stagnation streamline at a constant distance upstream of the fin leading edge. Figure 49 illustrates that the distance upstream (Δ) is dependent on fin angle. Measured values of Δ for the blunt and blunt swept fins are shown. At fin deflection angles of 6 degrees and higher, the blunt and blunt swept fin values of Δ are identical regardless of the fin sweep angle. At a 2 degree fin deflection angle, the blunt fin and 60° blunt swept fin data points are identical, but the 45° blunt swept fin data point is 29% higher. The value of Δ in Figure 49 is expressed in fin leading edge radii although all fin leading edge radii tested were identical. It is anticipated that the fin leading edge radius will have a direct influence on peak heating line intersection point. No further refinement was attempted in the correlation due to the sparse data base.

The peak heating line location is correlated as a function of Δ, α, and x in a manner similar to the sharp fin data. The correlation is of the form:

$$y_{CALC} = (x + \Delta)\ [\text{TAN}\ (\alpha + 2\ 1/4°)], \tag{17}$$

where Δ is illustrated in Figure 49. Figure 50 compares the calculated and measured peak heating location. Figure 50a illustrates the comparison for the location of the blunt non-swept fin peak heating. Figures 50b and 50c illustrate the same comparisons for the 45 degree blunt swept and 60 degree blunt swept fins, respectively. The comparisons shown are based on a highly empirical correlation which contains no parametric dependence on flow field properties such as Mach number. It is anticipated that the flow field parameters will have a decided influence on the peak heating location. Since data at other flow field conditions are not available, no attempt was made to refine the correlations.

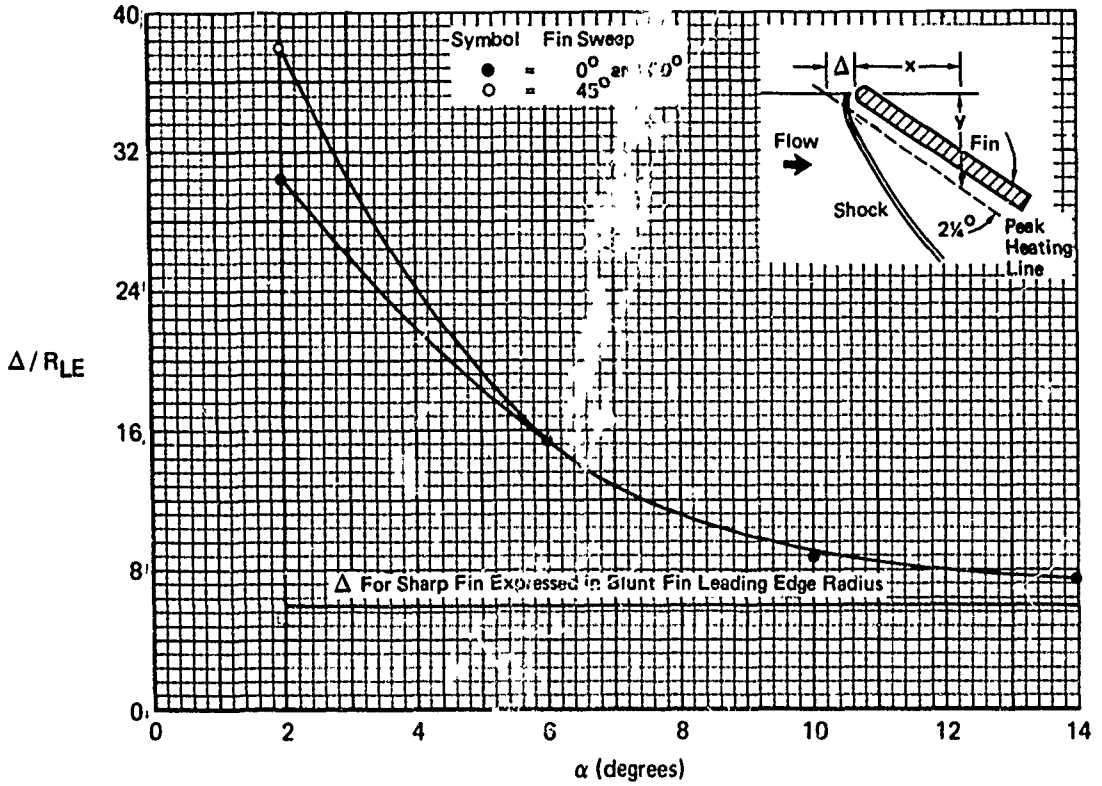

FIGURE 49 CORRELATION OF BLUNT FIN PEAK HEATING LINE ORIGIN (Δ)

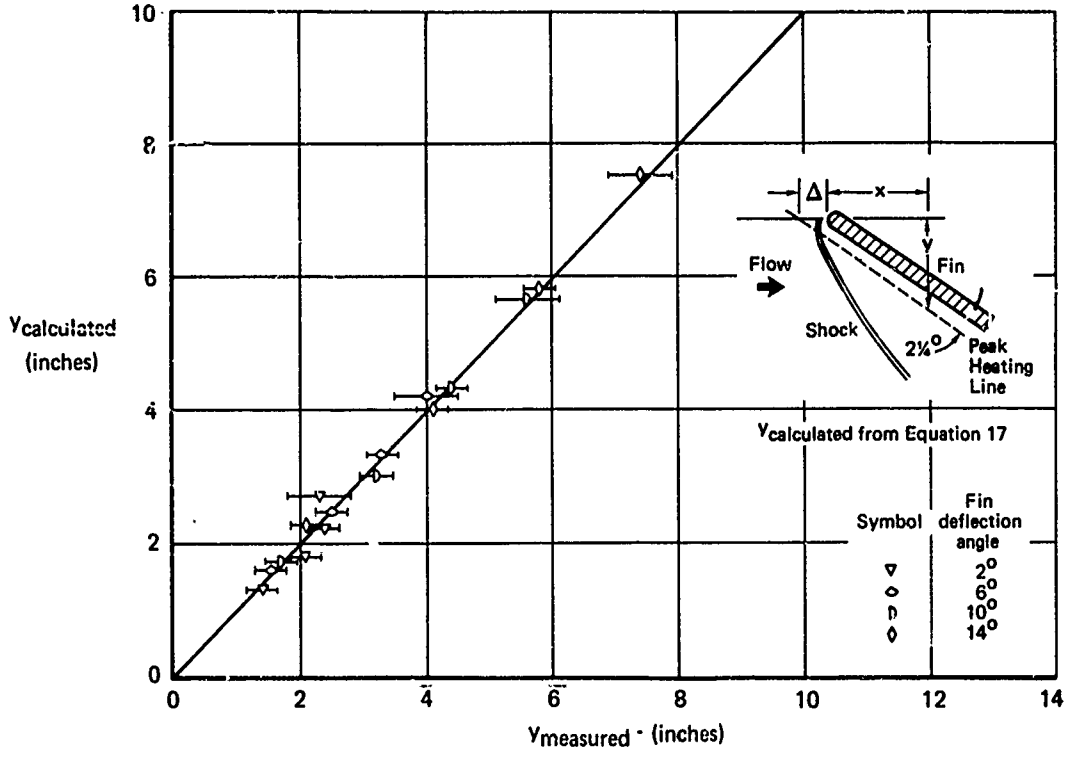

a. No Sweep

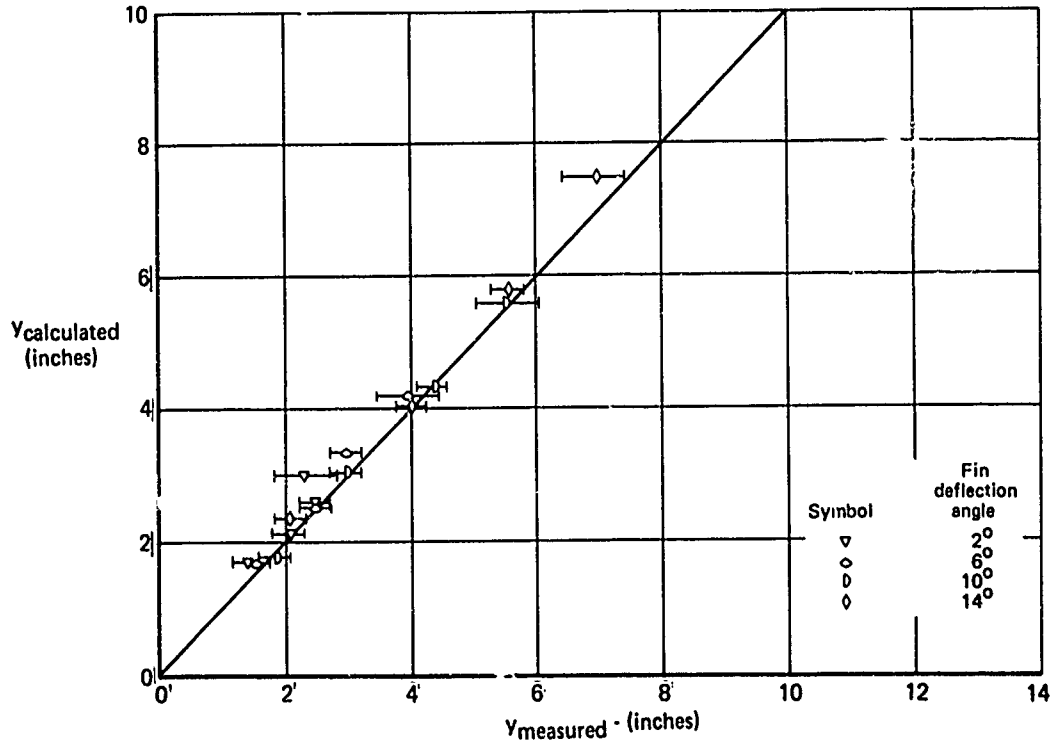

b. 45° Sweep

FIGURE 50 BLUNT FIN PEAK HEATING LOCATION CORRELATION

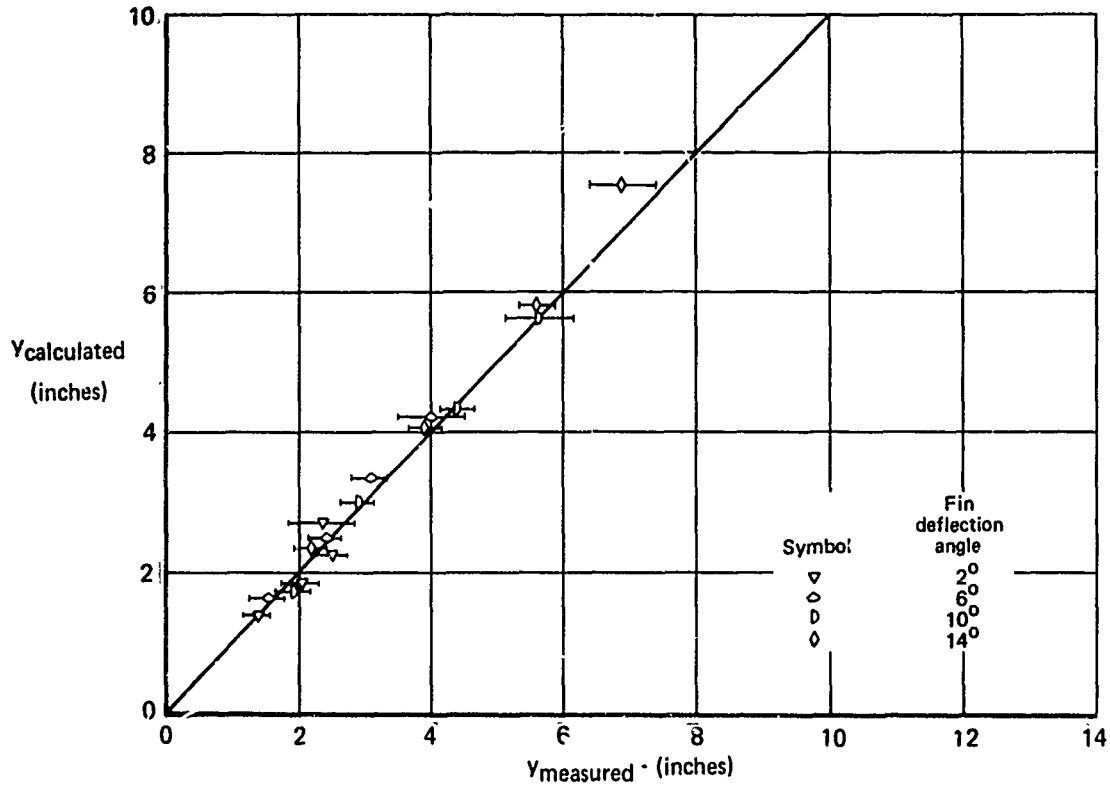

c. 60° Sweep

FIGURE 50 BLUNT FIN PEAK HEATING LOCATION CORRELATION (Concluded)

3.4.3 Blunt Fin Shock Heating and Location - The heat transfer distribution analysis requires that the location of the impinging shock wave and the heating at the shock be known. The location of the shock must be calculated by including the fin bluntness effects. Several methods exist for calculating detached shock shapes.

The blunt fin shock shape was calculated using the inverse method defined by Maslen, Reference 17. This method of shock shape calculation requires that the shock stand-off distance and shock curvature be inputed on the stagnation streamline. Furthermore, the true stagnation line is assumed to be the geometric stagnation line. The stagnation line shock stand-off distance and curvature were calculated using Barnwell's method, Reference 18. Figure 51 illustrates the calculated shock shape for the unswept blunt fin using Maslen's method.

The heating at the impinging shock was obtained at locations determined by these calculated shock shapes. The blunt fin shock heating level is shown in Figure 52. These data indicate that the entire blunt fin interaction region is separated by comparison with the sharp fin shock heating correlation line. The data indicates that heating at the shock increases with fin deflection angle in a manner similar to the separated sharp fin data. The column number 1 data is too close to the highly curved portion of the separation line to correlate with the other data.

3.4.4 Blunt Swept Fin Shock Heating and Location - Shock shape solutions are required for the blunt swept fins in order to correlate the location and magnitude of shock heating. The calculation of the shock shape solutions for the unswept sharp and blunt fins are relatively straightforward. The exact calculation of shock shapes for blunt swept fins requires a three-dimensional non-symmetric flow field solution. In order to avoid this complexity, two limiting shock shapes can be calculated which bound the true shock shape, as depicted on Figure 53. One bound can be calculated as the shape which will be a valid approximation far downstream. This limiting shape, termed the "two-dimensional limit", can be determined by calculating the shock shape normal to the swept fin leading edge using the normal component of the free stream Mach number. The shape of the resulting shock impingement path on the plate can subsequently be obtained by rotating and stretching the streamwise shock coordinate by the cosine of the sweep angle.

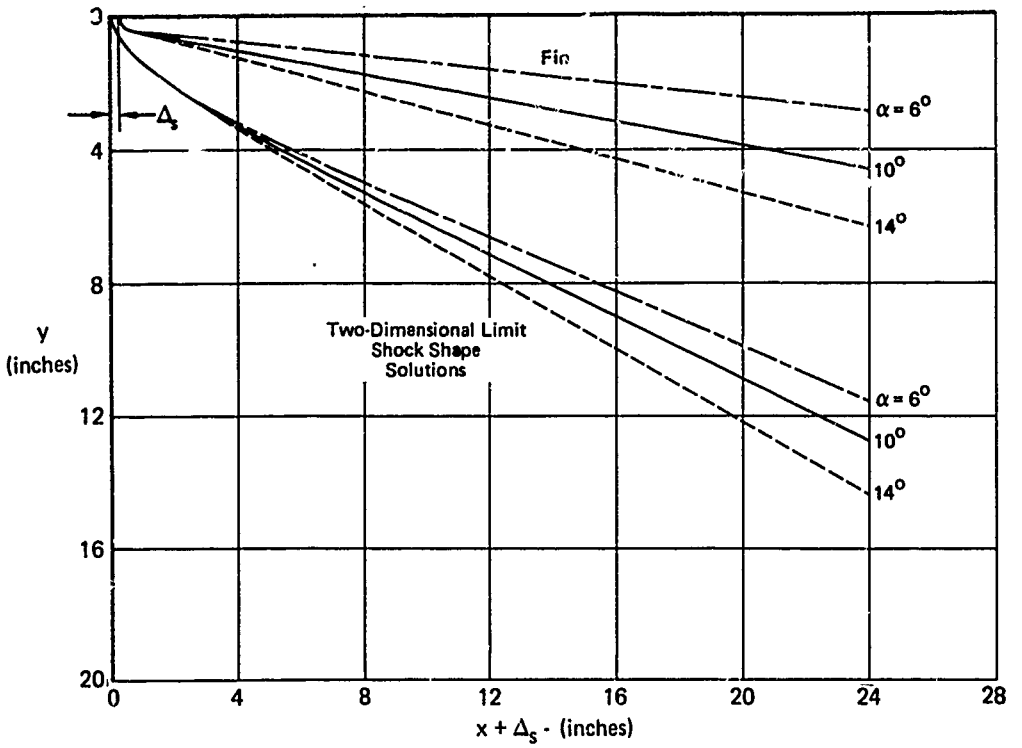

FIGURE 51 BLUNT FIN SHOCK SHAPES

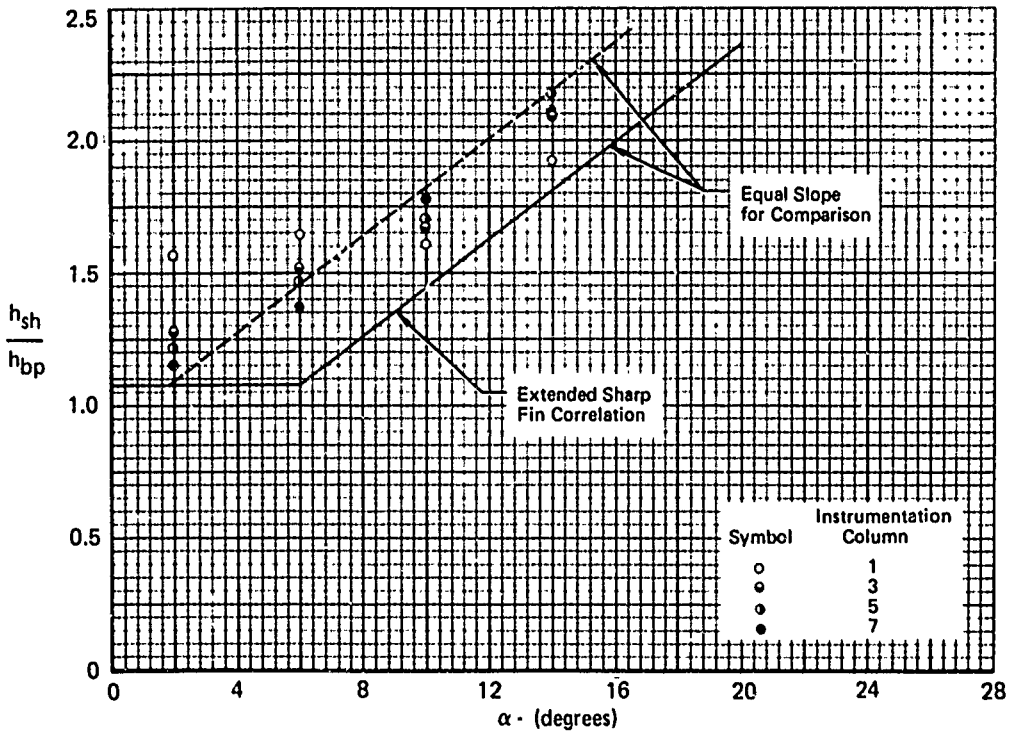

FIGURE 52 BLUNT FIN IMPINGING SHOCK HEATING CORRELATION COMPARISON

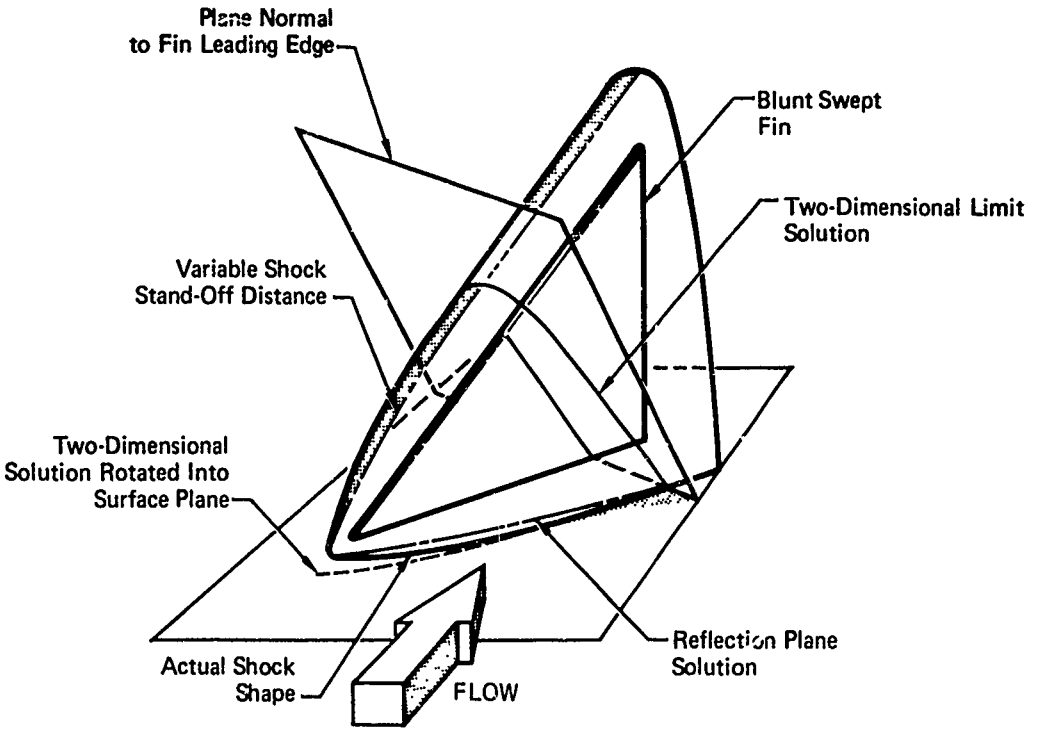

FIGURE 53 LIMITING BLUNT SWEPT FIN SHOCK SHAPE SOLUTIONS

A shock solution which is more precise in the fin leading edge-sidewall region can be calculated by using the full freestream Mach number about the appropriate elliptical shaped leading edge fin. This solution, termed the "reflection plan solution", assumes no mass flow along the swept leading edge.

In the actual case, mass does flow along the swept leading edge and hence the shock stand-off distance will vary as depicted on Figure 53. The true shock shape on the plate surface is bounded by these two limiting cases. In the stagnation region it closely resembles the reflection plane solution and sufficiently far downstream approaches the two-dimensional limit. The downstream distance required for the shock wave to approach the two-dimensional limit is a function of Mach number and fin geometry, including sweep angle and deflection angle. A reduced downstream Mach number will shorten the distance required to attain validity of the two-dimensional solution. Thus, the influence of increased fin deflection angle is to shorten the distance. Reduced sweep also decreases the distance.

The shock shape calculated using the two-dimensional limit for the blunt swept fin with a 45 degree sweep angle is illustrated in Figure 54a. Figure

54b illustrates the shock shapes calculated using the two-dimensional limit for the blunt swept fin with a 60 degree sweep angle. Figure 54c illustrates the reflection plane shock shape solution for the blunt swept, 60 degree sweep fin at a 10 degree deflection angle with its two-dimensional limit counterpart.

The heating variation at the shock calculated using the two-dimensional limit for the 45 degree swept fin is illustrated in Figure 55a. Figure 55b illustrates the heating variations at the shock defined by the two-dimensional limit for the 60 degree swept fin. The shock heating magnitude data point obtained using the reflection plane shock solution is identical to the "two-dimensional solution" data point.

The heating at the shock is used as a boundary condition because it is an identifiable point in the interaction region as discussed in Section 3.1. When the impinging shock is normal to the surface, the shock heating appears to take on unique values independent of location along the shock. This heating level is thought to be characteristic of the separated turbulent heating levels. When the fin becomes swept, the impinging shock projection to the fin surface may be upstream of the separated region. This rationale is consistent with the data on Figure 55 which show that the shock heating for the

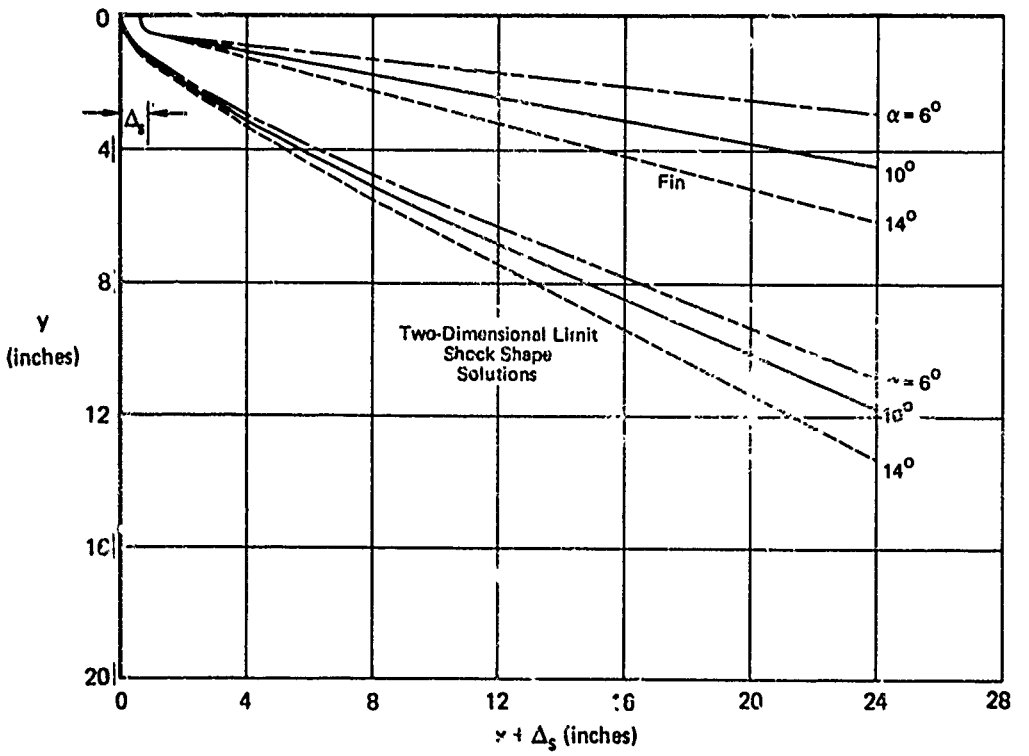

a. 45° Sweep

FIGURE 54 BLUNT, SWEPT FIN SHOCK SHAPES

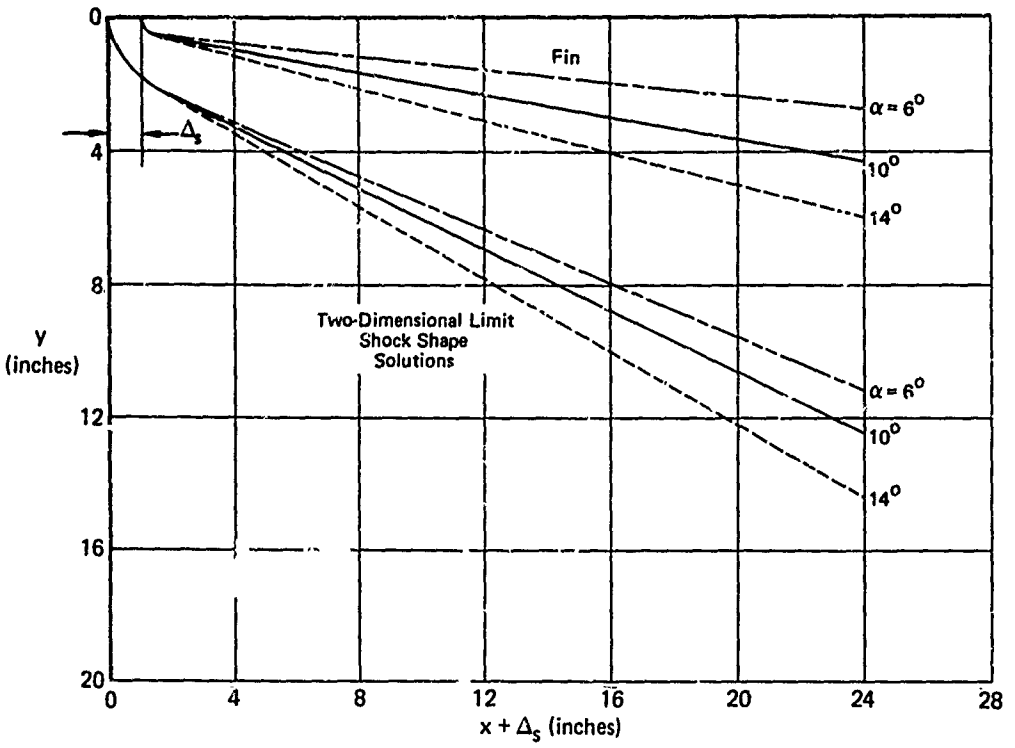

b. 60° Sweep

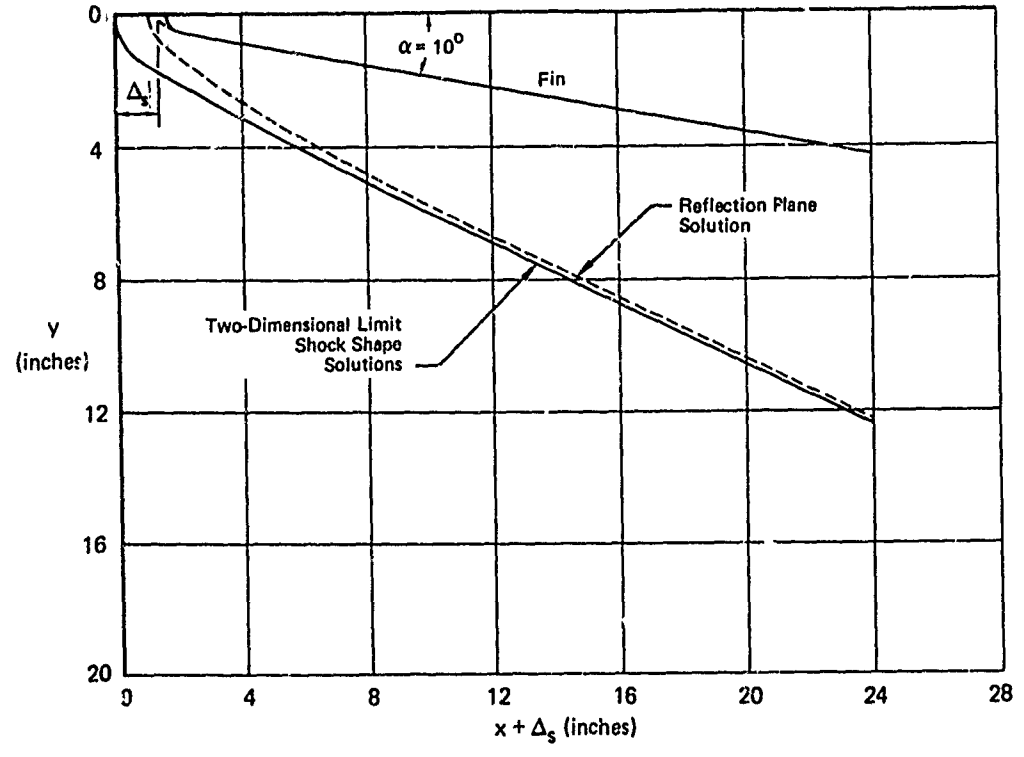

c. 60° Sweep, α = 10°

FIGURE 54 BLUNT SWEPT FIN SHOCK SHAPES (Concluded)

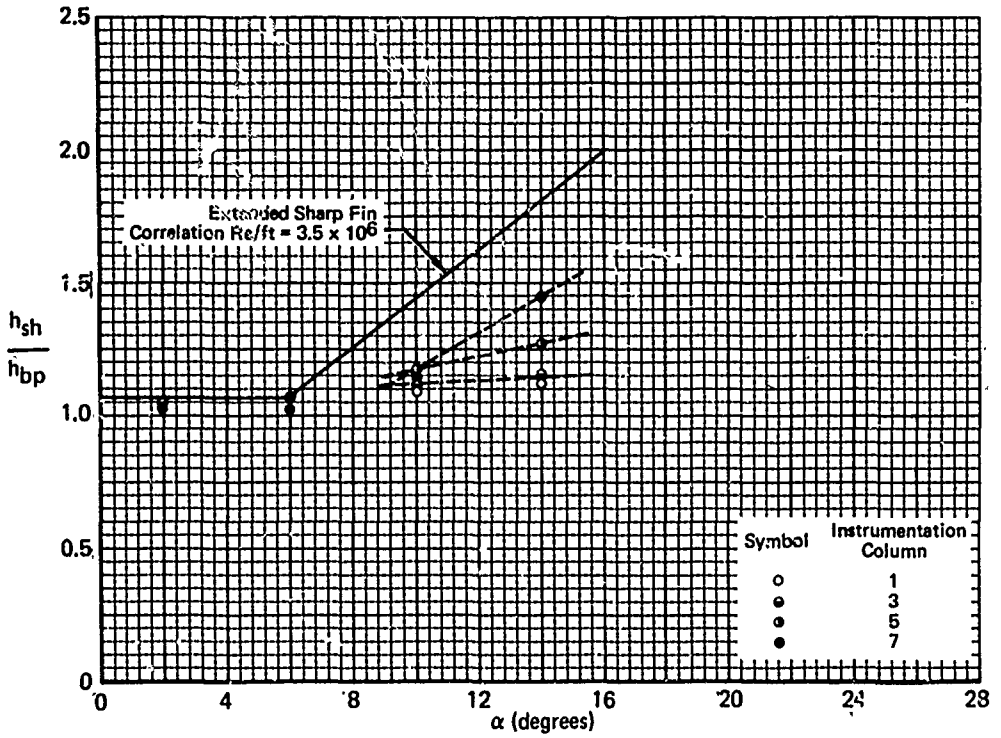

a. 45° Sweep

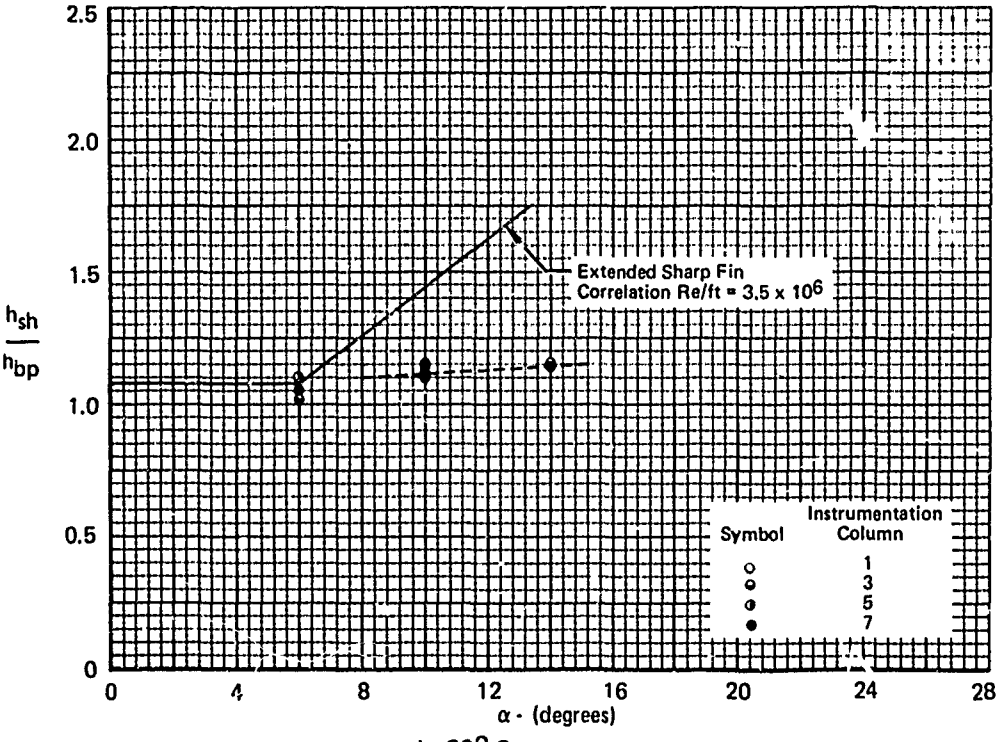

b. 60° Sweep

FIGURE 55 IMPINGING SHOCK HEATING CORRELATION COMPARISON - BLUNT SWEPT FINS

60° blunt swept fin is essentially at freestream conditions and that at the smaller sweep angle of 45° that the heating at the shock is increasing in response to the presence of the interaction. The problem is complicated further at small fin deflection angles by the nose bluntness which causes separation in the stagnation region, although the swept and deflected fin may not be capable of causing separation aft of the fin leading edge region.

3.4.5 Blunt and Blunt Swept Fin Heating Distributions - Heating distributions for the blunt and blunt swept fins can be calculated using a modified form of Equation (15), since the boundary conditions have been defined. The more complex blunt fin geometry induces a much more complex flow field as evidenced by the fact that the inviscid streamlines are not parallel between the blunt and blunt swept fins and their induced shocks. This complexity implies that heating distributions cannot be plotted in a meaningful cross flow direction, (i.e., along straight lines normal to the inviscid streamlines). The cross flow direction of (ψ^*) was, therefore, arbitrarily chosen as normal to the freestream lines for the correlation. The blunt fin heating distributions are plotted as a function of ψ^*. Figure 56 illustrates the heating distributions calculated for the blunt and blunt swept fins compared with data. All data were obtained at the higher Reynolds number and for short fins. It can be concluded that bluntness and sweep influence the flow field and hence the surface heating such that the heating distribution analysis becomes less valid. This reduced validity is primarily due to the less precise definition of the location of h_{sh}, but is also influenced by breakdown of the assumption of local similarity in the flow due to the highly curved shock wave. As evidenced by comparison of the figures, the effect of sweep has an especially large effect on the distribution. Figure 56d, which is based on the reflection plane shock solution, improves the data correlation of Figure 56c obtained using the two-dimensional shock solution. However, the improvement is not considered adequate for a good correlation.

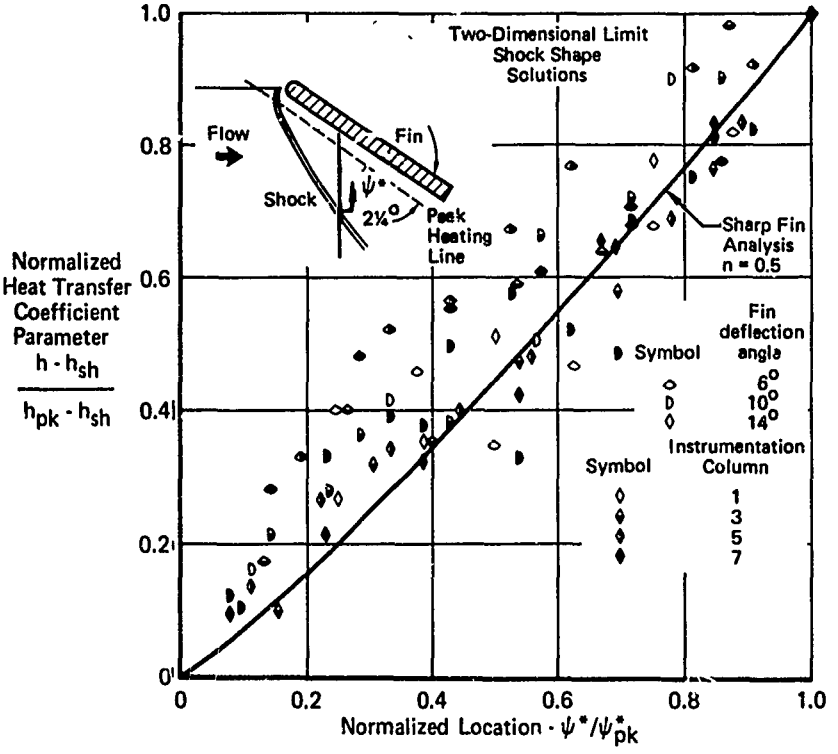

a. No Sweep

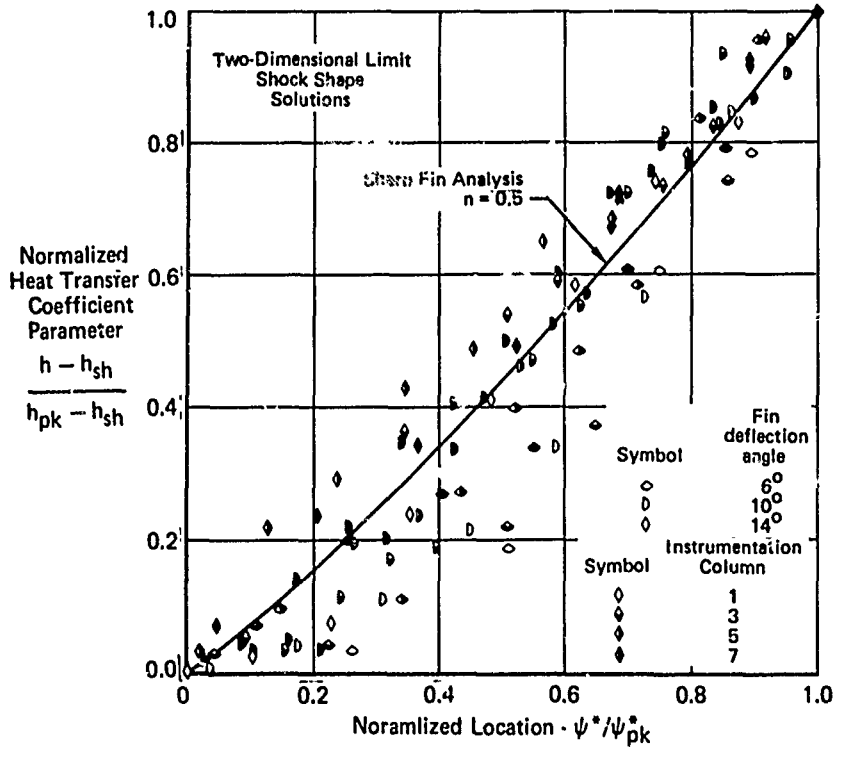

b. 45° Sweep

FIGURE 56 HEATING DISTRIBUTION CORRELATION COMPARISON - BLUNT FINS

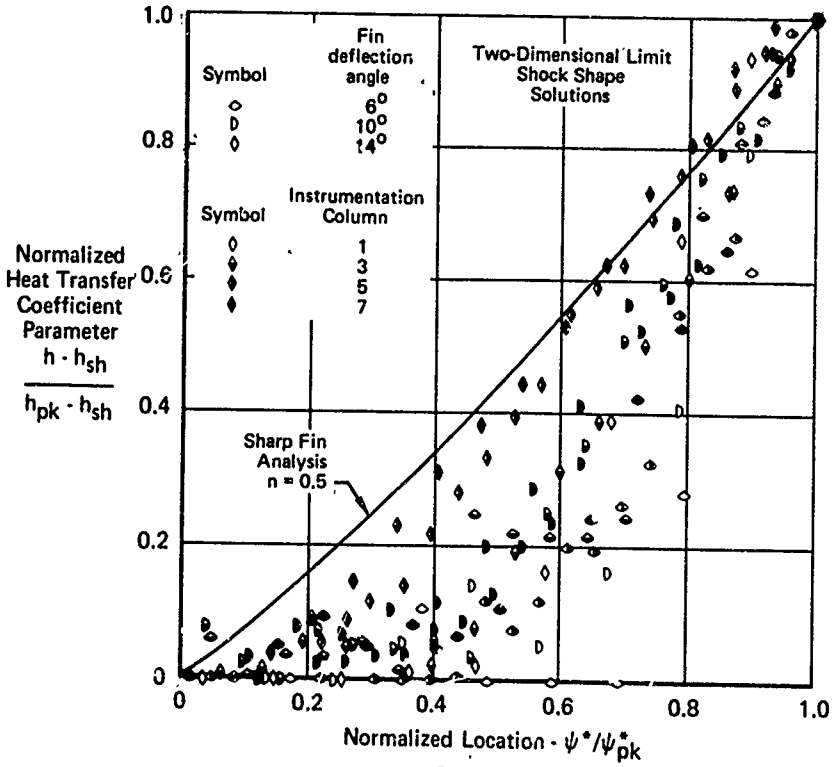

c. 60° Sweep

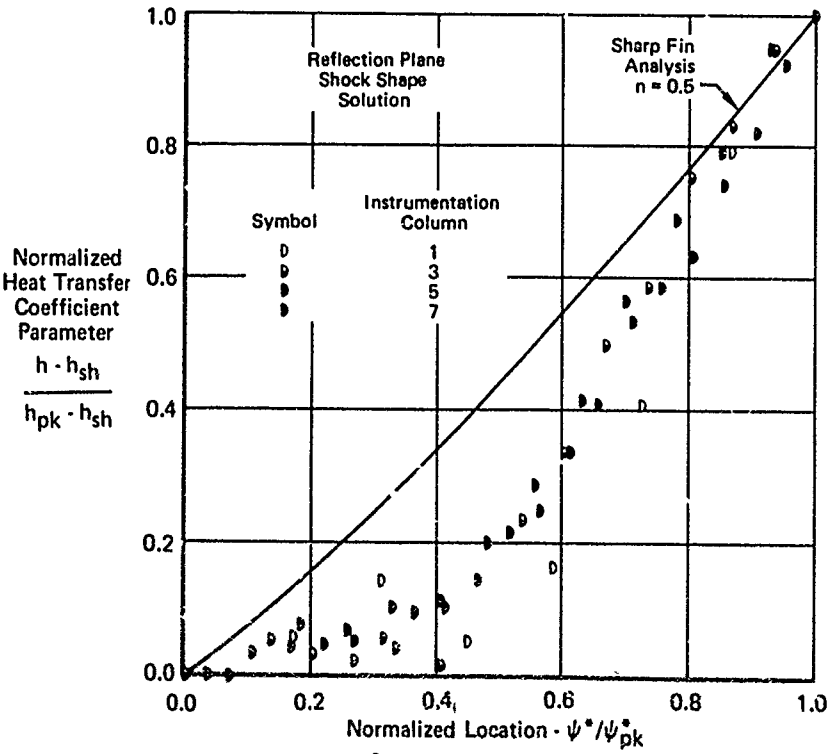

d. 60° Sweep, $\alpha = 10°$

FIGURE 56 HEATING DISTRIBUTION CORRELATION COMPARISON - BLUNT FINS (Concluded)

4. CONCLUDING REMARKS

Extensive flow field and heating data were measured in a three-dimensional shock wave turbulent boundary layer interaction region on a sidewall of a wind tunnel at Mach number 3.71. The spatial resolution provided by the 6 inches thick turbulent boundary layer on the sidewall provided excellent measurement detail.

Correlations and analyses were conducted based on sharp fin geometry and data. The concluding remarks regarding data correlation, analysis, and validation are divided into two groups, depending on fin geometry.

The data obtained with a sharp leading edge, non-swept fin, indicate that, although the interaction region is very complex, a simplified analytical approach and correlations can provide adequate design information.

1) Peak heating magnitudes normalized by a function of the inviscid pressure ratio across the shock become independent of fin angle above a fin deflection angle corresponding to McCabe's incipient separation criterion. The variation of normalized peak heating with downstream distance is hypothesized to depend upon the growth and entrainment rates of an imbedded vortex. The maximum peak heating was not measured within the instrumented region. The maximum heating occurs some distance downstream and the exact location appears to be dependent on boundary layer thickness.
2) A correlation for peak heating location was obtained which compares favorably with the test data at Mach 3.71 and with Mach 6 and 8 data. The correlations indicate that the peak heating line lies much closer to the fin than indicated by previous correlations.
3) Surface heating under the impinging shock wave, which is characteristic of separated turbulent heating, exhibits a distinct change in character at approximately the fin deflection angle which corresponds to McCabe's incipient separation angle. For fin deflection angles less than the incipient separation angle the shock heating remains constant at approximately the undisturbed value. For fin deflection angles greater than McCabe's incipient separation angle the shock heating increases with fin deflection angle. In all cases the heating is independent of downstream distance.
4) Heat transfer distributions between the shock wave and the peak heating line were shown to agree with a new analytical technique based on the presence of an imbedded vortex in the interaction

region. In proper normalized form the distributions are shown to be essentially independent of downstream location provided this distance is greater than 0.8δ from the fin leading edge, where the flow becomes locally similar, and independent of fin deflection angle provided that the fin deflection angle is greater than the incipient separation angle.

5) Oil flow data bound the incipient separation angle calculated using McCabe's criteria. A comparison with other available data is a partial validation of McCabe's criteria for incipient separation.

6) All surface and flow field data indicate that when the interaction causes separation the upstream influence is large. It is hypothesized that this influence will scale with boundary layer thickness.

Data were also obtained with blunt and blunt swept fin configurations. These data were compared to the analysis techniques which were developed and validated with sharp fin data. The results are summarized below:

7) Acceptable heating correlations were obtained for the non-swept blunt fin data. Blunt fin peak heating appeared to asymptotically approach sharp fin values sufficiently far downstream. Heating at the shock appeared to correspond to separated turbulent heating regardless of fin deflection angle. The sharp fin heating distribution analysis agreed rather well with blunt fin data considering the decidedly different flow field.

8) Correlations for blunt swept fin heating data were not acceptable in general, and were poorer for the more highly swept fin. Peak heating was lower than the corresponding sharp fin data due to the much weaker interaction aft of the stagnation region. Heating distributions did not compare with analysis. This discrepancy was related to the possibility of separation occurring downstream of the projected shock impingement point on the surface, and also to the breakdown of the local similarity assumption used in the analysis. The measured data indicates that peak heating magnitude is reduced by sweeping the fin leading edge.

5. REFERENCES

1. Korkegi, R. H., "Survey of Viscous Interactions Associated with High Mach Number Flight," AIAA Journal, July 1972, pp. 915-922.

2. Reference deleted

3. Neumann, R. D. and Burke, G. L., "The Influence of Shock Wave-Boundary Layer Effects on the Design of Hypersonic Aircraft," AFFDL-TR-68-152, March 1969.

4. Burbank, P. B. and Leon, H. B., "Distribution of Heat Transfer on a 10° Cone at Angles of Attack from 0° to 15° for Mach Numbers of 2.49 to 4.65 and a Solution to the Heat Transfer Equation That Permits Complete Machine Calculations," NASA Memo 6-4-59L, 1959.

5. Personal Communications with R. L. Stallings, NASA Langley from August 1972 to March 1974.

6. Stanbrook, A., "An Experimental Study of the Glancing Interaction Between a Shock Wave and a Turbulent Boundary Layer," Aeronautical Research Council C.P. No. 555, July 1960.

7. Maskell, E. C., "Flow Separation in Three Dimensions," Royal Aircraft Establishment Report No. AERO 2565, November 1965.

8. Van Driest, E. R., "The Problem of Aerodynamic Heating," Aero Eng. Rev., Vol. 15, No. 10, October 1956, pp. 26-41.

9. Holden, M. S., "Shock Wave-Turbulent Boundary Layer Interaction in Hypersonic Flow," AIAA Paper 72-74, January 1972, Also ARL Report 73-0137, October 1973.

10. Markarian, C. F., "Heat Transfer in Shock Wave Boundary Layer Interaction Regions," Naval Weapons Center Report NWC-TP-4485, November 1968.

11. Spalding, D. B. and Chi, W. W., "The Drag of a Compressible Turbulent Boundary Layer on a Smooth Plate With and Without Heat Transfer," Journal of Fluid Mechanics, January 1964.

12. McCabe, A., "The Three-Dimensional Interaction of a Shock Wave with a Turbulent Boundary Layer," Aeronautical Quarterly, August 1966, pp. 231-252.

13. Personal Communication with R. D. Neumann, AFFDL, September 1973.

14. Lowrie, B. W., "Cross Flows Produced by the Interaction of a Swept Shock Wave with a Turbulent Boundary Layer," Ph.D. Thesis, Univ. of Cambridge, December 1965.

15. Roshko, A., and Thomke, G. J., "Supersonic, Turbulent Boundary Layer Interaction With a Compression Corner at Very High Reynolds Numbers," Proceedings of the Symposium on Viscius Interaction Phenomena in Supersonic and Hypersonic Flow, Hypersonic Research Laboratory, Aerospace Research Laboratory, 7-8 May 1969.

16. Kuehn, D. M., "Experimental Investigation of the Pressure Rise Required for the Incipient Separation of Turbulent Boundary Layers in Two-Dimensional Supersonic Flow," NASA Memo 1-21-59A, 1959.

17. Maslen, S. H., "Inviscid Hypersonic Flow Past Smooth Symmetric Bodies," AIAA Journal, June 1964, pp. 1055-1061.

18. Barnwell, R. W. and Davis, R. M., "A Computer Program for Calculating Inviscid, Adiabatic Flow About Blunt Bodies Traveling at Supersonic and Hypersonic Speeds at Angle of Attack," NASA TMX 2334, September 1971.

NOMENCLATURE

Symbol	Meaning
C	pressure parameter = $\frac{P_{pk} - P_{sh}}{P_{sh}}$
C_p	specific heat at constant pressure - Btu/°R lb_m
h	heat transfer coefficient - Btu/Ft^2sec°R
k	thermal conductivity - Btu Ft/sec Ft^2 °R
M	Mach number
n	exponent in velocity gradient expression, see Equation (11)
P	pressure - psia
P_T	total pressure - psia
P'_T	pitot pressure - psia
q	heat transfer rate per unit area - Btu/Ft^2 Sec
Pr	Prandtl number
R	gas constant - Ft lb_F/lb_m °R
Re	Reynolds number
R_{LE}	blunt fin leading edge radius - inches
s	distance along inviscid streamline downstream of shock (inches)
T	temperature - degrees Rankine
t	time
U	velocity in the x direction - Ft/Sec.
V	velocity in the y direction - Ft/Sec.
W	weight per unit area - lb/in^2
x	distance in freestream direction downstream of fin tip - inches
y	distance normal to x-z plane from fin tip - inches
y'	distance in y direction from top of instrumentation column - inches
z	distance from test plate surfaces - inches
α	fin deflection angle measured relative to freestream direction - degrees
β	velocity gradient (cross flow plane)
γ	specific heat ratio
Δ	distance in x-direction from the intersection of peak heating line with x-axis to the fin tip - inches
Δ_s	shock stand of distance at stagnation line - inches
δ	freestream boundary layer thickness at fin tip - inches
Θ	local shock angle measured relative to freestream direction - degrees
λ	peak heating angle measured relative to freestream direction - degrees
μ	viscosity

NOMENCLATURE (CONT.)

Symbol	Meaning
ρ	density - lb_m/Ft^3
ϕ	surface streamline angle - degrees
ψ	distance defined in Figure 31 - inches
$\bar{\psi}$	distance defined in Figure 30 - inches
ψ^*	distance normal to freestream direction measured from the shock to the peak heating line - inches
$\mathcal{R}$	constant defined in Equation (16)
Subscript	
aw	adiabatic wall
bp	measured bare plate value
e	boundary layer edge condition
eq	value determined at thermodynamic equilibrium
mas	maximum
pk	local relative maximum or peak
sh	value on surface beneath inviscid shock location
w	property at wall (test plate surface)
1	value downstream of inviscid shock
∞	freestream value

*U.S.Government Printing Office: 1974 — 657-016/275